UNIVERSIDAD NACIONAL AUTONOMA DE MEXICO

Daniel Tafoya Martínez

Kinematics and Chemistry of Planetary Nebulae with Water Maser Emission

Thesis
2009

Kinematics and Chemistry of Planetary Nebulae with Water Maser Emission

Daniel Tafoya Martínez
CRyA, UNAM, México

Thesis advisor: Yolanda Gómez Castellanos
CRyA, UNAM, México

Thesis co-advisor: Nimesh A. Patel
CfA, Harvard, USA

A thesis submitted in partial fulfillment

of the requirements for the degree of

Doctor en Ciencias (Astronomía)

VNIVERSIDAD NACIONAL
AVTÓNOMA DE
MEXICO

Morelia Michoacán México, April, 2009

Cinématica y Química de Nebulosas Planetarias con Emisión Máser de Agua

Daniel Tafoya Martínez
CRyA, UNAM, México

Director de tesis: Yolanda Gómez Castellanos
CRyA, UNAM, México

Co-director de tesis: Nimesh A. Patel
CfA, Harvard, USA

Tesis presentada como requisito parcial

para obtener el grado de:

Doctor en Ciencias (Astronomía)

VNIVERSIDAD NACIONAL
AVTÓNOMA DE
MEXICO

Morelia Michoacán México, Abril, 2009

Agradecimientos

Realizar y terminar esta tesis fue posible gracias a la ayuda, comprensión, colaboración y apoyo moral de muchas personas. Durante mi trabajo de investigación, aprendí innumerables cosas de mis asesores, profesores, compañeros, amigos y familiares. Podría crear una larga lista de las personas con las cuales me encuentro enormemente agradecido, sin embargo, no me gustaría dejar a nadie fuera de dicha lista. Por esta razón, sólo menconaré que agradezco a la Dra. Yolanda Gómez y al Dr. Nimesh Patel por toda su paciencia, sus consejos, comentarios y enseñanzas; pero sobre todo les agradezco por haberme brindado su amistad. Me gustaría hacer un reconocimiento especial a mis padres, José Tafoya y Susana Martínez, quienes me han venido apoyando en todos los sentidos desde que se me ocurrió la idea de estudiar astronomía; ellos sembraron la semilla y se han esforzado para que este sueño se vuelva realidad. También agradezco a mis hermanos, Lupita, Sara y Pepe, quienes han sido mis almas gemelas y mejores amigos en este mundo; siempre que necesité escuchar una voz que me hiciera sentir lleno de entusiasmo, ellos me la proporcionaron. De forma especial, quiero agradecer a la mujer que estuvo conmigo todo este tiempo y que, para mi, significó una inspiración constante para alcanzar mis metas y seguir adelante; sin miedo a exagerar, me gustaría decir que la mitad del mérito que me corresponde por este trabajo es de ella: Andrea.

Finalmente, pero no de forma menos importante, quiero agradecer a la Universidad Nacional Autónoma de México, al Centro de Radio Astronomía y Astrofísica, y al Harvard-Smithsonian Center for Astrophysics por acogerme y brindarme el apoyo económico necesario para realizar esta actividad que tanto me gusta y apasiona. Agradezco a todo el personal técnico y administrativo por todo su esfuerzo para hacer que mi estancia fuera lo más placentera posible.

Dedicada a mi Familia
(J-S-L-S-P-A)

Contents

Overview

The current idea that the planetary nebulae are descendants of low and intermediate-mass red giants stars is accepted and widely supported by the observational evidence. However, there are still gaps in the qualitative, as well as quantitative description of the evolutive models. Careful observations and measurements of the stars undergoing the transition between those phases are necessary to complete the scheme that describes their final phases.

According to the basic scenario, proposed to explain the last stages of low and intermediate-mass stars, during the red giant phase, stars undergo an isotropic strong stellar wind, which forms a dense circumstellar envelope that expands slowly. In the oxygen-rich envelopes, the density and temperature conditions favor the population inversion of SiO, H_2O and OH molecules, leading to strong maser emission. Radio observations have confirmed the presence of this type of maser in several red giant stars. At the end of the red giant phase, the mass-loss rate of the stellar wind decreases significatively, consequently, the circumstellar envelope density decreases as well, provoking that the masers disappear gradually. Due to their location in the envelope, SiO masers should disappear in a time-scale of tens of years, H_2O masers would disappear within hundreds of years, and finally OH masers, which would last for thousands of years. The models establish that the planetary nebula phase begins around one thousand years after the red giant phase ends, therefore, SiO and H_2O maser emission was not expected to be found in planetary nebulae.

However, the association of H_2O maser emission with the planetary nebula K 3-35 was confirmed in 2001. After this detection, a survey for water maser emission in other planetary nebulae was initiated; as a result, two more planetary nebulae with H_2O maser emission have been found: IRAS 17347−3139 and IRAS 18061−2505. These discoveries have provoked that the scenario that explains the formation of masers in evolved stars needs

to be revised.

On the other hand, these three planetary nebulae show a clear bipolar symmetry with a very narrow equatorial waist; currently, the physical processes responsible for the formation of these kind of morphologies are not well known. The standard interacting winds model, proposed to explain the formation of planetary nebulae, is incompatible with the observations. The presence of binary systems, magnetic fields, collimated winds, equatorial disks, etc. has been invoked to model the formation of bipolar morphologies with symmetries as those observed in these planetary nebulae. Nevertheless, the observational evidence and the measurements of the different physical parameters, needed to constrain the theoretical models, are scarce in these objects.

In this thesis work, we have studied two of the three planetary nebulae harboring water maser emission: K 3-35 and IRAS 17347−3139. Our goals were focused on trying to characterize the physical conditions of the gas in these nebulae to be able to understand the persistence of H_2O masers as well as to determine what are the physical mechanisms that could be playing an important role in the formation of bipolar morphologies with narrow waists and point symmetry. Due to the intrinsic nature of the phenomena that we aimed to investigate, and due to the fact that these sources are extremely obscured in the visible band, our observations have been carried out mainly at radio wavelengths; moreover, since the angular sizes of the sources are very small, we have made use of techniques of synthesis imaging with radio interferometers.

In chapter 1, a general introduction to the current evolutive scenario for low and intermediate-mass stars is presented. We remark the different models that have been proposed to explain the evolution of the last stages in the lives of these kinds of stars; including the formation of planetary nebulae with different sorts of morphologies. At the end of this chapter, a brief review of the molecular emission in late-type stars is presented, emphasizing the maser emission that typically arises in these astronomical sources. In chapter 2, we go through some of the mechanisms responsible for the emission of radio waves in cosmic sources. The continuum emission processes are presented in detail, explaining how one can derive the physical parameters from the observations. The basic concepts related with line emission are discussed, as well as the physical parameters that can be obtained from the observations. In this chapter, the phenomenon of maser emission is explained; we briefly discuss the pumping mechanisms that lead to maser emission, as well

as the methods proposed to determine the strength of astronomical magnetic fields through polarimetric observations of masers. In chapter 3, we present a paper in which we report the detection of HCO^+ emission towards the planetary nebula K 3-35. In this paper we determine the temperature and mass of the molecular gas, as well as an upper limit to the size of its extent; we also suggest the presence of dense globules of neutral gas within which the water molecules could be excited to produce maser emission. In chapter 4 of this thesis, it is included a paper in which we report the detection of a Zeeman pair from the OH maser emission arising in the equatorial region of the planetary nebula K 3-35. From this detection, we deduced the presence of a magnetic field with a strength of $\sim$ 1 mG. In this chapter we also show the spatial distribution and kinematics of the OH masers that are tracing different regions of the nebula. From the results, we found that the masers are being tracing an equatorial torus, as well as a more extended axisymmetric outflow. We conclude that the magnetic field in K 3-35 could be playing an important role in the collimation of its bipolar lobes, however, more measurements are necessary to clearly understand how magnetic fields are working on the shaping of the great-scale morphology of the nebula. In chapter 5, we present a paper in which we report the results of our radio continuum, as well as OH masers, observations towards the planetary nebula IRAS 17347−3139. We show the first images in which we could resolved the emission form the ionized gas in this nebula at 3 wavelengths (3.6, 1.3 and 0.7 cm). In order to estimate the electronic density, we derived the spectral index of the emission. According to the results, the ionized region of IRAS 17347−3139 consists basically of two components: a dense equatorial torus-like structure from which the water maser emission is originating; the second component is extended in the direction of the bipolar lobes and has a lower density. This extended component shows a subtle point-symmetry suggesting the presence of a collimated and precessing wind that would be excavating the bipolar lobes. In this paper we also report the first detection of OH maser emission toward this planetary nebula.

Resumen General

Actualmente, la idea de que las nebulosas planetarias son descendientes de las estrellas gigantes rojas de baja y mediana masa se acepta de forma consensual y es ampliamente apoyada por la evidencia observacional. Sin embargo, aún existen lagunas en la descripción, tanto cualitativa como cuantitativa, de los modelos evolutivos; observaciones y mediciones cuidadosas de estrellas que se encuentran en la transición de ambas fases son necesarias para poder completar el esquema que describe sus las últimas etapas.

De acuerdo al escenario básico, propuesto para explicar las últimas etapas de las estrellas de baja y mediana masa, durante la etapa de gigante roja, las estrellas poseen un viento estelar isotrópico e intenso, el cual forma una envolvente circunestelar densa que se expande lentamente. En las envolventes ricas en oxígeno, las condiciones de densidad y temperatura favorecen la inversión de poblaciones de las moléculas de SiO, H_2O y OH, propiciando que se produzca emisión máser intensa. Observaciones de radio han confirmado la presencia de este tipo de másres en varias estrellas gigantes rojas. Al final de la etapa de gigante roja, la tasa de pérdida de masa del viento estelar disminuye significativamente, como consecuencia, la densidad de la envolvente circunestelar también disminuye, esto provoca que los máseres desaparezcan gradualmente. Debido a su localización en la envolvente, los máseres de SiO deben desaparecer en una escala de tiempo de decenas de años, los máseres de H_2O desaparecerían en una escala de tiempo de cientos de años, y finalmente los de OH en escalas de tiempo de miles de años. Los modelos establecen que la etapa de nebulosa planetaria comienza unos mil años después de que termina la fase de gigante roja, por lo tanto, no se esperaba encontrar máseres de SiO o H_2O en nebulosas planetarias.

Sin embargo, en 2001 se confirmó la asociación de emisión máser de H_2O con la nebulosa planetaria K 3-35. A partir de esta detección, se comenzó una búsqueda de emisión máser de agua en otras nebulosas planetarias; como re-

sultado, se han encontrado otras dos nebulosas planetarias con emisión máser de H_2O: IRAS 17347−3139 e IRAS 18061−2505. Estos descubrimientos han propiciado que se tenga que revisar el escenario que explica la formación de máseres en estrellas evolucionadas.

Por otro lado, estas tres nebulosas planetarias muestran una clara simetría bipolar con la cintura muy angosta; hoy en día, los procesos físicos responsables de la formación de este tipo de morfologías no se conocen con claridad. El modelo estándar de vientos interactuantes, propuesto para explicar la formación de nebulosas planetarias, es incompatible con las observaciones. La presencia de sistemas binarios, campos magnéticos, vientos colimados, discos ecuatoriales, etc. ha sido invocada para modelar la formación de morfologías bipolares con simetrías como las que se observan en estas nebulosas. No obstante, la evidencia observacional y las mediciones de los diferentes parámetros físicos, necesarios para restringir los modelos teóricos, en estas nebulosas planetarias es escasa.

En este trabajo de tesis, hemos estudiado dos de las tres nebulosas planetarias que presentan máseres de H_2O: K 3-35 e IRAS 17347−3139. Nuestros objetivos se enfocan en tratar de caracterizar las condiciones físicas del gas en estas nebulosas para poder entender la persistencia de máseres de H_2O, así como determinar los mecanismos físicos que pueden estar jugando un papel importante en la formación de morfologías bipolares con cinturas estrechas y con simetría de punto. Debido a la naturaleza intrínseca de los fenómenos que deseamos investigar, además de que las fuentes se encuentran muy oscurecidas en la banda visible, nuestras observaciones se han llevado a cabo principalmente en longitudes de onda de radio; además, ya que los tamaños angulares de las fuentes son muy pequeños, hemos usando técnicas de sintesís de imágenes usando radio interferómetros.

En el capítulo 1, se presenta el panorama general del escenario evolutivo actual que se tiene para estrellas de baja masa y masa intermedia. Se destacan los diferentes modelos que se han propuesto para explicar el desarrollo de las últimas etapas en la vida de esta clase de estrellas y la formación de nebulosas planetarias con diferentes tipos morfologías. Una breve revisión sobre la emisión molecular se incluye al final del capítulo, enfatizando la emisión máser que típicamente se origina en estos objetos astrómicos. En el capítulo 2, se exponen algunos de los mecanismos físicos responsables de la emisión de radio en las fuentes cósmicas. Se detallan los procesos de emisión de continuo y como se pueden derivar ciertos parámetros físicos a partir de las observaciones. También se presentan los conceptos básicos relacionados

con la emisión de línea y la obtención de parámetros físicos a partir ellos. En este capítulo se explica el fenómeno máser; se discuten brevemente los mecanismos de bombeo que conducen a la emisión máser, así como los procedimientos que se han propuesto para determinar el campo magnético a partir de observaciones polarimétricas de máseres. En el capítulo 3, se presenta un artículo en el que se reporta la detección de emisión de HCO^+ en la nebulosa planetaria K 3-35. En este artículo se determina la temperatura y masa del gas molecular, así como un límite superior para su tamaño; también se propone la presencia de grumos densos de gas neutro dentro de los cuales las moléculas de agua pueden estar siendo excitadas para producir emisión máser. En el capítulo 4 de esta tesis, se incluye un artículo en el que se reporta la detección de un par Zeeman de la emisión máser de OH proveniente de la región ecuatorial de la nebulosa planetaria K 3-35. A partir de esta detección, se dedujo la presencia de un campo magnético con una intensidad de ~ 1 mG. En este capítulo, también se muestra la distribución espacial y cinématica de los máseres de OH que trazan diferentes regiones en la nebulosa. De los resultados, se pudo encontrar que los máseres se originan tanto en una especie de toroide en la parte ecuatorial, como en un flujo axial más extendido. Se concluye que el campo magnético en K 3-35 puede estar jugando un papel importante en la colimación de los lóbulos de esta nebulosa, sin embargo, se necesitan mas detecciones como esta para poder entender claramente el papel que los campos magnéticos juegan en la formación a gran escala de morfologías bipolares. En el capítulo 5, se presentan un artículo en el que se dan a conocer los resultados de observaciones, tanto de radio continuo como de máseres de OH, de la nebulosa planetaria IRAS 17347−3139. Se muestran las primeras imágenes resueltas del gas ionizado en esta nebulosa a 3 longitudes de onda (3.6, 1.3 y 0.7 cm), y se deriva el índice espectral de la emisión para poder obtener la densidad electrónica. De acuerdo a los resultados, la región ionizada de IRAS 17347−3139 consta básicamente de dos componentes: una ecuatorial y de mayor densidad, donde se origina la emisión máser, y otra de menor densidad, extendida en el eje axial, correspondiendo a la dirección de los lóbulos bipolares observados en imágenes infrarrojas. La emisión muestra una ligera simetría de punto sugiriendo la presencia de un viento colimado y precesando que está excavando los lóbulos bipolares. En este artículo también se reporta la primera detección de emisión máser de OH en esta nebulosa planetaria.

Síntesis

La primera nebulosa planetaria (NP), de la cual se tiene registro, fue observada por Charles Messier en 1764 durante su famosa búsqueda de objetos con apariencia similar a la de los cometas; esta nebulosa entró en su catálogo como el objeto número 27. En aquellos días, no se conocía la naturaleza intrínseca de la mayoría de los objetos nebulosos del catálogo de Messier. Sin embargo, se pensaba que se podría tratar de sistemas estelares similares a Las Pléyades o El Pesebre que, debido a la enorme distancia a la que se encontraban, no se podían resolver en estrellas individuales. El músico y astrónomo inglés, William Herschel, obsevó miles de nebulosas y las clasificó de acuerdo a las propiedades visuales que mostraban a través de su telescopio (Herschel 1786, 1789). Herschel usó por primera vez el nombre de Nebulosa Planetaria para referirse a un tipo de nebulosas que presentaban características muy similares a las de los planetas: brillo superficial uniforme y vívido, con un diámetro pequeño y bien definido (Herschel 1785). Conforme la resolución angular ofrecida por los telescopios fue aumentando, se pudo diferenciar a las nebulosas gaseosas de las galaxias y cúmulos estelares (constituidos básicamente de estrellas). Así mismo, las nebulosas planetarias (NPs) fueron distinguidas de las otras nebulosas gaseosas debido a que presentaban estructuras más definidas y frecuentemente se les encontraba una estrella central asociada.

La concepción de que las NPs representan una de las últimas fases de la evolución estelar se desarrolló con trabajos teóricos como el de Shklovsky (1956), quien propuso que las NPs son progenitoras de las estrellas enanas blancas y descendientes de las estrellas gigantes rojas. Abell & Goldreich (1966) revisaron los posibles escenarios bajo los cuales se podrían formar las NPs; ellos llegaron a la conclusión de que las estrellas con una masa del orden de 1.2 $M_{\odot}$* deben pasar por la fase de NP, además, que los directos

*1 $M_{\odot}$=1.99×10^{33} gr.

progenitores de las NPs son estrellas gigantes rojas. Sin embargo, los mecanismos físicos responsables de la expulsión del gas que forma a las NPs no se conocían con claridad. El primer esquema del escenario de formación de NPs cuantitativamente compatible con las observaciones fue establecido por Kwok et al. (1978) con su modelo de vientos estelares interactuantes. Este modelo se basa en las observaciones que revelan que las estrellas de baja masa y masa intermedia ($M < 8M_{\odot}$), en la fase evolutiva llamada rama asintótica de las gigantes (RAG o AGB por sus siglas en idioma inglés), expulsan de manera continua (durante unos 10^4 años) una fracción importante de su envolvente a través de un viento masivo, con tasas de pérdida de masa de hasta $\dot{M} \sim 10^{-5} M_{\odot}$ año^{-1}, expandiéndose a una velocidad de unos 10 km s^{-1} (Viento Lento). El modelo establece que una vez que la tasa de pérdida de masa del Viento Lento disminuye y el núcleo queda desprendido de la envolvente en expansión, una nueva fase de pérdida de masa comienza, creándose un viento más tenue ($\dot{M} \sim 10^{-7} M_{\odot}$ año^{-1}) y expandiéndose a una velocidad mucho mayor, a unos 10^3 km s^{-1} (Viento Rápido). Este último viento, alcanza al material expulsado durante el Viento Lento y se produce un choque. La temperatura del gas chocado aumenta considerablemente; una burbuja de gas caliente en expansión, empuja y comprime al gas de las partes externas, formando una cáscara (similar al efecto de una pala de nieve). Cuando el núcleo alcanza la temperatura suficiente para producir copiosas cantidades de fotones ionizantes, esta cáscara en expansión es ionizada y puede ser detectada (e.g. en emisión óptica) como una nebulosa planetaria.

Hoy en día, el modelo evolutivo que establece que las NPs son descendientes de las estrellas gigantes rojas se acepta de forma consensual. Sin embargo, debido a que la fase de transición es relativamente corta ($\sim$ 1000 años; Kwok 1993), las observaciones de objetos en dicha transición son escasas y difíciles de llevar a cabo; como resultado, existen aún varios eslabones perdidos en el estudio de la evolución de estrellas de baja masa y masa intermedia. Por ejemplo, se ha observado que las partes externas de las envolventes circunestelares de la mayoría de las estrellas gigantes rojas muestran una simetría aproximadamente esférica (e.g. OH127.8, Booth et al. 1981). Sin embargo, sorprendentemente, las NPs muestran una amplia gama de simetrías no esféricas: bipolares, multipolares, de punto, de espejo, etc. De hecho, el alejamiento de la simetría esférica se ha observado en las envolventes circunestelares de algunas estrellas AGB (e.g. TW Hydra; Hirano et al. 2003) y en la mayoría

de las proto-nebulosas planetarias[**] (e.g. Sahai et al. 2007). La formación y desarrollo de las diferentes morfologías en las nebulosas y proto-nebulosas planetarias, así como su evolución química, se encuentran entre los estudios más activos y excitantes en el campo de la evolución estelar en la astrofísica moderna.

Figura 1: La nebulosas y proto-nebulosas planetarias muestran una amplia gama de morfologías como se puede apreciar en este mosaico de nebulosas fotografiadas con el Telescopio Espacial Hubble. Cuadro superior izquierdo: NP NGC 6543 (Ojo de gato). Cuadro superior derecho: NP MyCn 18 (Reloj de arena). Cuadro inferior izquierdo: Proto-nebulosa planetaria Hen 401. Cuadro inferior derecho: NP Mz 3 (Hormiga).

Actualmente, existe una enorme cantidad de observaciones en todas las longitudes de onda que, junto con los modelos teóricos, han ayudado a los astrónomos a entender las últimas etapas de la evolución de las estrellas de baja masa y masa intermedia. En particular, las observaciones en radio frecuencias poseen la ventaja de que la emisión a estas longitudes de onda no

[**]Las proto-nebulosas planetarias son los progenitores inmediatos de las NPs; se caracterizan porque aún no han sido ionizadas por la estrella central y su brillo se debe básicamente a radiación dispersada.

es absorbida por el polvo que se forma en la envolvente circunestelar de estos objetos. Además, se ha observado que precisamente en las oscuras y frías envolventes circunestelares de estas estrellas se propician las condiciones para la formación de diversas moléculas, las cuales producen líneas de emisión en longitudes de onda centimétricas, milimétricas y submilimétricas (e.g. Pardo et al. 2007). Por otro lado, también se sabe que la componente ionizada de las NPs emiten la mayor parte de su energía en forma de radio continuo. Debido a ésto, las observaciones en radio frecuencias constituyen una herramientas invaluable para el estudio de estos objetos. Por ejemplo, a partir de las observaciones moleculares, podemos estimar la distribución, cinemática y propiedades físicas de su componente neutra; la presencia y abundancia de ciertas especies moleculares, así como el grado de ionización de la envolvente nos ofrece información sobre el estado evolutivo de la NP.

Se ha observado que cuando la envolvente circunestelar de la estrella es rica en oxígeno (i.e. [O/C]>1), se puede producir fuerte emisión máser de moléculas como SiO, H_2O (agua) y OH (Reid & Moran 1981; Elitzur 1992b; Habing 1996). Debido a que las condiciones necesarias para la excitar y bombear los máseres son diferentes para cada clase molecular, los máseres de SiO aparecen cerca de la fotósfera estelar ($R \simeq 10^{14}$ cm); los máseres de agua aparecen a unos $\simeq 10^{15}$ cm del centro de la estrella, y los máseres de OH a unos $\simeq 10^{16}$ cm (Reid & Moran 1981; Elitzur 1992b; Habing 1996; Lane et al. 1987).

Generalmente, para excitar e invertir las poblaciones de estas moléculas, se requieren altas densidades, temperaturas moderadas y un campo de radiación intenso. La densa envolvente circunestelar formada por el Viento Lento ofrece tales condiciones. Sin embargo, al final de la etapa AGB, cuando la tasa de pérdida de masa del Viento Lento disminuye considerablemente, condiciones físicas necesarias para producir la emisión máser de los diferentes tipos de moléculas en la envolvente circunestelar van desapareciendo gradualmente. Si se toma en cuenta que la velocidad del Viento Lento y denso es de unos ~ 10 km s^{-1}, un simple cálculo predice la densidad en la región donde se produce la emisión máser de SiO disminuye considerablemente al cabo de unos 10 años, lo que provoca que dicha emisión desaparezca; los máseres de agua desaparecen después de 100 años, mientras que los máseres de OH pueden perdurar hasta más de 1000 años (Lewis 1989; Gómez, Moran & Rodríguez, 1990). Aún más, cuando la estrella central alcanza la temperatura suficiente para emitir fotones de alta energía, las moléculas en la envolvente circunestelar se ven expuestas a un campo de radiación ionizante que pue-

de foto-disociarlas. Como consecuencia, hasta recientemente, no se esperaba encontrar emisión máser de SiO o de agua en NPs, donde la densidad ha disminuido considerablemente y la ionización del gas ha comenzado.

Sorprendentemente, Miranda et al. (2001) confirmaron la asociación de emisión máser de agua con la fuente K 3-35, convirtiéndola en la primera nebulosa planetaria con este tipo de emisión. Los máseres de agua fueron encontrados en tres regiones: hacia el norte, hacia el centro y hacia el sur de la región ionizada de la nebulosa (ver Figura 2). La distribución de los máseres en K 3-35 es muy similar a la que presentan las llamadas nebulosas *water fountain*, que son pNPs con máseres de agua a velocidades superiores a las de los máseres de OH, y que generalmente trazan estructuras colimadas o chorros bipolares (e.g. Imai, Sahai & Morris 2007; Claussen, Sahai & Morris 2008). Sin embargo, el caso de K 3-35 es particular porque los máseres aparecen en regiones que, proyectadas, coinciden con el gas ionizado, mientras que en las nebulosas water fountain, la emisión proviene de regiones neutras.

Miranda et al. (2001) sugirieron que probablemente podría existir algún mecanismo de escudamiento que estaría protegiendo a las moléculas de agua de no ser destruidas por la radiación ionizante de la estrella central. Dayal & Bieging (1996) detectaron eisión de CO ($J = 2 \rightarrow 1$) en la dirección de K 3-35, lo cual vino a reforzar la sospecha de la presencia de gas molecular neutro donde podría estar originándose la emisión máser de agua. Para corroborar si podría existir algún mecanismo de escudamiento en la envolvente circunestelar de K 3-35, llevamos a cabo una búsqueda de moléculas hacia esta NP. Usando los radiotelescopios de 20 metros en Onsala, Suecia; de 30 metros en Sierra Nevada, España y de 45 metros en Nobeyama, Japón, buscamos emisión de las siguientes moléculas: SiO, $H^{13}CO^+$, HNC, HCN, HC_3OH, HC_5N, CS, HC_3N, ^{13}CO, CN, y NH_3. Como resultado de este proyecto, se logró confirmar la asociación de la emisión de CO ($J = 2 \rightarrow 1$), que se había reportado previamente, y también se detecto por primera vez emisión de la transición CO ($J = 1 \rightarrow 0$) y de la molécula HCO^+ ($J = 1 \rightarrow 1$) (ver Figura 3).

De las observaciones de CO pudimos obtener un límite superior del tamaño de la región donde se está originando dicha emisión: $\sim 20''$. Del cociente de la emisión CO ($J = 2 \rightarrow 1$) y CO ($J = 1 \rightarrow 0$) se estimó un valor para la temperatura cinética del gas de unos 20 K; a partir de este resultado, también pudimos obtener el valor de la masa molecular de la envolvente circunestelar en K 3-35 ($M_m \simeq 0.017 M_\odot$.)

De nuestras observaciones, estimamos que la densidad columnar prome-

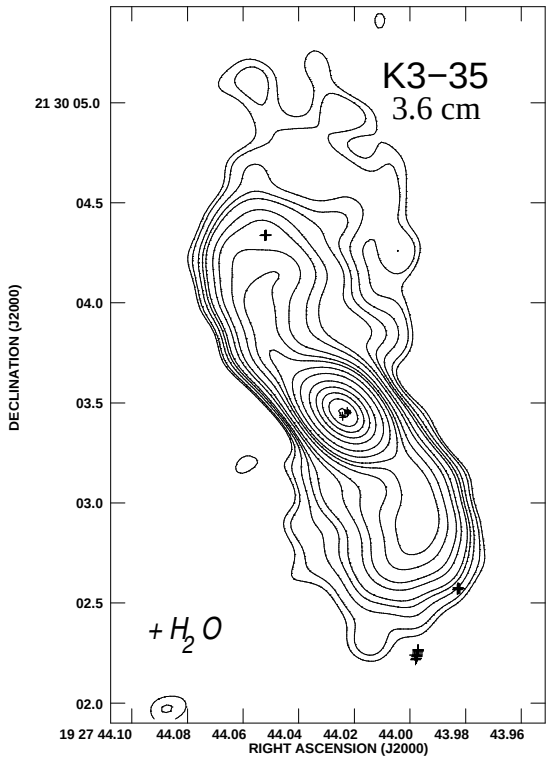

Figura 2: Posiciones de los máseres de agua en la NP K 3-35. Los contornos representan la emisión de radio continuo observada con el VLA a una longitud de onda de 3.6 cm. (Miranda et al. 2001; Gómez et al. 2003)

diada en el haz primario ($\simeq 44''$) de HCO^+ es de $N(HCO^+) \simeq 6.9 \times 10^{11}$ cm^{-2}. Se ha observado que la abundancia de HCO^+, $[HCO^+/H_2]$, es mayor en las NPs que en las proto-nebulosas planetarias, donde la estrella central aún no ha comenzado a ionizar la envolvente (Bachiller et al. 1997; Bachiller & Josselin 2003). Se ha sugerido que ésto se debe probablemente a que un entorno ionizado o foto-disociado favorece la formación de la molécula HCO^+ (Bachiller et al. 1997). Por otro lado, de acuerdo con Huggins et al. (1996), comparando el valor de la masa del gas ionizado (M_i) con la masa del gas molecular, se puede construir un diagrama que nos permite determinar el grado de evolución de las NPs. Para tratar de comparar la abundancia de HCO^+ en K 3-35, y su estado evolutivo respecto a otras NPs y objetos post-AGB, graficamos $[HCO^+/H_2]$ como función de M_i/M_m. De nuestros resultados podemos

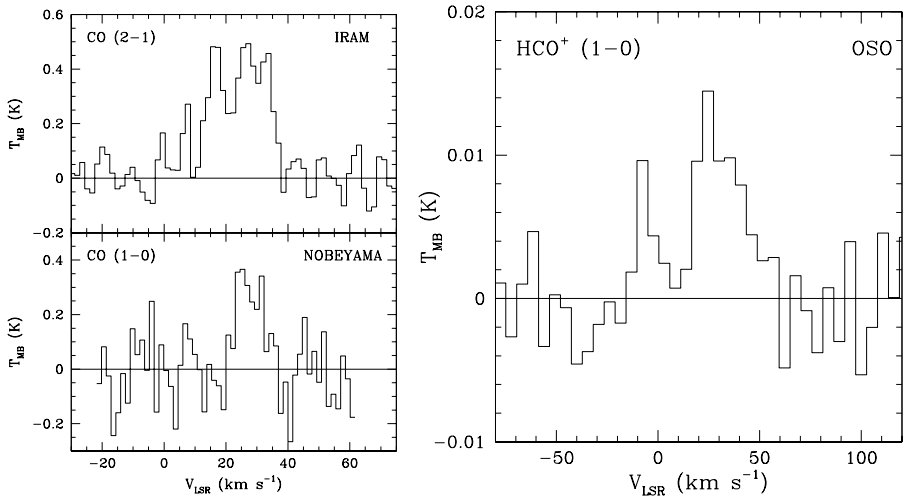

Figura 3: Izquierda, panel superior: espectro de la transición CO ($J = 2 \rightarrow 1$) de la NP K 3-35, obtenido con el radio telescopio de 30 m del IRAM, en España. Izquierda, panel inferior: espectro de la transición CO ($J = 1 \rightarrow 0$) de la NP K 3-35, obtenido con el radio telescopio de 45 m del NAOJ, en Japón. Derecha: espectro de la transición HCO^+ ($J = 1 \rightarrow 0$) de la NP K 3-35, obtenido con el radio telescopio de 20 m del OSO, en Suecia.

corroborar que K 3-35 es, en efecto, una NP muy joven; también encontramos que la abundancia de HCO^+ en este objeto es ligeramente mayor que en otras NPs.

La detección de HCO^+ en K 3-35 sugiere la presencia de regiones de alta densidad ($\sim 10^5$ cm^{-3}) en su envolvente. Se ha observado en algunas NPs la presencia de glóbulos de alta densidad embebidos en el gas ionizado (Huggins et al. 1992). Estos glóbulos son lugares donde la formación de HCO^+ se ve favorecida, por lo que sugerimos que posiblemente existan glóbulos de alta densidad embebidos en la componente ionizada de K 3-35. Dentro de estos glóbulos se podrían dar las condiciones de densidad y temperatura para escudar las moléculas de agua de los fotones ionizantes de la estrella central y además bombear la emisión máser observada. Estos resultados fueron publicados en Tafoya et al. (2007).

K 3-35 también presenta emisión máser de OH en las cuatro transiciones a $\lambda \sim 18$ cm: 1612, 1665, 1667 y 1720 MHz (Engels et al. 1985; Miranda et al. 2001). Estos máseres aparecen espacialmente localizados hacia la re-

gión central de la nebulosa $\lesssim$ 1000 AU[***] (adoptando una distancia de 5 kpc[****], Zhang 1995). Miranda et al. (2001) observaron las transiciones a 1665 y 1667 MHz en esta nebulosa; de sus observaciones, ellos encontraron niveles de polarización circular de hasta el 50 % en la transición a 1665 MHz. A estas frecuencias la presencia de polarización circular de los máseres de OH puede deberse a la existencia de campos magnéticos. Miranda et al. (2001) estimaron que la intensidad del campo magnético requerido para producir la polarización circular observada en K 3-35 es del orden de miligauss y propusieron que su presencia apoyaría los modelos magnéticos para la colimación de los flujos de gas (e.g. García-Segura & López 2000).

En 2005, hicimos nuevas observaciones interferométricas de la emisión máser en las cuatro transiciones del OH a $\lambda\sim$ 18 cm (ver la Figura 4). Estas observaciones tienen mayor sensitividad y resolución, tanto espectral como angular, que las anteriores. La emisión a 1665 MHz se escuentra distribuida mas o menos a lo largo de la dirección perpendicular al eje axial de los lóbulos, y muestra un gradiente de velocidad en esta misma dirección, por lo que se ha sugerido que podrían estar trazando una estructura ecuatorial (toroide). Por otro lado, los máseres a 1667 MHz tienen una distribución y gradiente de velocidad más bien paralela al eje axial de los lóbulos, sugiriendo en primera instancia que podrían estar trazando un flujo polar de gas. Sin embargo, la emission aparece en dos grupos espectrales que están desplazados hacia el azul respecto a la velocidad sistémica, lo que nos ha hecho proponer que ambos son parte del flujo que se aproxima hacia nosotros. La emisión maśer a 1720 MHz se encuentra concentrada en la posición correspondiente al pico de radio continuo a 1.3 cm, probablemente originándose muy cerca de la estrella central. Finalmente, los máseres a 1612 MHz parecen estar viniendo tanto del flujo axial que se aproxima a nosotros, como del posible toroide.

Como se ve en la Figura 4, encontramos polarización circular en las transiciones a 1612, 1665 y 1667 MHz (parámetro de stokes V). En particular, la emisión a 1665 MHz muestra emisión polarizada originándose en un mismo punto, lo cual sugiere que podría tratarse de un *par Zeeman*. Este resultado corrobora la proposición de Miranda et al. (2001), de que existe un toriode magnetizado en K 3-35. Nosotros hemos estimado que la intensidad del campo magnético en la dirección de nuestra línea visión es de $\sim$ 0.3 miligauss. Aunque esta medición esta hecha en una región particular de la nebulosa,

[***] 1 UA=radio promedio de la órbita de la Tierra $=1.5\times10^{13}$ cm.
[****] 1 kpc=10^3pc; 1 pc=3.08×10^{18} cm.

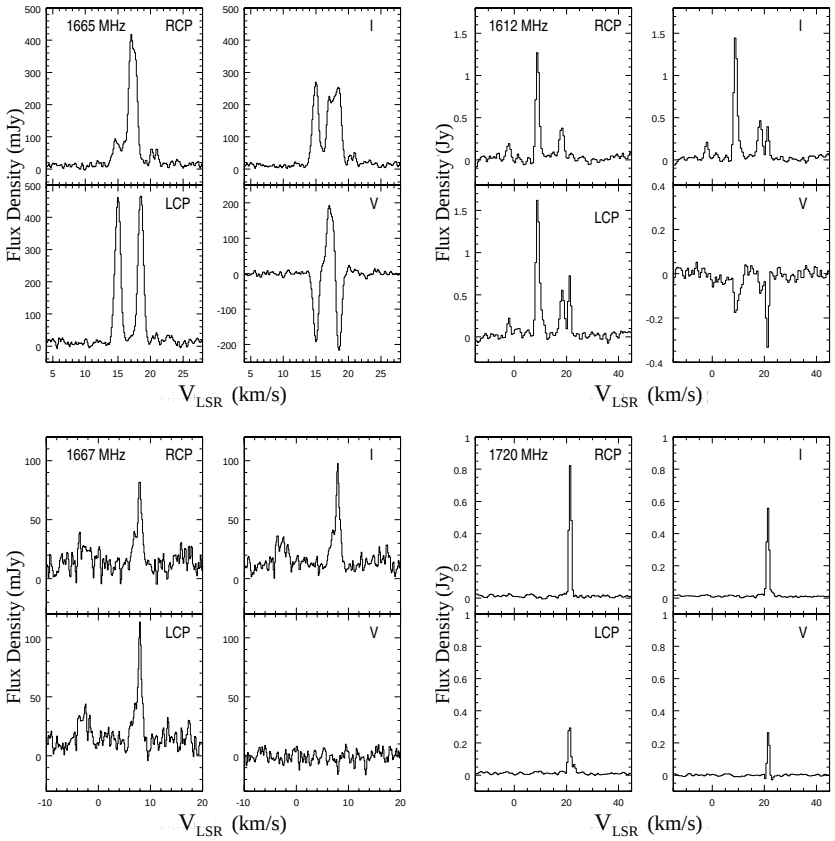

Figura 4: Espectros de polarización circular derecha e izquierda (RCP y LCP por sus siglas en idioma inglés, respectivamente), y de los parámetros de Stokes I y V de la nebulosa planetaria K 3-35, para las transiciones del OH a 1665, 1612, 1667, y 1720 MHz (Gómez, Tafoya et al. 2009). Los espectros fueron obtenidos integrando la emisión en una caja de $\sim 5''$, centrada en la posición del pico del radio continuo a $\lambda \sim 1.3$ cm. La velocidad sistémica V_{LSR} de la fuente es ~ 23 km s^{-1} (Tafoya et al. 2007).

este resultado es de gran valor ya que podría ser utilizado en los modelos de formación de chorros colimados, que invocan un campo magnético, y valorar que tan importante es el papel que desempeña este mecanismo en su colimación. Estos resultados aparecerán publicados en Gómez, Tafoya et al. (2009).

Después de que se confirmara la existencia de emisión máser de agua ori-

ginándose en la NP K 3-35, de Gregorio-Monsalvo et al. (2004) realizaron una búsqueda de máseres de agua hacia otras 26 nebulosas planetarias jóvenes. Como resultado, estos autores encontraron máseres de agua en la nebulosa planetaria IRAS 17347−3139, convirtiéndose en la segunda estrella de este tipo con emisión máser de agua. Los máseres fueron encontrados trazando una elipse, localizada hacia el centro de la nebulosa (ver Figura 5).

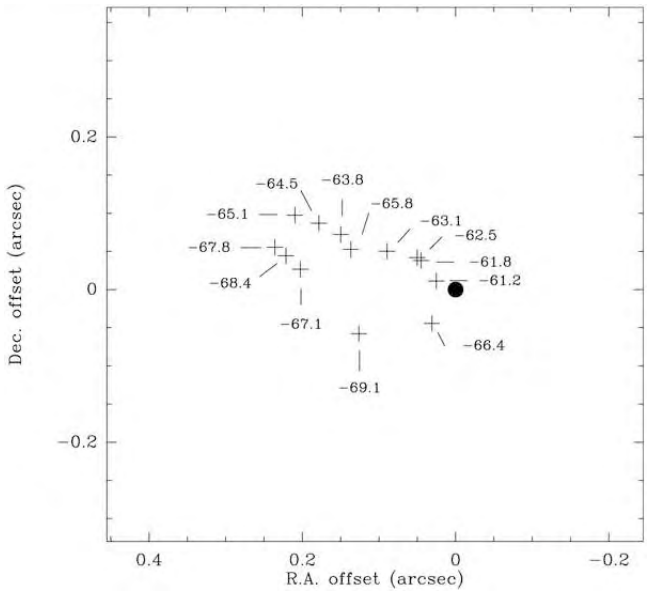

Figura 5: Distribución de los máseres de agua en la NP IRAS 17347−3139. El punto negro indica la posición del pico de radio continuo a 1.3 cm. (de Gregorio-Monsalvo et al. 2004)

De manera interesante, se encontró que el centro de la distribución de máseres está desplazado unos 0.″15 de la posición del pico del radio continuo a 1.3 cm. Una posible explicación de este desplazamiento es que se trate de un sistema binario en el que los máseres estarían asociados a uno de los miembros, y el radio continuo estaría asociado al otro. Sin embargo, la resolución angular (tamaño del haz sintetizado $> 0.''3$) de estas observaciones no fue suficiente para confirmar esta hipótesis. Para tratar de determinar si hay un sistema binario en IRAS 17347−3139, en 2005 llevamos a cabo observaciones de radio continuo a longitudes de onda de 3.6, 1.3 y 0.7 cm con el radio interferómetro *Very Large Array* en su configuración A, alcanzando una máxima resolución angular de 0.″1. Con estas observaciones pudimos resolver

espacialmente por primera vez la estructura del gas ionizado en esta NP. La emisión de radio continuo puede ser interpretada como originándose en dos regiones orientadas perpendicularmente entre sí. Una región es extendida y más tenue, alargada en la dirección de los lóbulos bipolares observados en las imágenes infrarrojas. La otra región es más compacta y brillante, y está alargada en la dirección de una banda oscura ecuatorial también vista en las imágenes infrarrojas.

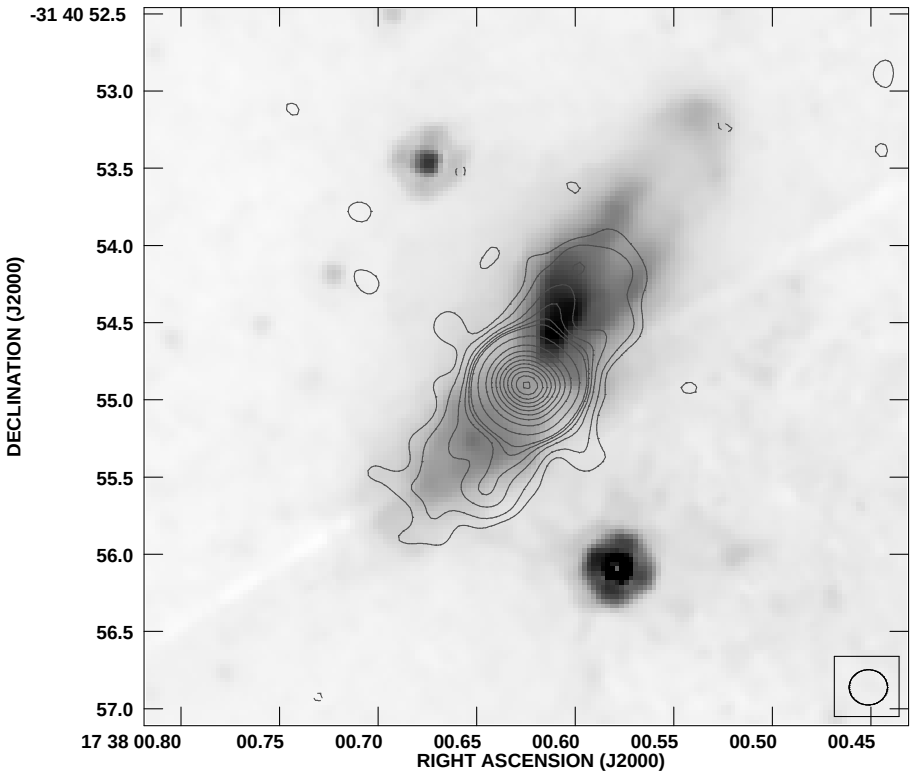

Figura 6: Contornos: imagen de IRAS 17347−3139 tomada con el VLA a λ =1.3 cm. Escala de grises: imagen infrarroja de IRAS 17347−3139 tomada con el Telescopio Espacial Hubble a λ =1.1 μm (Tafoya et al. 2008).

de Gregorio-Monsalvo et al. (2004) y Gómez et al. (2005) discutieron la posibilidad de la existencia de un viento ionizado en IRAS 17347−3139, ya que el índice espectral de la emisión ($\alpha \simeq 0.7$; $S_\nu \propto \nu^\alpha$) así lo sugiere. Ellos estimaron que la tasa de pérdida de masa del viento ionizado tendría que

tener un valor de $\dot{M} \simeq 10^{-4}\ (D/\mathrm{kpc})^{3/2}\ M_\odot$ año^{-1}, el cual es mucho mayor al valor típico observado en otros objetos ($\sim 10^{-7}\ M_\odot$ año^{-1}, Patriarchi & Perinotto 1991). Incluso suponiendo que la emisión se origina en un viento colimado (Reynolds 1986), ellos encontraron que la tasa de pérdida de masa calculada es mucho mayor que para otras NPs. Debido a este resultado, de Gregorio-Monsalvo et al. (2004) y Gómez et al. (2005) propusieron que la emisión se está originando en la envolvente circunestelar ionizada de IRAS 17347−3139 y no en un viento ionizado.

Nuestras observaciones con mayor resolución angular sugieren la posibilidad de que sí exista un viento ionizado y colimado en IRAS 17347−3139. En las imágenes a 3.6 y 1.3 cm, la estructura extendida muestra una ligera simetría de punto (ver Figura 6). Este tipo de simetrías se han observado en varias NPs y objetos post-AGB, y han sido interpretadas como debidas a la presencia de un chorro colimado precesando (Velázquez et al. 2007). Además, en las imágenes infrarrojas se puede observar una estructura de *choque de proa* en el lóbulo norte, probablemente creada por la interacción del viento con la envolvente circunestelar. Para derivar la tasa de pérdida de masa del viento, usamos el tratamiento formulado por Reynolds (1986), y obtuvimos un valor de $\dot{M}_i \simeq 1.3{\times}10^{-5}\ (D/\mathrm{kpc})^{3/2}\ M_\odot$ año^{-1}. Este valor sigue siendo mayor que los observados en otras fuentes ($\sim 10^{-7}\ M_\odot$ año^{-1}); sin embargo, este exceso podría ser debido a que la emisión en la estructura extendida no sólo se origina en el viento ionizado, sino que también exista contribución de las paredes ionizadas de los lóbulos bipolares.

Adicionalmente a las observaciones de radio continuo, también realizamos observaciones espectrales de las transiciones de OH a $\lambda \simeq 18$ cm hacia la NP IRAS 17347−3139; detectamos emisión máser débil de la línea a 1612 MHz a una velocidad LSR $\mathrm{v_{LSR}} \simeq -70$ km s^{-1}. Esta emisión no muestra indicios de estar polarizada circularmente, por lo que no hay evidencia de la presencia de un campo magnético en esta fuente. Por otro lado, esta es la primera vez que se detecta emisión máser de OH a 1612 MHz a esta velocidad LSR en este objeto y que se puede confirmar su asociación espacial con la nebulosa. Zijlstra et al. (1989) reportaron emisión máser de la línea a 1612 MHz a una velocidad LSR ~ -125 km s^{-1} asociada con IRAS 17347−3139. Recientemente, como resultado de observaciones polarimétricas hacia varias NPs, Szymczak & Gérard (2004) también reportaron emisión máser de la línea a 1612 MHz hacia esta fuente, pero en los rangos de velocidad LSR: $-23{<}\mathrm{v_{LSR}}{<}5$ km s^{-1} y $-125{<}\mathrm{v_{LSR}}{<}-90$ km s^{-1}. Sin embargo, debido a la baja resolución angular de sus observaciones, la asociación espacial de esta emisión con la nebulosa

no quedó establecida de manera clara. Nosotros, además de la emisión débil a -70 km s^{-1} asociada con IRAS 17347−3139 ($S_\nu \simeq 40$ mJy[*****]), también detectamos emisión máser de la línea a 1612 MHz en los mismos rangos que las observaciones de Zijlstra et al. (1989) y Szymczak & Gérard (2004). Sin embargo, ya que nuestras observaciones tuvieron una resolución mayor a las previas, pudimos distinguir con mayor certeza la región donde los máseres se están originando y encontramos que esta emisión está asociada con las fuentes OH 356.65−0.15 y J17380406−313838. Este resultado esclarece el hecho de que apareciera emisión máser de OH en IRAS 17347−3139 con velocidades superiores a las típicas de expansión de las envolventes circunestelares.

Recientemente Gómez et al. (2008) han reportado la detección de otra nebulosa planetaria con emisión máser de agua, sumando así tres casos conocidos. Este tercer objeto también tiene morfología bipolar y los máseres se localizan en la región central. Uscanga et al. (2008) ha modelado los máseres de agua en K 3-35 con un disco en rotación y expansión que podría ser la clave en la colimación del viento y la producción de jets. Consideramos que es necesario continuar haciendo observaciones interferométricas hacia estas NPs con emisión máser de agua ya que la caracterización de discos o toroides alrededor de NPs podrían aportar información relevante acerca del mecanismo que produce los jets y otros tipos de morfologías asimétricas observadas en NPs.

En conclusión, no obstante que apenas se tienen tres casos confirmados de NPs con máseres de agua, vale la pena notar que todas tienen una morfología bipolar y los máseres provienen de la región central, posiblemente de un toroide. No es de extrañar que existan toroides compuestos de material molecular denso en la zona ecuatorial de la nebulosa que este escudando a las moléculas de agua de la radiación ionizante proveniente de la estrella central, además de mantener las condiciones físicas necesarias para que se produzca la emisión máser. Compartimos la sugerencia propuesta por Gómez et al. (2008), respecto a que este nuevo tipo de nebulosas planetarias llamadas H_2O-PN sean los precursores de las estrellas post-AGBs conocidas como water fountains.

[*****] 1 mJy=10^{-3}Jy; 1 Jy=10^{-23} erg cm^{-2} s^{-1} Hz^{-1}

Aramos arena de estrellas y nos tomamos el Universo en un vaso de agua.

Anónimo

1

Stellar Evolution and Formation of Planetary Nebulae

1.1 Stellar Evolution of low-mass stars

It is now well known that the planetary nebulae (PNe, and PN for singular) represent a phase in the evolution of low and intermediate mass stars ($M < 8M_{\odot}$). This type of stars spend most of their lives in a stage known as the *main sequence*, converting hydrogen into helium in their cores via thermonuclear reactions (position 1 in the Hertzsprung-Russell diagram of Figure 1.1). The type of nuclear reaction that leads to the formation of helium depends on the mass of the star; for stars with a mass $M \lesssim M_{\odot}$, the so-called *proton-proton chain* is the main mechanism responsible for production of energy:

$$\begin{aligned} \text{step 1}: \quad & \mathrm{p} + \mathrm{p} \quad \rightarrow \mathrm{D} + \nu, \\ \text{step 2}: \quad & \mathrm{D} + \mathrm{p} \quad \rightarrow {}^{3}\mathrm{He} + \gamma, \\ \text{step 3}: \quad & {}^{3}\mathrm{He} + {}^{3}\mathrm{He} \quad \rightarrow {}^{4}\mathrm{He} + \mathrm{p} + \mathrm{p}, \end{aligned}$$

where p represents a proton; D and He, denote the nuclei of the elements deuterium and helium, respectively; ν and γ, represent a neutrino and radiation, respectively. There are other two alternative reactions for the step 3 in the proton-proton chain, which also lead to the creation of helium; their importance in the creation of energy depends on the temperature of the core (Böhm-Vitense 1992 and references therein). For stars with a mass about 10-20% higher than the sun, another mechanism becomes dominant in the

production of energy; it is called the CNO cycle:

$$\begin{aligned}
\text{step 1}: \quad & {}^{12}\mathrm{C} + \mathrm{p} \rightarrow {}^{13}\mathrm{N} + \gamma, \\
\text{step 2}: \quad & {}^{13}\mathrm{N} \rightarrow {}^{13}\mathrm{C} + e^{+} + \nu, \\
\text{step 3}: \quad & {}^{13}\mathrm{C} + \mathrm{p} \rightarrow {}^{14}\mathrm{N} + \gamma, \\
\text{step 4}: \quad & {}^{14}\mathrm{N} + \mathrm{p} \rightarrow {}^{15}\mathrm{O} + \gamma, \\
\text{step 5}: \quad & {}^{15}\mathrm{O} \rightarrow {}^{15}\mathrm{N} + e^{+} + \nu, \\
\text{step 6}: \quad & {}^{15}\mathrm{N} + \mathrm{p} \rightarrow {}^{12}\mathrm{C} + {}^{4}\mathrm{He},
\end{aligned}$$

where C, N and O, represent the nuclei of the elements carbon, nitrogen and oxygen, respectively, and e^{+}, denotes a positron. In the case of the sun, only about 1% of the energy is produced through this reaction (Schwarzschild 1958).

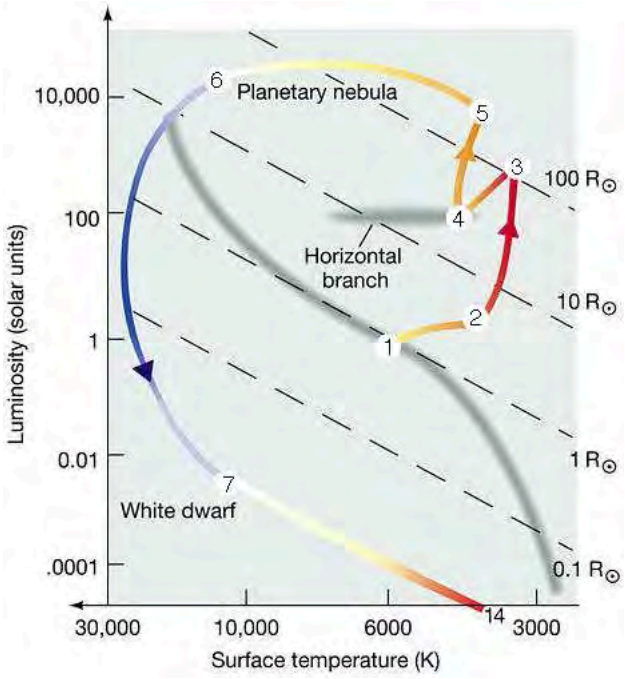

Figure 1.1: Hertzsprung-Russell diagram (see text for details).

When the hydrogen begins to deplete, and the core becomes richer in helium, the outward pressure force decreases, causing the core to contract under

the force of its own gravity. The energy liberated, due to the gravitational contraction, heats a shell just outside the core; the rate of nuclear reactions increases and the luminosity of the star also rises. This causes the outer layers of the star to expand greatly and become cooler. During this phase, the star moves up to the *red giant branch* (RGB) of the Hertzsprung-Russel diagram (position 2 of Figure 1.1).

At the tip of the RGB, the temperature in the stellar core is high enough for a different nuclear fusion process to take over; the helium nuclei are fused into heavier elements in a reaction called triple alpha (Salpeter 1952; position 3 of Figure 1.1):

$$\begin{aligned} \text{step 1}: \quad & {}^4\text{He} + {}^4\text{He} \rightarrow {}^8\text{Be} + \gamma, \\ \text{step 2}: \quad & {}^8\text{Be} + {}^4\text{He} \rightarrow {}^{12}\text{C} + \gamma. \end{aligned}$$

For high temperatures, other reactions also become possible, such as the following:

$$^{12}\text{C} + {}^4\text{He} \rightarrow {}^{16}\text{O} + \gamma.$$

At this point, the star begins to move to the *horizontal branch* (HB) of the Hertzsprung-Russell diagram (position 4 of Figure 1.1). The star remains in equilibrium in this stage for a period of time, until the helium begins to deplete in the core, which gets richer on heavier elements (C and O). If the star is not massive enough, it will develop a degenerated C-O core, evolving directly from the HB to the white dwarf stage (position 7 of Figure 1.1), without passing through the phases marked with the numbers 5 and 6 in Figure 1.1. On the other hand, if the star is massive enough, the core will contract and heat up, causing the rate of reactions to increase, similar to the RGB phase. The star will move up again, but this time on a path known as the *asymptotic giant branch* (AGB; between position 4 and position 5 of Figure 1.1). During this phase, an important fraction of the star's mass is lost through a slow-massive wind, with expansion velocities of ~ 10 km s^{-1} and mass-loss rates that can be as high as $\sim 10^{-4}\ M_{\odot}$ yr^{-1} (e.g., Knapp & Morris 1985; Winters et al. 2000). Finally, at the tip of the AGB phase (position 5 of Figure 1.1), the star experiences instabilities due to helium flashes in the core, which leads to the expulsion of the outer layers. The exposed core is called *post-AGB star*, and a detached slowly expanding circumstellar envelope is

formed around it. The low temperature and high density in the envelope favors the formation of various molecular species and dust grains; the central regions become completely obscured at visible wavelengths. During the post-AGB phase, the star evolves through the phase between the positions number 5 and 6 in Figure 1.1; the circumstellar envelope becomes visible in scattered light from the central star, and it is called *pre-planetary nebula or proto-planetary nebula* (pPN for singular and pPNe for plural). For low and intermediate-mass stars, the temperatures reached in the core of the central star are not enough for undergoing nuclear reaction of carbon and oxygen, however, when the surface temperature is around 25,000 K, large amounts of ionizing radiation are emitted; the expanding envelope is ionized, and the star enters to the *planetary nebula* phase (position 6 of Figure 1.1). As the ionized envelope continues expanding, its density decreases, until finally it is not visible anymore.

The hot stellar remnant left behind is called a white dwarf star (position 7 of Figure 1.1). This is the final fate of a low or intermediate-mass star, unless it belongs to a binary system, in such a case, the white dwarf star can experience mass accretion from its companion. The accreted material (basically hydrogen) falls onto the surface of the star; if the accumulated mass of the star does not reach the Chandrasekhar limit ($\sim 1.4\ M_{\odot}$), the gas is heated under degenerated conditions. This results in a thermonuclear runaway that provokes a sudden increase of the luminosity and the expulsion of the outer layers; this phenomenon is know as a nova explosion (see e.g. Starrfield et al. 1985). On the other hand, if the mass-accreting rate is high enough so that there is not time for the thermonuclear runaway to occur, and the accumulated mass of the star exceeds the Chandrasekhar limit, a deflagration of the carbon takes place. This leads to a violently conversion of carbon and oxygen into heavier elements inside the star, and it explodes as a Ia type supernova (see Nomoto et al. 1984).

1.2 Formation of Planetary Nebulae

When it was first proposed that PNe were the descendants of red giant stars, it was not clear how the circumstellar envelope was ejected. Some sudden ejection mechanisms, including pulsation instabilities (Kutter & Sparks 1974; Wood 1974; Tuchman et al. 1979), envelope relaxation oscillations due to thermal instability in the core (Smith & Rose 1972), radiation pressure

(Faulkner 1970; Finzi & Wolf 1971), or thermal pulses (Härm & Schwarzschild 1975; Trimble & Sackman 1978) were proposed to account for the detachment of the envelope. Although these sudden-ejection models seem reasonable to explain the appearance of PNe, none of them is quantitatively successful in ejecting the right amount of mass.

Furthermore, even if the PN is created through a sudden impulsive ejection, and additional pressure is required to maintain the expansion of the nebula. Several mechanisms were considered to be the driving force of the expanding nebula, such as pressure from the ionization front (Capriotii 1973; Wentzel 1976) or radiation pressure on grains (Ferch & Salpeter 1975). However, none was found to be adequate. The solution to these problems was found in a model proposed by Kwok et al. (1978), in which they suggest that the PN phenomenon does not represent a separate ejection of matter, but just a rearrangement of material ejected over the AGB phase.

1.2.1 The interacting stellar winds models

The first results that were qualitatively, as well as quantitatively consistent with the available observations were offered by *the interacting stellar winds* (ISW) model, proposed by Kwok et al. (1978). According to this model, once the slow and massive stellar wind (Slow Wind) of the AGB phase weakens, a much more tenuous (with mass-loss rates of $\sim 10^{-7} M_{\odot}$ yr^{-1}) but faster ($v_{ex} \sim 10^3$ km s^{-1}) wind takes over (Fast Wind). The latter wind reaches the former, interacting hydrodinamically and producing two shock fronts: one that propagates outwards, through the dense, slowly-expanding circumstellar envelope created by the Slow Wind; and other that propagates inwards, where the gas from the Fast Wind is shocked (See Figure 1.2). Under adiabatic conditions, the shocked gas heats up to temperatures $\sim 10^6$K, forming a hot bubble that expands outward and sweeps up the material in the circumstellar envelope. This results in the creation of a dense, expanding circumstellar shell around a very hot inner bubble. Once the central star is hot enough to produce large amounts of ionizing photons, the swept-up shell is ionized, and the planetary nebula is created. The predicted mass of the ionized shell as well as the expansion velocities were found to be consistent with the observations, making this model to seem promising at explaining the formation of planetary nebulae. Furthermore, it was expected that the hot bubble, predicted by the model, would emit X-ray continuum. Observations with X-ray telescopes corroborated such prediction, supporting once

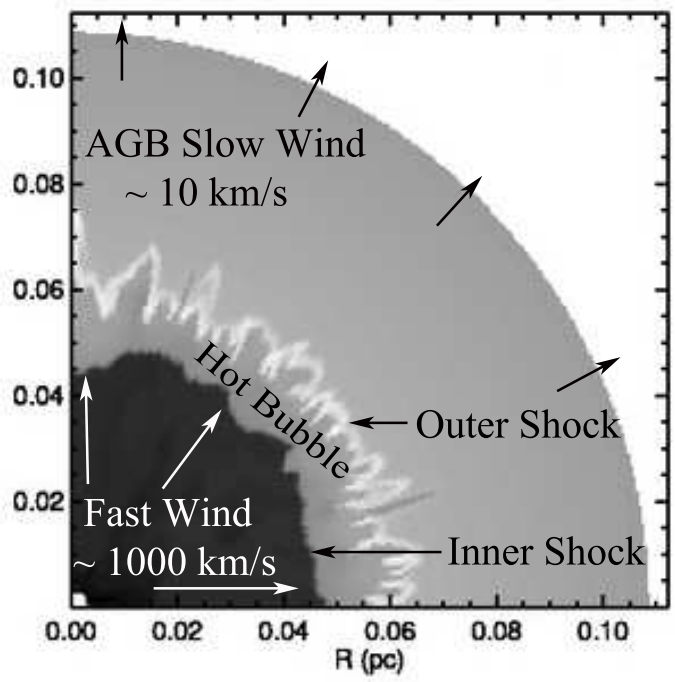

Figure 1.2: Interacting stellar winds model proposed to explain the formation of PNe by Kwok et al. (1978). This Figure has been adapted from García-Segura et al. (2006), where results of numerical simulations, using the interacting stellar winds model, are presented.

again this model.

The ISW model assumes that the Slow, as well as the Fast Wind, are spherically symmetrical; this results in the formation of a PN with the same symmetry. However, as higher sensitive and angular resolution observations were carried out, they revealed planetary nebulae with morphologies that departed from spherical symmetry, such as elliptical and bipolar shapes (e.g. Schwarz et al. 1992). To try to explain these morphologies, Calvet & Peimbert (1983) proposed the presence of a torus in the equatorial regions to deflect the winds toward a polar axis. Kahn & West (1985) demonstrated the viability of this mechanism, while the presence of such equatorial component was observationally confirmed (Balick 1987, Balick et al. 1987). Following these results, a series of analytical and numerical studies, including and enhancement of the density towards the equator, were made (Icke 1988; Icke

et al. 1989, 1992; Soker & Livio 1989; Frank 1994; Mellema 1994, 1995; and Mellema & Frank 1995). These calculations became known as the *generalized interacting stellar winds* (GISW) model (See Figure 1.3).

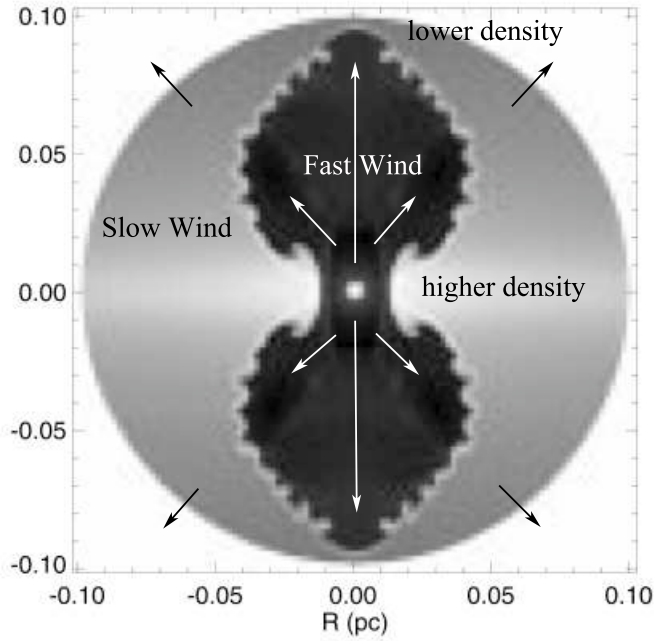

Figure 1.3: Generalized interacting stellar winds proposed to explain the formation of bipolar morphologies in PNe. The Fast Wind interacts with a circumstellar envelope in which the density is enhanced towards the equatorial region. Adapted from García-Segura et al. (1999).

Basically, in the GISW model it is assumed that the mass-loss rate of the Slow Wind in the AGB phase is a function of the latitude angle, being stronger in the equatorial region than toward the poles. This causes the density in the equator to be higher, in a sort of torus; when the isotropic Fast Wind takes over, it interacts with this structure; (similarly to the ISW model) a hot bubble of shocked gas is created, but in in the GISW model, the hot bubble expands preferentially toward the polar regions, where the density is lower, forming a bipolar structure (e.g. Kahn & West 1985; García-Segura et al. 1999). Under this scenario, the other observed morphologies (e.g. round, elliptical) can be explained as due to an effect of projection of the polar axis with respect to the line of sight.

The GISW model was able to explain the formation of elliptical and bipolar nebulae with wide waists. However, in the mid 1990's, the unprecedented high quality images of the the Hubble Space Telescope (HST) revealed structures present in PNe that challenged the GISW. One of the best examples is the Cat's eye nebula (upper left image of Figure 1 of Síntesis), which shows a complex system of bipolar structures with point-symmetry and some of them highly collimated. The GISW faces several problems when trying to explain this morphology, for example, there is no trace of an equatorial torus that would be deflecting the gas toward the polar regions, moreover, the presence of jet-like highly collimated structures cannot be explain under the standard assumptions of the GISW model. Currently, a plethora of observations show that the scenario including only two interacting winds is not adecuated to explain the shaping of pPNe and PNe but other mechanism should be included (see Balick & Frank 2002).

1.2.2 Magnetic fields, jets and binary systems

Since it is not possible to explain the development of narrow bipolar lobes with collimated structures by only considering the hydrodynamical interaction of two winds, other ingredients have been gradually added to the models of pPNe and PNe formation. Currently, there are many theoretical works that include the action of magnetic fields, the presence of collimated winds or jets from the central star, accretion in a binary system, etc. (Balick & Frank 2002). In many cases, these mechanisms have been successful at reproducing some characteristics of specific objects (e.g. García-Segura et al. 1999). Unfortunately, due to their difficulty, the observations that support the assumptions used in these models are sometimes scarce and not very conclusive.

Magnetic fields have been broadly used in the models to confine outflows within narrow structures in diverse cosmic sources (see e.g. Matt et al. 2003; Ferrari 1998). In particular, the *magnetized wind-blown bubble* model, developed by Chevalier & Luo (1994), has been used to reproduce the morphologies and structures observed in PNe (Różyczka & Franco 1996). This model assumes that a weak magnetic field is embedded in a spherically expanding fast wind; in the post-shock region, the compression strengthens the magnetic field, constraining the gas to move along the polar axis, and producing an elongated morphology in this direction. García-Segura (1997), García-Segura et al. (1999), and García-Segura & López (2000) have ad-

ditionally included the presence of an equatorial torus, in order to obtain higher degrees of collimation. In general, one important result from these works is that the highest degree of collimation is obtained for stars of higher mass. This is an interesting result, since it finds support in the observations (see e.g. Stanghellini et al. 2000). Another mechanism, proposed to launch collimated winds that could shape the axisymmetric nebulae, makes use of magneto-centrifugal forces (Blackman et al. 2001). In this model, the magnetic field is produced by a dynamo mechanism in a fast-rotating central star. The calculations show that the magnetic energy provided by this mechanism is enough to drive the collimated winds (Blackman et al. 2001) and it might even account for X ray emission observed in the central stars of some PNe. Furthermore, due to the coupling of the magnetic field to the stellar wind, angular momentum would be extracted from the central star, which would spin-down gradually; therefore, this model could explain the slow rotation observed in white dwarf stars.

The generation of strong magnetic fields via dynamo action in AGB stars has been discussed in works such Blackman et al. (2001) and Pascoli (1997). The presence of a binary system might be a crucial factor for producing an efficient dynamo that could account for the magnetic field necessary to launch and collimate outflows (Nordhaus & Blackman 2006). Some authors have remarked that magnetic fields cannot be solely the main agent for shaping axisymmetric planetary nebulae (e.g. Soker 2006).

The detection of magnetic fields in some AGB, as well as in pPNe and PNe has been encouraging to support the magnetic models. Recently, magnetic fields have been detected in AGB stars and in central star of PNe (Etoka & Diamond 2004; Jordan et al. 2005). In addition, polarimetric observations of maser emission of water and OH have provided evidence of the presence of magnetic fields in toroidal structures as well as along the axial bipolar outflows (Miranda et al. 2001; Vlemmings et al. 2006). These results are important to constrain the magnetic models, however, as Soker (2006) remarks, more detailed study is necessary to understand the role played by the magnetic fields in the shaping of pPNe and PNe.

1.3 Molecular and maser emission in evolved stars

As it was mentioned in §1.1, during the AGB phase, the star undergoes a strong mass-loss that leads to the formation of a dense circumstellar enve-

lope that expands slowly and whose extent can be as large as ~ 10 pc. Most of the molecules and dust grains in the galaxy are thought to be created in the envelopes of evolved stars. As the star evolves to white dwarf, passing through the pre-PN and PN phases, the circumstellar envelope suffers strong kinematical changes, as well as the effects of ionizing radiation. The physical conditions are drastically altered; its temperature and density are affected by shock and ionization fronts, many molecular species are destroyed, while others are created. Therefore, circumstellar envelopes represent a unique astrophysical laboratory where we can study the synthesis of cosmic chemical compounds. They have been widely studied through observations, which, due to the high extinction, are carried out mainly in the infrared, sub-millimeter and radio bands. The spectroscopic observations have revealed the presence of a rich variety of elements, molecules, and dust grains that are being excited under different physical conditions. Recently, the observations using interferometric techniques have provided images that show the spatial distribution of the different components in the envelope (Lucas & Guélin 1999). Moreover, this sort of observations also have enabled us to determine the kinematics within the wind. Probably one of the most striking results has been the discovery of bipolar high velocity outflows in the expanding envelope of the AGB phase, which was thought to be spherically symmetric. Maser emission has also been detected in the envelope of evolved stars; due to their small angular size, and their high intrinsic brightness, they have been an invaluable tool to understand the chemistry, physical conditions and kinematics of the envelope (See below). Following, we present a very basic description of the CSE, as it has been conceived from the models and observations.

1.3.1 Molecular distribution in the envelope of late-type stars

Within a distance of a few AU, molecular species, such as H_2, CO, C_2, CN, SiO H_2O, are formed. The kinematics in this region is thought to be dominated by density waves created in a pulsating atmosphere. Also, the material dredged up from the interior of the star is injected directly into this region, from where it is pushed slowly outwards. Depending on the importance of the convection underneath the atmosphere, the envelope will become rich in carbon (i.e. C/O>1). At a distance of $\sim$ 5-10 AU, where the temperature reaches values ~ 1000 K, the formation of dust grains becomes possible (See Figure 1.4). Dust is thought to be playing a major role in driving the wind in AGB stars (Fleischer et al. 1992; Sedlmayr 1994). Basically, the idea

is that radiation impinge on the dust grains, transferring momentum; consequently, the dust grains move away from the central star and drag the gas through collisional interactions, resulting in the expanding wind. The dusty circumstellar envelope can obscure completely the star, which can only be detected through the continuum infrared emission of the dust, as well as from emission of polyaromathic hydrocarbon bands. In the dust-forming region, some molecules, such as SiO, deplete completely into dust grains. As a consequence, maser emission from this molecule is expected to arise within this region (See Figure 1.4). This result has been confirmed observationally in several evolved stars (e.g. Chapman & Cohen 1986).

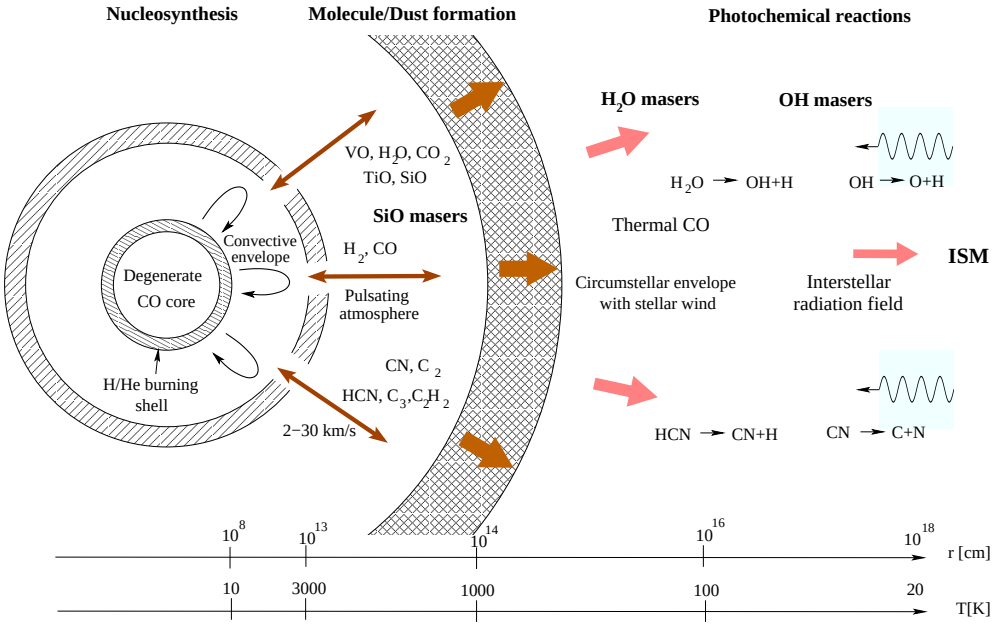

Figure 1.4: Schematic representation of the envelope of an AGB star.

In the region beyond the dust formation zone the molecules are blown toward the outer regions. As the optical depth decreases, the interstellar radiation can penetrate the wind, and photo chemical reactions take place; molecules such as CN or OH are created in this way (See Figure 1.4). This region is kinematically dominated by the expansion of the wind. The emission from molecules such as CO, HCO^+, HCN, show that the typical expansion velocity of the winds is about 15-20 km s^{-1}. In general, the molecules

trace spherical structures around AGB stars, indicating the regions were they are being created. A beautiful example is the carbon-rich star IRC+10216, in which the emission from different molecular species appear in concentric rings (Lucas & Guélin 1999). This morphology is also traced by the OH 1612 MHz maser emission, which arises in the outer regions of the wind (Booth et al. 1981). Recent VLBI observations of water masers in AGB stars have shown signs of bipolar symmetries in the inner regions of the wind (Nakagawa et al. private communication). This suggests that probably some axisymmetric mode of mass-loss is beginning to operate before the star leaves the AGB phase. The departure from spherically symmetric mass-loss becomes clearly evident in the pPNe phase, in which, for practically all the sources, the dispersed stellar radiation shows bipolar, or multipolar morphologies, with a dark equatorial lane. The molecular emission also trace bipolar or multipolar outflows with expansion velocities larger than the AGB wind ($v_{exp} \sim 50$km s^{-1}). Moreover, molecules also reveal equatorial structures, perpendicular to the bipolar outflows, expanding at $v_{exp} \sim 10$km s^{-1}. Bujarrabal et al. found that the energy and momentum of the outflows cannot be account only by considering radiation driven winds. Thus, other mechanism, such as probably magnetic fields might be playing a role in the acceleration of the outflows. H_2O and OH masers also reveal the presence of collimated outflows and jets in pPNe and PNe (Imai et al. 2002; Claussen et al. 2009). This emission has also been very useful to determine the presence of magnetic fields in the nebulae (Vlemmings et al. 2006; Gómez et al. 2009).

When the central star becomes hot enough to emit large amounts of ionizing photons, the molecules in the envelope are dissociated, except for those protected by some shielding mechanism (probably embedded in dense neutral clumps; e.g. Tafoya et al. 2007). It has been observed that when the ionization begins, the abundance of some molecular species increases. This indicates that the physicochemical conditions created by the ionization lead to the creation of new molecular species (Bachiller et al. 1997; Josselin & Bachiller 2003; Kwok 2009). It is also known that the maser emission also disappear as the star evolves toward the PN phase (See §1.3.2).

1.3.2 Maser emission in evolved stars

In the envelopes of oxygen-rich stars ([O/C]>1), molecules such as SiO, H_2O and OH are abundant, and they can produce strong maser emission (Reid & Moran 1981; Elitzur 1992a; Habing 1996). Due to their small an-

gular size and high intrinsic brightness, masers are a powerful tool to study very localized regions in the envelopes of the stars. The results from the maser theory regarding pumping mechanisms, can now be confronted with careful interferometric observations that reveal the location of the different masers within the circumstellar envelope (see Elitzur 1982; Elitzur 1992a). Statistical analysis that treat the maser stars as a stellar population have revealed interesting results, suggesting the possibility of setting out an evolutionary sequence by considering the appearance and disappearance of the different types of masers (Baud & Habing 1983; Lewis 1989, Gómez et al. 1990). Recently, with the development of efficient phase-referenced techniques in interferometry, and the improvement of very sensitive instruments, the possibility of measuring very small motions of masers in distant sources has become a reality (e.g. Imai et al. 2007; Claussen et al. 2009). From the apparent motion of maser spots, as measured from multi-epoch observations, it has been possible to determine the kinematics in the envelope of several evolved stars as well as their distances to the Sun. This last by means of the trigonometric parallax (e.g. Nakagawa et al. 2008). Apart from the valuable information for the understanding on the evolution of late-type stars, this results have enable the astronomers to gather information to create a map and determine the kinematics of the Milky Way. Thus, in the last years, the observations of stellar masers have played an important role in determining the distribution of dark matter in our Galaxy. Detailed reviews on maser emission in late-type stars can be found in works such as (Elitzur 1992a; Elitzur 1992b; Verschuur & Kellermann 1988, chapter 6); following we will discuss some generalities of the three strongest masers that typically arise in evolved stars.

SiO masers

The stellar SiO maser emission arises in vibration excited transitions, corresponding to temperatures higher than 2000 K (See Figure 1.5). Thus, the physical conditions to invert the populations of this molecule, as required to produce strong maser emission, can be maintained only in the close vecinity of a star. Furthermore, beyond the dust-formation region ($\sim$ 10 AU; see Figure 1.4), SiO molecules are completely depleted into dust grains (see §1.3.1). Consequently, SiO masers must arise near the surface of the star. This conclusion has been corroborated directly by interferometric observations which show the SiO masers appear located within a few AU from the central star

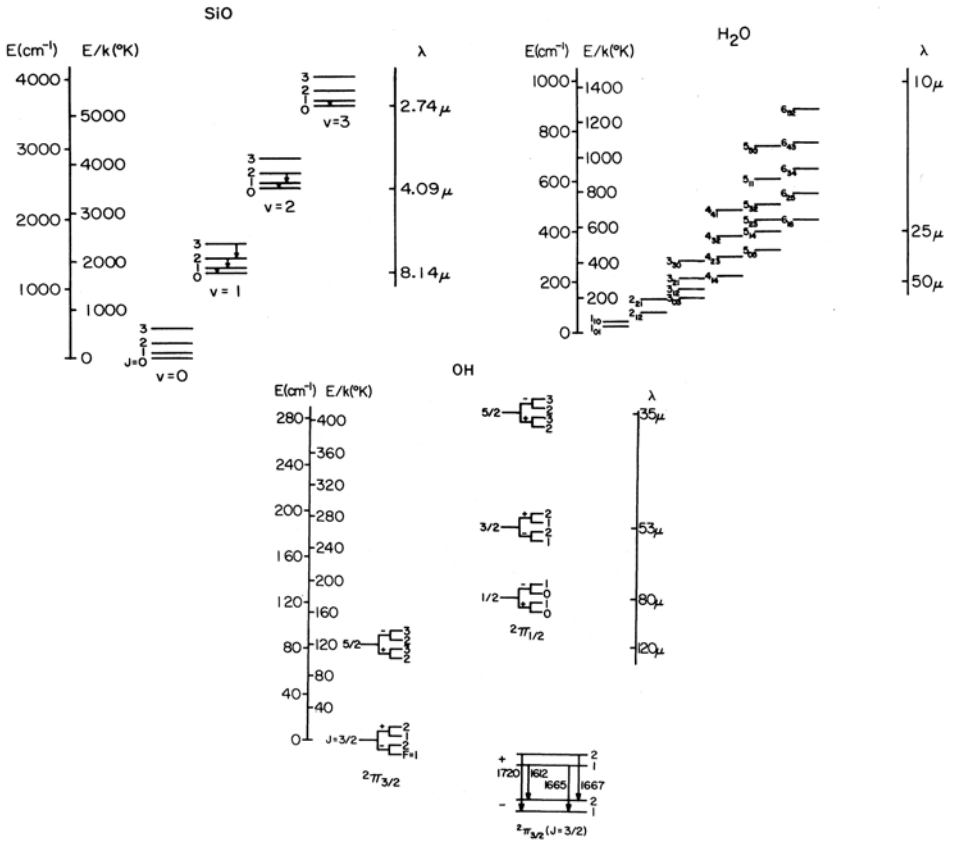

Figure 1.5: Energy levels for SiO, H_2O and OH molecules. For the SiO molecule, the vibration levels ($v \leq 3$) are shown. The common SiO and OH maser transitions are indicated with arrows. The most common maser transition for the H_2O molecule is $J=6_{16} \rightarrow 5_{23}$, which emits a photon with frequency $\nu \simeq 22$ GHz (adapted from Elitzur 1982).

(Moran et al. 1979).

The pumping mechanism for SiO masers is thought to be colisional rather than radiative. Observations of variable stars have revealed that SiO masers display periodic variations correlated with their visual magnitude, but in most cases they are shifted by a lag in phase of ~ 0.2 behind the visual maximum (Clark et al. 1984). This results are in conflict with radiative pumping by the stellar radiation. On the other hand, there seems to be a good agreement between the variability of the SiO masers and the in-

frared emission, which is also lagging bahind the visual light curve. This indicates that the SiO masers and the IR emission are arising in the same region of the atmosphere, however, there is no correlation at all between the average SiO and IR amplitude (Nyman & Olofsson 1986). This results, indicate that the IR radiation cannot trigger the inversion of populations of SiO molecules. Calculations made by Lockett & Elitzur (1991) show that the dominant pump mechanism is the collitions with neutral particules at a temperature $T \sim 120$ K and $n \sim 10^9$ cm^{-3}.

As an astronomical tool, SiO masers have been important to study the regions close to the stellar atmosphere of the AGB stars. They do not only provide us information of the physical conditions at distances within the dust-formation region, but also of the kinematics and polarization. Recently, using multi-epoch VLBI observations, Diamond & Kemball (1999) made a movie of the motion of SiO masers around the AGB star TX can. These results represent unique evidence showing the kinematics of a star at such small scales. Other works reporting polarization observations, have revealed the presence of magnetic fields with strenghs of tens of Gauss (Barvainis et al. 1987), these results provide valuable information on the dynamic agents present just above the photosphere of the star.

H_2O masers

In addition to SiO, the stellar atmosphere also has a high content of H_2O, since this molecule contains the bulk of the oxygen not tied up in CO. However, the H_2O masers cannot operate too close to the star because the high densities required for dust formation ($\sim 10^{10}$-10^{11} cm^{-3}) thermalize the populations of its rotation levels. This maser is expected to arise in further regions where the density has decrease to $\sim 10^8$-10^9 cm^{-3}. We also notice from Figure 1.5 that the rotation levels of the strong maser emission lie ~ 600 K above the ground level, indicating that the masers cannot arise further than $\sim 10^{15}$ cm (see Figure 1.4). On the other, the water photodissociation rate in the interestellar UV field is $P \sim 10^{-10}$ s^{-1}. If we consider a velocity of the wind of ~ 10 km s^{-1}, the disassication of H_2O molecules occurs at a distance of $\sim v/P \simeq 10^{16}$ cm, where the density of OH peaks. According to this approach, H_2O masers should be tracing the regions of the envelope where the stellar wind is launched. The association of the water masers with the stellar wind is supported by observations that show a predicted correlation of the maser luminosity with mass-loss rate (Bowers & Hagen 1984). Thus,

the study of this maser emission can add a greart deal to our understanding of the chemistry and the kinematics of the wind.

Usually, H_2O maser lines appear at velocities lower than those of the OH masers, confirming that the water masers are indeed arising in the inner regions of an accelerated wind. Observations have shown that the location of the masers is correlated with the mass-loss rate of the wind. Moreover, it has been observed a general trend of variability that correlates with the stellar cycle, however the water masers show a lag behind the IR and OH maxima by a phase of $\sim$ 0.1-0.2 (Engels et al. 1986), indicating that the that a radiative pumping mechanism could be ruled out. These results are in good agreement with detailed calculations made by Cooke & Elitzur (1985) that predict a location for the water masers of 10^{14} cm for $\dot{M} = 10^{-7} M_{\odot}$ yr^{-1} and 10^{15} cm for $\dot{M} = 10^{-5} M_{\odot}$ yr^{-1}. Furtehermore, these calculations also predict that the main pumping mechanism of the water masers should be through collitions with neutral particules in dense regions ($\sim 10^8$ cm^{-3}).

Due to their strong variability, the study of the kinematics of the wind through water masers observations is rather dificult. However, recent studies, carried out using VLBI techniques, have been succesful at tracing the proper motions of these masers in the envelopes of evolved stars. For AGB stars, these observations have revealed striking results, such as the discovery of bipolar expanding structures (Nakagawa, private comunication), allowing to study the development of axisimmetric modes of mass-loss. Other interesting discovery related to water masers in evolved stars are the so-called water fountain nebulae. These objects present water masers with velocities larger than those of OH, and that appear tracing collimated bipolar structures (Imai et al. 2002). From the measurement of the proper motions, expansion velocities up to $\sim$100 km s^{-1} have been derived, suggesting that a collimated jet is exciting the wate molecules. Polarimetric observations carried out by Vlemmings et al. (2006) toward the source W43, strongly suggest the presence of a magnetic field that could be confining the collimated jet that presumedly is sculpting the bipolar lobes. VLBI observations of H_2O masers have also allowed to directly measure the annual parallax of these sources, which translates into their distances. These results are assential to determine the physical parameters of the stars Furthermore, with the accurate determination of the distance, the location of the stars in our Galaxy is known; this information ca be widely used in other branches of astronomy. For example, a more accurate law for the period-luminosity relation of Mira variables can be obtained; this result translates in a better determination of

the cosmic distance ladder.

In 2001, Miranda et al. confirmed the first planetary nebula with water maser emission. This discovery cause astonishment since the conditions for pumping the water masers were not expected to be present in this evolutionary stage. The water maser emission was found in a sort of equatorial torus near the star, at a distance of ∼100 AU (similar to the distance at which this maser is found in AGB stars), and also at the tips of the bipolar lobes of K 3-35 (∼5000 AU). These later masers resemble those of the water fountain nebulae. Currently, there are other two PNe for which water maser emission has been confirmed. A detailed analysis of this emission should reveal information of the physical condition under which the masers are being pumped, and the kinematics of the gas in these nebulae.

OH masers

This is the first astronomical maser discoverd and so far the best studied. From Figure 1.5 we can see that the ground state $^2\Pi_{3/2}(J = 3/2)$ has four energy levels as a consequence of the interaction between the orbital and electron spin with the nuclear spin. Maser transitions can occur between these levels, resulting in the emission of lines at ν =1612, 1665, 1667, and 1720 MHz. As it was mentioned in §1.3.1, the OH forms in the expanding wind, when the H_2O molecules are photo-dissociated by interestellar UV radiation. Thus, it is expected that stellar OH masers arise at distances $\gtrsim 10^{16}$ cm (See Figure 1.4). On the other hand, the inversion of populations requires cycling of the molecules through excited rotation states whose corresponding temperatures range from 120 K to ∼400 K (see Figure 1.5). This requirement sets an upper limit for the distance at which the populations can be inverted via collisions, consequently, OH maser emission cannot arise at distances where the temperature is too low. This is not necessarely the case for the OH 1612 MHz maser, which has been observed to be tightly correlated with the stellar light curve, indicating that the pumping is predominantly radiative.

With the exception of the PN K 3-35, for which OH maser emission of the four transitions has been detected, late-type stars only show maser emission at 1612 MHz (satellite line) and 1665, 1667 MHz (main lines). The stars which are stronger in the main lines are called "type I" while those with stronger 1612 MHz emission are "type II". The later type has been studied more thoroughly so far, and the results have added great deal to our undarstanding of the evolution of evolved stars. In these objects, the OH 1612 MHz

maser line has a characteristic profile of two strong spikes separated in velocity by about 20-50 km s^{-1}. A prototype is the star IRC+10011, which is shown in Figure 1.6. The characteristic double-peak profile can be easily explained as maser emission from a shell in an expanding wind close to its terminal velocity; the radial acceleration is weak, resulting in velocity coherence mostly along radial rays. The blue- and redshifted components correspond to the front and back of the shell, respectively. The terminal velocity of the wind is given by twice the separation of the peaks and the mid-point corresponding to the systemic velocity of the star. This model has been widely verified by the observations. Particularly, two illustrative tests have been carried out with positive results. First, as Figure 1.6 shows, the emission from the extreme velocities fall at the map center while the emission from the central velocity components appear as portions of rings that are concentric with the map center. This is the strucuture expected for an dexpanding shell. The second test of the "front-back" emission model was suggested by Schultz et al. (1978). Assuming that both sides of the circmstellar envelope are excited simultaneously, the emission from the two peaks (arising in oposite sides of the shell) should vary in intensity in a similar manner. However, from the point of view of the observer on Earth, the emission from the far side of the shell should be delayed by the light travel time across the envelope relative to the blue-shifted emission from the near side of the star. Jewell et al. (1980) were able to demonstrate with certainty that the red component was indeed lagging behind the blue one, determining a lag for IRC+10011 as 25±5 days, corresponding to a shell radius of $\simeq 3 \times 10^{16}$ cm. Similar results have been published by Herman and Habing (1981), Diamond et al. (1985). These results provide one of only a handful of methods in astronomy that actually measure linear dimensions. Furthermore, by measuring the angular size of the shells, the distance to these sources have been obtained.

The OH masers of the main lines show very different characteristics from those of the sattelite line. Calculation of the pumping mecanisms indicate that these masers should be arising in different regions, since the populations are inverted under different conditions (Elitzur 1992b). The observations have shown that the maser emission of the main lines are present mainly in stars with low and its spatial distribution is more compact, similar to those of water masers. Since they are located closer to the star, the effect of magnetic fields is stronger, therefore, they have been used in polarimetric experiments to try to measure the strenght of the magnetic fields in evolved stars (e.g. Gómez et al. 2009).

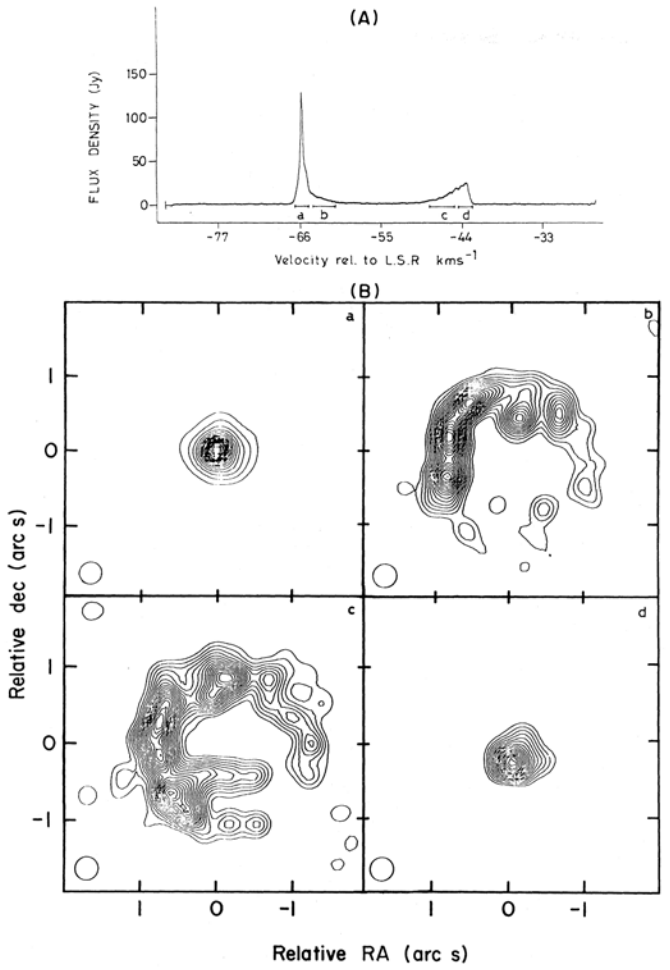

Figure 1.6: On top it is shown the spectrum of the OH 1612 MHz maser emission of the late-type star OH127.8. The bracketed velocity intervals correspond to the mapped emission that is shown in the bottom panel (Data from Booth et al. 1981).

Evolutionary sequence of the maser emission in evolved stars?

According to the evolutionary track of evolved stars, once the mass-loss rate of the Slow Wind at the tip of the AGB phase diminishes, the density of the circumstellar envelope would decrease. It is thus expected that the formation of molecules and dust would not be longer favored, on the contrary,

as the central star heats up, producing more ionizing photons, the molecules are dissociated. Although, near the photo-dissociated regions, some chemical processes could take place, creating new molecular species (Bachiller & Josselin 2003; Tafoya et al. 2007). Since the masers emission of the different molecular species arises in dense regions under very particular physical conditions, the evolution of the stars, characterized by changes in the mass-loss rate, density, temperature, etc. would be closely related with the presence of masers in the envelope.

An approach to understand the evolution of evolved stars by analysing the maser emission was taken by Baud & Habin (1983). The basic premise of the scheme used by these authors is that the OH 1612 MHz maser emission is predominantly controlled by $\dot{M}$, which is directly related to the time spent in the OH emitting phase. They found that the initial phase of the OH 1612 MHz maser emission occurs during an early stage of the wind, with a relatively mass-loss rate, $\gtrsim 3 \times 10^{-6} M_{\odot}\mathrm{yr}^{-1}$. As the stellar envelope loses mass, the mass-loss process accelerates until finally the star enters a superwind phase with $\dot{M} \geq 10^{-5} M_{\odot}\mathrm{yr}^{-1}$. De Jong (1983) performed a similar anaysis and reached similar overall conclusions. Anothe scheme was proposed by Lewis (1989) for the evolution of masers in the circumstellar shells of late-type stars. He also uses the mass-loss rate as the primary indicator for the presence of maser emission. Occording to his scheme, SiO, H_2O and OH main lines and finally OH 1612 MHz masers are added one by one in a chronological sequence as the mass-loss rate increases. He argues that except for the OH 1612 MHz line, the masers disspaear in the reverse order as the star evolves to the PN phase. Support to the basic premise of this chronological sequence has come from studies carried out by Stencel et al. (1990) and Gómez et al. (1990). The later authors found that, from a sample of 84 OH/IR stars, the percentage of objects with detectable H_2O and SiO mases emission decreases with increasing [25-12] color, which is thought to be an age indicator.

All truths are easy to understand once they are discovered; the point is to discover them.

Galileo Galilei

2

Emission mechanisms in Radio Astronomy

A remarkable property of matter is that it can interact with radiation, either emitting it, absorbing it, or simply dispersing it. A given particle (atom, ion or molecule) can transform part of its energy (ΔE) into a photon of frequency $\nu = \Delta E/h$, where h is the Planck constant. Conversely, the particle can absorb a photon of frequency ν, increasing its energy in the amount: $\Delta E = h\nu$.

A cosmic source is made up of an ensemble of particles that are constantly emitting, absorbing and dispersing radiation. The amount of energy emitted per unit of frequency or wavelength (i.e. the spectrum), by this source would be the net result of summing the contribution of all the microscopic processes taking place in it. In general terms, the resulting emission can be classified into two categories: continuum emission and line emission.

The former is produced when the ensemble of particles experience transitions from states with any given energy E_u to another with lower energy, E_l, in such a way that photons of all possible frequencies are emitted. On the other hand, line emission is produced when the particles undergo transitions between states with discrete values of energy (i.e. $E_j \rightarrow E_i$; $j = 1 \ldots \infty$, $i = 1 \ldots \infty$, and $j > i$), emitting photons of frequency $\nu_{ji} = (E_j - E_i)/h$.

2.1 Continuum emission at radio frequencies

In the astronomical context, particularly, in radio astronomy, it is common to divide the continuum emission into two categories: *thermal emission* and *non-thermal emission*.

2.1.1 Thermal emission

By definition, the thermal emission is that produced by matter, which is in thermal equilibrium, i.e. a single value of the temperature characterizes the matter and its surroundings (including radiation at all frequencies). In reality, this condition is never met by any object. However, an expression for the spectrum of a body that theoretically would be in thermal equilibrium can be found. This is the so called *blackbody* radiation. A blackbody is defined as an object, which absorbs all the radiation impinging on it. A good approximation of this situation is that of a cavity with a small hole. Every single ray of light entering the hole has very low probability of leaving without being absorbed, so the hole acts as a blackbody. The only photons coming from the hole will be those from the field of radiation in the cavity that is in thermal equilibrium with the walls. The energy transported by a beam of radiation, coming out of the hole, traveling within a unit of solid angle, crossing a unit of area, in a unit of time, and per unit of frequency (defined as the intensity I_ν, or brightness), would be given by the Planck law:

$$I_\nu^{BB} \equiv B_\nu(T) = \frac{2h\nu^3}{c^2}\frac{1}{\mathrm{e}^{h\nu/kT}-1}, \tag{2.1}$$

where c is the speed of light in vacuum, k is the Boltzmann constant, and T is the temperature of the walls of the cavity. In figure 2.1, the brightness from blackbodies at different temperatures are shown. In general, matter is not in thermal equilibrium with radiation. However, the intensity, at a given frequency, emitted by any body can be defined as follows:

$$I_\nu \equiv B_\nu(T_\mathrm{B}), \tag{2.2}$$

where, T_B, is defined as the *brightness temperature*.

For the range of frequencies within 1 and 100 GHz (between the dashed lines in Figure 2.1), and for temperatures higher than 1 K, we see that the emission increases as a power law of frequency ($B_\nu \propto \nu^2$). This is the Rayleigh-Jeans approximation. Under this regime, we have that:

$$\mathrm{e}^{h\nu/kT} \simeq 1 + \frac{h\nu}{kT} + \ldots, \tag{2.3}$$

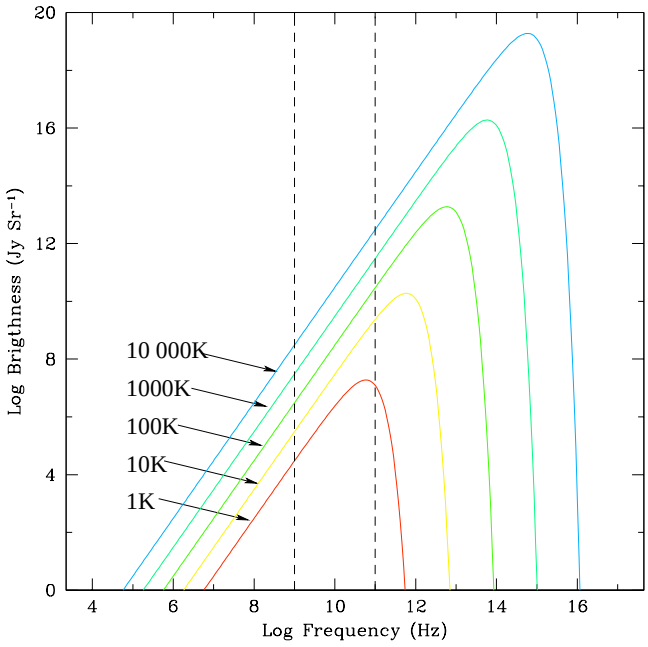

Figure 2.1: Planck law

which results in

$$B_{\rm RJ}(\nu, T) = \frac{2\nu^2}{c^2} kT, \tag{2.4}$$

$$\Rightarrow \qquad I_\nu \simeq \frac{2\nu^2}{c^2} kT_{\rm B}; \tag{2.5}$$

showing the power law dependence of the emission with the frequency. Eqn. 2.5 is commonly used by radio astronomers.

From Figure 2.1, we also note that, as the temperature of the blackbody increases, the emission reaches a maximum value at higher frequencies. This is the so-called *Wien's displacement Law*. A simple calculation shows that the frequency at which the emission, per unit of frequency, is maximum is given by:

$$\left[\frac{\nu_{\rm max}}{\rm GHz}\right] = 58.79 \left[\frac{T}{\rm K}\right]. \tag{2.6}$$

When the angular resolution of the radio telescopes allowed the identification of discrete radio sources in the sky, radio astronomers were able to investigate them separately, at different frequencies. It was found that, for some objects, the continuum flux density rises as a positive power law of the frequency ($S_\nu \propto \nu^\alpha$; $\alpha > 0$). This emission can be explain as arising in gas with a thermal velocity distribution, thus, it is called continuum thermal emission.

At radio frequencies, the continuum thermal emission is mainly produced by free electrons in ionized plasmas. The electrons interact with the protons due to the electric force between them; when they are deviated from their trajectories, they experience an acceleration and emit photons (see Figure 2.2). This type of emission is called *free-free emission*, or *thermal bremsstrahlung emission* (bremsstrahlung, in German, means braking radiation).

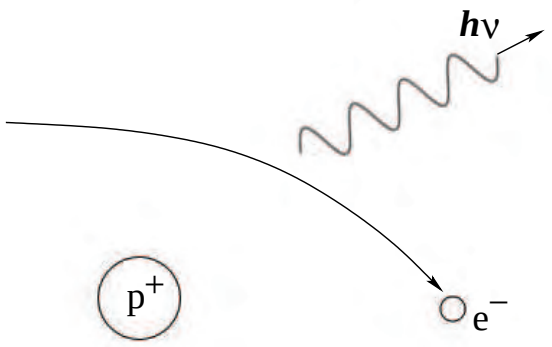

Figure 2.2: Free-free emission.

Thermal bremsstrahlung emission

A plasma is a tenuous ionized gas at high temperature, for which we can consider that the interactions between the particles is due predominantly to long distance electric forces. Astronomically, plasmas are made basically of ionized hydrogen, so we can consider that the only particles present are electrons and protons.

The possible electric interactions that can take place are the following:

$$e^- + e^- \rightarrow e^- + e^- + \gamma,$$
$$p^+ + p^+ \rightarrow p^+ + p^+ + \gamma,$$
$$e^- + p^+ \rightarrow e^- + p^+ + \gamma.$$

However, a simple analysis shows that the second derivative, with respect of time, of the dipolar moment ($\mathbf{d} = \sum e_i \mathbf{r}_i$), in the first two types of interaction is zero. Therefore, the dipolar power radiated, given by the Larmor equation,

$$P = \frac{2\ddot{d}^2}{3c^3}, \tag{2.7}$$

is also zero (there is quadrupolar emission, however it is too weak).

On the other hand, for the interaction between a proton and an electron, the second derivative of the dipolar moment is approximately:

$$\ddot{\mathbf{d}} \simeq -e\ddot{\mathbf{r}}_e. \tag{2.8}$$

From this point, to derive the emission coefficient (i.e. the amount of energy emitted per unit of volume, time and frequency), we will follow the analysis form chapter 5 in Rybicki and Lightman (1979). To simplify the calculations, it is assumed that the interactions ("collisions") occur in a small interval of time and that the trajectories of the electrons are not affected significantly, and can be assumed to be linear. For thermal bremsstrahlung emission, the expression for the radiation of a single electron is averaged over a Maxwellian velocity distribution resulting in the following expression for the emission coefficient:

$$\epsilon_\nu^{ff} \equiv \frac{dW}{dV\ dt\ d\nu} = \frac{2^5 \pi e^6}{3mc^3} \left(\frac{2\pi}{3km}\right)^{1/2} T^{-1/2} Z^2 n_e n_i \mathrm{e}^{-h\nu/kT} \bar{g}_{ff}, \tag{2.9}$$

where m and e are the mass and charge of the electron, respectively; Z is the charge of the ion nuclei (Z=1 for ionized hydrogen), n_e and n_i are the density of the electrons and ions, respectively; and $\bar{g}_{ff}$ is the *Gaunt factor*. This factor includes the information related to the upper and lower limits in the integration over all the possible the impact parameters of the collisions. At radio frequencies, an analytic approximation of the Gaunt factor, given

by Altenhoff (1960), can be used:

$$\bar{g}_{ff} = 11.95\, T^{0.15}\nu^{-0.1}, \tag{2.10}$$

which is accurate to within a factor of 25% for $T < 10^4$ K and $\nu < 100$ GHz. In the radio frequencies regime, for ionized hydrogen, using this value of the Gaunt factor, dividing by the 4π, and evaluating in CGS units; from equation 2.9, we obtain the emission coefficient per unit of solid angle:

$$j_\nu^{ff} \equiv \frac{\epsilon_\nu^{ff}}{4\pi} = 6.5 \times 10^{-38} n_e^2\, T^{-0.35}\nu^{-0.1} \text{ ergs cm}^{-3} \text{ Hz}^{-1} \text{ s}^{-1} \text{ sr}^{-1}. \tag{2.11}$$

Finally, according to Kirchoff's law, for thermal emission, the absorption coefficient is given by:

$$\kappa_\nu^{ff} = j_\nu^{ff}/B_\nu(T), \tag{2.12}$$

which, for the radio frequencies regime, when evaluated in CGS units results as:

$$\kappa_\nu^{ff} = 0.21\, n_e^2\, T^{-1.35}\nu^{-2.1} \text{ cm}^{-2}. \tag{2.13}$$

2.1.2 Thermal emission from a homogeneous HII region

As mentioned above, in most astronomical cases, the ionized gas is basically made of hydrogen, hence the ionized regions are called HII regions (although there are some situations where this approximation is not applicable). These regions are associated to different sources of ionizing photons. For example, in the regions of massive star formation, when the *protostars* begin to emit large amounts of photons with energies larger than 13.6 eV (the ionization potential of the hydrogen), the circumstellar gas is ionized, forming an HII region surrounding the newborn star. On the other hand, at the end of their lives, low-mass stars form a dense circumstellar envelope through a massive stellar wind (see Chapter 1). When the core gets hot enough, it begins to produce copious amounts of ionizing photons which form an HII region, known as a planetary nebula. There are many other astronomical situations for which an HII region arises, however, in this thesis we will focus our attention only on those associated with PNe.

First, we consider the radiative transfer equation:

$$\frac{dI_\nu}{ds} = -\kappa_\nu I_\nu + j_\nu. \tag{2.14}$$

This equation basically states two things: as a beam of radiation travels a path ds, the intensity decreases proportionally to the product of the absorption coefficient and the intensity itself, and it increases proportionally to the emission coefficient.

Now, we define a very useful concept, the *optical depth* (τ_ν):

$$\tau_\nu(s) \equiv \int_{s_0}^{s} \kappa_\nu ds. \tag{2.15}$$

Intuitively, the optical depth represents the number of absorptions that a photon of a given frequency, ν, would experience when crossing a path of length $|s - s_0|$.

Using this definition in equation 2.14, we obtain:

$$\frac{dI_\nu}{d\tau_\nu} = -I_\nu + \mathcal{S}_\nu, \tag{2.16}$$

where $\mathcal{S}_\nu$ is known as the *source function*, and it is defined as: $\mathcal{S}_\nu \equiv j_\nu/\kappa_\nu$. The general solution for this differential equation is the following:

$$I_\nu(\tau_\nu) = I_\nu(0)\ \mathrm{e}^{-\tau_\nu} + \int_0^{\tau_\nu} \mathcal{S}_\nu\ \mathrm{e}^{-(\tau_\nu - \tau'_\nu)} d\tau'_\nu. \tag{2.17}$$

Since we are considering a homogeneous HII region, $\mathcal{S}_\nu$ is constant throughout the source and the solution of this equation is:

$$I_\nu(\tau_\nu) = I_\nu(0)\ \mathrm{e}^{-\tau_\nu} + \mathcal{S}_\nu\ (1 - \mathrm{e}^{-\tau_\nu}). \tag{2.18}$$

For the case of thermal emission from an HII region, $\mathcal{S}_\nu = B_\nu(T)$ (eq. 2.12), and we obtain:

$$I_\nu(\tau_\nu) = I_\nu(0)\ \mathrm{e}^{-\tau_\nu} + B_\nu(T)\ (1 - \mathrm{e}^{-\tau_\nu}). \tag{2.19}$$

The optical depth can be obtained by integrating equation 2.15, using

equation 2.13:

$$\tau_\nu = \int_0^s \kappa_\nu ds = 0.08235 \left[\frac{EM}{\mathrm{cm}^{-6}\ \mathrm{pc}}\right] \left[\frac{T_e}{\mathrm{K}}\right]^{-1.35} \left[\frac{\nu}{\mathrm{GHz}}\right]^{-2.1}, \qquad (2.20)$$

where $EM = \int n_e^2\, ds$, and it is called the emission measure. For the homogeneous case, the flux density, S_ν, is obtained simply as follows:

$$S_\nu = \int_{\Omega_s} I_\nu\, d\Omega = I_\nu\, \Omega_s, \qquad (2.21)$$

where Ω_s is the solid angle subtended by the source. For a weak background source, using 2.19, we have that:

$$S_\nu = I_\nu\, \Omega_s = B_\nu(T)\, \Omega_s\, (1 - \mathrm{e}^{-\tau_\nu}), \qquad (2.22)$$

and when we consider equations 2.1 and 2.20, the flux density of a distant homogeneous source can be computed. Equation 2.20 shows that the optical depth for free-free emission is an inverse function of the frequency of observation, i.e. for low frequencies, $\tau_\nu \gg 1$, and $\mathrm{e}^{-\tau_\nu} \sim 0$; for this case we have that $S_\nu \propto \nu^2$. On the contrary, at higher frequencies, $\tau_\nu \ll 1$, $(1-\mathrm{e}^{-\tau_\nu}) \sim \tau_\nu$, and $S_\nu \propto \nu^{-0.1}$ (see Figure 2.3).

Thermal emission from a Non-homogeneous HII region

It is usually a good approximation to consider HII regions with a electron density profile that is a power law of the radius ($n_e \propto r^{-n}$). We will consider cases for which the ionization fraction is 1 (i.e. completely ionized hydrogen), and the electron temperature is constant. From equation 2.20, we see that the optical depth depends not only on frequency but also on the square of the electron density integrated along the path of a given line of sight (the emission measure). Then, at a given frequency of observation, since the electron density decreases with increasing radius, there will be a line of sight with impact parameter, r_1, for which $\tau_\nu(r_1) = 1$; for $r < r_1$,$\tau_\nu > 1$, and for $r > r_1$,$\tau_\nu < 1$ (see Figure 2.4). In the case of stellar winds, as those present in the last stages of stellar evolution (Chapter 1), the density profile of the gas has a power law dependence of $n \propto r^{-2}$. For this particular situation, to find the value of r_1 as a function of frequency, in equation 2.20, we set

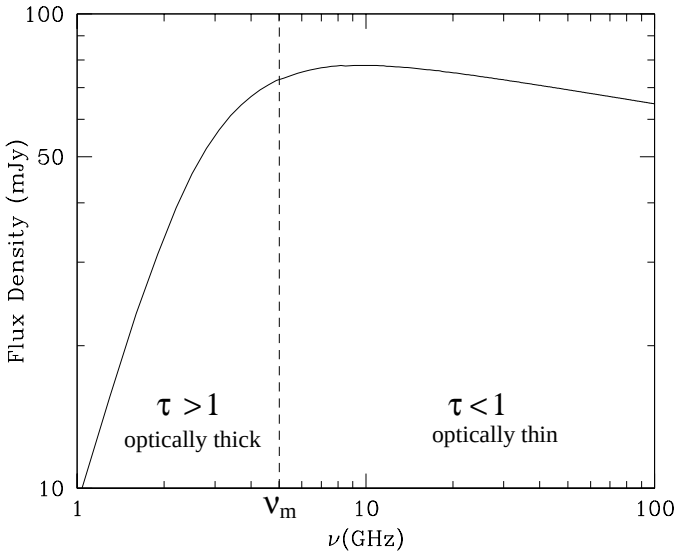

Figure 2.3: HII region spectrum.

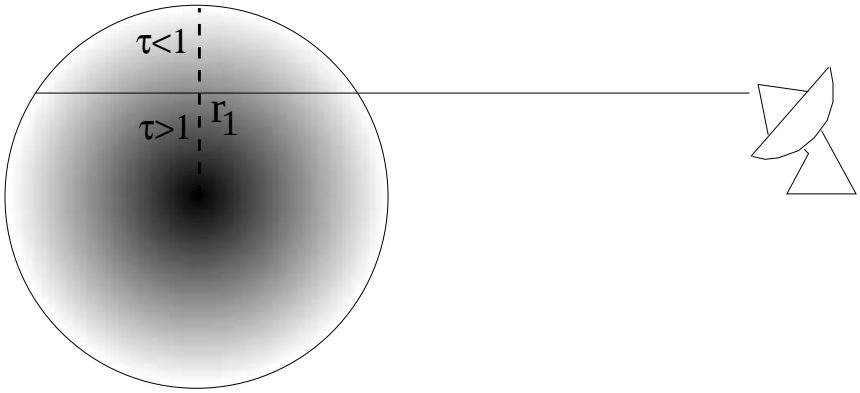

Figure 2.4: Non-homogeneous HII region.

$\tau_\nu = 1$, which results in:

$$1 = \tau_\nu(r_1) \quad \propto n_e^2(r_1) r_1 \nu^{-2.1} \propto r_1^{-4} r_1 \nu^{-2.1}$$
$$\Rightarrow r_1 \propto \nu^{-0.7}.$$

This shows that, as one observes at higher frequencies, the radius (therefore the solid angle) within which the emission is optically thick, decreases. This implies that the region from which the emission is optically thin, grows in size. The flux density of the *thick region* is given by:

$$S_\nu^{\rm thick} = I_\nu\ \Omega_{\rm thick} \propto \nu^2 r_1^2 \propto \nu^2 \nu^{-1.4}$$
$$\Rightarrow S_\nu^{\rm thick} \propto \nu^{0.6},$$

and the same dependence can be found for the *thin region* ($S_\nu^{\rm thin} \propto \nu^{0.6}$; frequency range within the dashed lines in Figure 2.5). For a theoretical

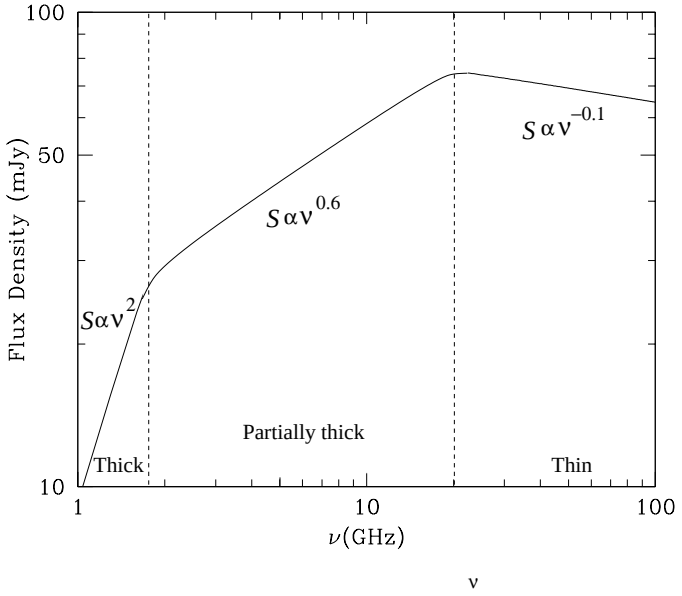

Figure 2.5: HII region spectrum.

region with a power law dependence $n \propto r^{-2}$, the density increases to an unlimited value when $r \to 0$. On the other hand, the regions extends to an unlimited radius. However, in reality the density reaches a maximum value at the center of the region, and there is an outer radius at which the density can be considered to become zero (e.g. the radius at which the ionized gas is not present anymore). When the observations are carried out at a frequency such

that $r_1 = 0$, the whole region becomes totally optically thin. The dependence of the flux density with the frequency becomes $S_\nu \propto \nu^{-0.1}$ again. At lower frequencies, when $r_1 = R_{\rm region}$, the whole region becomes optically thick, and the flux density increases with frequency as $S_\nu \propto \nu^2$ (see Figure 2.5).

Reynolds (1986) presented calculations for the case of an ionized wind that can be constrained to narrow opening angles. His equations also consider the presence of gradients in the opening angle, temperature, density and ionization fraction. He finds that for the case of constant opening angle (i.e. conical wind), density power law $n \propto r^{-2}$, and letting the temperature, and ionization fraction constant, the dependence of the flux density with frequency is the same as the spherical wind. However, he finds that the mass-loss rate derived for the collimated wind can be much lower than for the spherical case (equation 21 from Reynolds 1986):

$$\frac{\dot{M}({\rm jet})}{\dot{M}({\rm spherical\ wind})} = 0.20\theta_0({\rm sin}i)^{-1/4}, \qquad (2.23)$$

where θ_0 is the opening angle of the collimated wind, and i is the angle between the line of sight and the plane of the sky. The dependence of the flux density with frequency can be different from 0.6 if one takes into account the possible gradients of the physical parameters of the wind (see Table 1 of Reynolds 1986).

2.1.3 Non-thermal bremsstrahlung emission

This emission arises from matter that is not in thermal equilibrium. Basically, it can be said that the velocity distribution of the particles responsible for the emission (mainly electrons) is not Maxwellian. There are several mechanisms that produce non-thermal emission, but astrophysically, one can be considered as the dominant: *synchrotron emission* or *magnetic bremsstrahlung emission*.

This emission arises when free electrons move at relativistic velocities around lines of magnetic field. Since the electrons move in curved trajectories, they experience acceleration and radiate energy in the form of photons. This emission is mainly produced in the nuclei of active galaxies, in the magneto spheres of some kind of stars and in the remanents of supernovae. In the objects that we will study in this thesis, this emission does not play an important role and we will not discuss this type of emission with more detail.

2.2 Line emission

So far, we have discussed the mechanisms and emission processes that involve particles (mainly electrons) that experience transitions between states which have energy with any value. Now we will discuss some processes in which the transitions take place between states with a specific value of energy. The transitions take place in systems with quantized levels of energy: atoms, ions, molecules, etc. For example, the electron in a hydrogen atom revolves around the proton in orbitals with specific given energies; when the electron changes from the state with quantum number n=3 to that with n=2, a photon with a wavelength of 6562.8Å is emitted (Hα). A well known transition in the radio regime is that of the electron in an atom of hydrogen that changes its spin direction from parallel to anti-parallel, with respect to that of the proton. When this transition occurs, a photon with a frequency of 1.42 GHz ($\lambda \simeq 21$ cm) is produced. There are many other transitions that produce photons at radio frequencies, but we will concentrate only on rotational transitions in molecules.

Consider two states with energies E_j and E_i respectively ($E_j > E_i$). If we think of only the transition between these two levels (i.e. there are no processes producing transitions from other levels), there are five mechanism responsible for the transition between these two states: radiative excitation, stimulated decay, spontaneous decay, collisional excitation and collisional decay. The first two processes occur when there is a field of radiation present and the particles interact with a photon of energy $\Delta E = E_j - E_i$. If the particle is in the state with energy E_i, it will absorb the photon and will be *excited* to the state with higher energy E_j. On the contrary, if the initial state of the particle has energy E_j, the photon has a probability of *stimulating* it to emit a photon of the same energy. Furthermore, the particle in the state with energy E_j has a probability of *spontaneously* decay to the state with energy E_i, emitting a photon. Finally, since the particles are moving with a distribution of velocities, they can collide with each other. If there is an exact exchange of energy during the collision of $\Delta E = E_j - E_i$, a transition between the two states will occur. The probability of a transition between these two states is completely described by the *Einstein coefficients* and the *collisional rates* (see Figure 2.6).

Radiative transitions

First, consider the radiative transitions between the two states mentioned above. The process that populates the state with energy E_j is the absorption

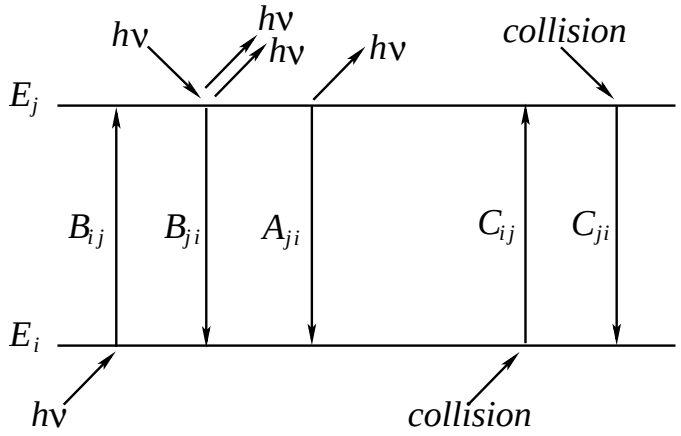

Figure 2.6: Transition between two levels.

of photons with frequencies $\nu = (E_j - E_i)/h$. Then, the Einstein coefficient B_{ij} is defined such that the rate at which the level j is populated is given by:

$$\dot{n_j} = -\dot{n_i} = n_i B_{ij} I_\nu, \tag{2.24}$$

where n_j and n_i are the densities of particles in the levels j and i, respectively. The are two radiative processes that populate the state with energy E_i: spontaneous, and stimulated emission. The Einstein coefficient B_{ji}, is related to the stimulated emission and it is defined such that, the rate at which the level i is populated is given by:

$$\dot{n_i} = -\dot{n_j} = n_j B_{ji} I_\nu. \tag{2.25}$$

Despite that the stimulated emission mechanism produces radiation; during this process, photons from the field are taken. The stimulated emission is then accounted as a negative absorption so that the absorption coefficient can be written as follows:

$$\kappa_\nu = \frac{n_i B_{ij} - n_j B_{ji}}{4\pi} h\nu_{ji}\phi(\nu), \tag{2.26}$$

where $\phi(\nu)$ is called the *line profile*, discussed below.

The rate at which level i is populated due to spontaneous transitions is

characterized by the Einstein coefficient A_{ji}, such that:

$$\dot{n_i} = -\dot{n_j} = n_j A_{ji}, \tag{2.27}$$

and the emission coefficient is written as follows:

$$j_\nu = \frac{n_j A_{ji}}{4\pi} h\nu_{ji}\phi(\nu). \tag{2.28}$$

A relation between the Einstein coefficients can be found when one considers the case of thermal equilibrium. In such situation the population of the levels is given by:

$$\frac{n_j}{n_i} = \frac{g_j}{g_i} \mathrm{e}^{-h\nu_{ji}/kT}, \tag{2.29}$$

where g_j and gi are the statistical weights of the levels j and i, respectively. Therefore, for the limit when $T \to \infty$, we obtain that:

$$g_i B_{ij} = g_j B_{ji}. \tag{2.30}$$

In thermal equilibrium, we also have that the populations in each level remain constant, and that the distribution of radiation is given by Planks law; this leads to:

$$n_j A_{ji} = (n_i B_{ij} - n_j B_{ji}) B_\nu(T), \tag{2.31}$$

$$\Rightarrow \qquad A_{ji} = \frac{2h\nu_{ji}^3}{c^2} B_{ji}. \tag{2.32}$$

Although the relations were obtained for the particular case of thermal equilibrium, they are valid for all cases, since the coefficients are intrinsic properties of the particles.

Line broadening mechanisms

The line profile is included because the particles do not absorb or emit photons of one single frequency. The line profile is the result of various mechanisms that broaden the line such as *natural broadening*, *Doppler broadening* and *Kinematic broadening*.

- Natural broadening: The Heisenberg's uncertainty principle states that one cannot determine the energy of a system with more precision than $\Delta E \sim \hbar/\Delta t$. Hence, the line will have a dispersion in frequencies of the

order of $\Delta\nu \simeq (2\pi\Delta t)^{-1}$, where Δt is the lifetime of the particle in a given level. At radio frequencies, this broadening is so small that it is considered negligible.

- Doppler broadening: The ensemble of particles have a distribution of velocities. Consequently, each particle will absorb or emit a photon that, in its particular rest frame, has frequency $\nu = (E_j - E_i)/h$. However, due to Doppler effect, from the frame of reference of the observer, there will be a dispersion of frequencies. For a Maxwellian distribution of velocities, this effect will lead to a broadening of the line of:

$$\Delta\nu_{th} = \sqrt{\frac{8\ln 2 k T_{\rm k} \nu_0^2}{mc^2}}, \tag{2.33}$$

  where $T_{\rm k}$ is the kinetic temperature, characterizing the Maxwellian distribution; m is the mass of the particles, and c is the speed of light in vacuum.

- Kinematic broadening: This mechanism is similar to the Doppler broadening; however, it is not due to the Doppler effect resulting from the distribution of velocities of the ensemble of particles, but to the bulk motion of some parts of the emitting region. For example, for an isotropically expanding gas, the particles approaching the observer will have positive velocities and, due to Doppler effect, will absorb or emit photons with shorter wavelengths. On the other hand, the particles moving away from the observer will absorb or emit photons with longer wavelengths. In the case of the envelopes of evolved stars, this mechanism is the most important for broadening the lines, and the resulting profile is a result of the kinematics of the emitting material.

In astronomy, the broadening of the lines is commonly expressed in terms of velocity. For non-relativistic Doppler effect, the transformation from frequency to velocity is given by the following expression:

$$\frac{\Delta\nu}{\nu_0} = \frac{\Delta v}{c}. \tag{2.34}$$

Collisional transitions

The other mechanism responsible for the transitions between levels of energy

is the collisions between particles. The rate at which the level j is populated due to this mechanism is written as:

$$\dot{n_j} = -\dot{n_i} = n_i C_{ij} - n_j C_{ji}, \tag{2.35}$$

where C_{ij} and C_{ji} are the collisional rates (see Figure 2.6). These rates are defined as the product between the overall density of particles n, and the collision rate coefficients γ_{ij} and γ_{ji}, respectively. Note that the particles that dominate the collision rates may not be the system particles. For example, while one observes lines of the transitions of CO, the collisions in the gas could be dominated by H_2 molecules. For a Maxwellian distribution of velocities of the particles, the collision rate coefficients can be expressed by the following expression:

$$\left[\frac{\gamma_{ji}}{\mathrm{cm^{-3}\ s^{-1}}}\right] = 1.45 \times 10^{-11} \left[\frac{\sigma_{ji}}{10^{-15}\ \mathrm{cm^{-2}}}\right] \left[\frac{m}{m_{\mathrm{H}}}\right] \left[\frac{T_{\mathrm{k}}}{\mathrm{K}}\right], \tag{2.36}$$

where σ_{ji} is the corresponding collision cross section. The collision rate coefficients are not independent; when $n \to \infty$, the collisions are the dominant mechanism producing transitions, and for thermal equilibrium we have that:

$$n_i C_{ij} = n_j C_{ji}, \tag{2.37}$$

and the ratio of populations is given by the Boltzmann function, therefore we obtain that:

$$C_{ij} g_i = C_{ji} g_j \mathrm{e}^{-h\nu_{ji}/kT}, \tag{2.38}$$

$$\Rightarrow \quad \gamma_{ij} g_i = \gamma_{ji} g_j \mathrm{e}^{-h\nu_{ji}/kT}. \tag{2.39}$$

Out of equilibrium, it can be shown that this expression holds for the kinetic temperature:

$$\gamma_{ij} g_i = \gamma_{ji} g_j \mathrm{e}^{-h\nu_{ji}/kT_{\mathrm{k}}}. \tag{2.40}$$

We have now considered all the relevant mechanisms that produce transitions between two energy levels of a particle. Then, we can write the rate at which a given level j is populated as:

$$\dot{n_j} = n_i(B_{ij} I_\nu + C_{ij}) - n_j(B_{ji} I_\nu + A_{ji} + C_{ji}). \tag{2.41}$$

2.2.1 Thermal line emission at radio frequencies

Considering again the situation that only transition between the two levels i and j can occur, in the steady state we will have that $\dot{n}_j = 0$. If we neglect the radiation field, equation 2.40 gives:

$$n_i(B_{ij}I_\nu + C_{ij}) = n_j(B_{ji}I_\nu + A_{ji} + C_{ji}) \tag{2.42}$$

$$\Rightarrow \qquad \frac{n_j}{n_i} = \frac{B_{ij}I_\nu + C_{ij}}{B_{ji}I_\nu + A_{ji} + C_{ji}}. \tag{2.43}$$

For $n \to \infty$, the collisions will be dominant and, using equation 2.41, we will have that:

$$\frac{n_j}{n_i} \to \frac{C_{ij}}{C_{ji}} = \frac{g_j}{g_i}\mathrm{e}^{-h\nu_{ji}/kT_\mathrm{k}}. \tag{2.44}$$

We notice that the excitation temperature is defined in such a way that the ratio of populations of these levels is written as:

$$\frac{n_j}{n_i} = \frac{g_j}{g_i}\mathrm{e}^{-h\nu_{ji}/kT_\mathrm{ex}}. \tag{2.45}$$

This means that, as $n \to \infty$, $T_\mathrm{ex} \to T_\mathrm{k}$, i.e. the populations approach the Boltzmann distribution at the kinetic temperature; it is said that the levels *thermalize*. The necessary density to reach thermalization is defined as that for which the rate of collisional downward transitions is equal to the rate of spontaneous transitions:

$$C_{ji} = A_{ji} \Rightarrow n = \frac{A_{ji}}{\gamma_{ji}} \equiv n_\mathrm{crit}. \tag{2.46}$$

On the other hand, if the density is low ($n \to 0$), the radiation from the background will dominate and we will have that

$$\frac{n_j}{n_i} = \frac{B_{ij}I_\nu}{B_{ji}I_\nu + A_{ji}} \Rightarrow \mathrm{e}^{-h\nu_{ji}/kT_\mathrm{bg}}. \tag{2.47}$$

For the low density limit, the $T_\mathrm{ex} \to T_\mathrm{bg}$.

Consider the solution of the radiative transfer equation (2.18). Then, toward a line emitting source (ON source), the brightness is given by:

$$I_\nu^\mathrm{ON} = I_\nu(0)\ \mathrm{e}^{-\tau_\nu} + \mathcal{S}_\nu\ (1 - \mathrm{e}^{-\tau_\nu}). \tag{2.48}$$

This expression includes the emission of the line as well as the adjacent continuum. To subtract the continuum, observations toward a region off the source are required ($\tau_\nu = 0$); then, the intensity at the OFF position is:

$$I_\nu^{\rm OFF} = I_\nu(0) \tag{2.49}$$

The intensity of the line is expressed as follows:

$$I_\nu^{\rm L} = I_\nu^{\rm ON} - I_\nu^{\rm OFF} = [\mathcal{S}_\nu - I_\nu(0)]\ (1 - {\rm e}^{-\tau_\nu}). \tag{2.50}$$

Since $\mathcal{S}_\nu = B_\nu(T_{\rm ex})$ (see Estallela & Anglada 1999, pp. 15), using the definition in equation 2.2, and defining the intensity in units of temperature, $J_\nu(T)$, as following:

$$B_\nu(T) = \frac{2k\nu^2}{c^2} J_\nu(T); \tag{2.51}$$

we can write equation 2.50 as:

$$T_L = J_\nu(T_{\rm L}) = [J_\nu(T_{\rm ex}) - J_\nu(T_{\rm bg})]\ (1 - {\rm e}^{-\tau_\nu}). \tag{2.52}$$

Obtaining physical parameters from molecular observations

To obtain the excitation temperature, we can observe a molecule whose optical depth at the center of the line, τ_0, is much larger than 1, such that equation 2.52 becomes:

$$T_L^0 = J_\nu(T_{\rm ex}) - J_\nu(T_{\rm bg}), \tag{2.53}$$

where T_L^0 is the intensity of the line at its center. Now we can solve for $T_{\rm ex}$ and obtain:

$$T_{\rm ex} = \frac{h\nu/k}{\ln\left[1 + \frac{h\nu/k}{T_{\rm L}^0 + J_\nu(T_{\rm bg})}\right]}. \tag{2.54}$$

If the transitions are thermalized then $T_{\rm ex} \rightarrow T_{\rm k}$, and we obtain the kinetic temperature of the gas.

On the other hand, if the optical depth of the line is much lower than 1, then we have that equation 2.52 can be written as:

$$T_L^0 = [J_\nu(T_{\rm ex}) - J_\nu(T_{\rm bg})]\tau_0. \tag{2.55}$$

Therefore, to derive the excitation temperature, we need to use two transitions. For example, if we have observations of the transitions CO (J=2→1) and CO (J=1→0), for which $\tau_0 \ll 1$, neglecting the correction for departures from the Rayleigh-Jeans regime, and assuming thermalization, we can write the ratio of the line temperatures as:

$$\frac{T^0_{L,21}}{T^0_{L,10}} = \frac{\tau_{0,21}}{\tau_{0,10}}. \tag{2.56}$$

It can be shown that τ_0 can be expressed in terms of the total column density (N) of CO, as follows (Estallela & Anglada 1999, pp. 87):

$$\tau_0 = \frac{(2J+1)hc^3 A_{J,J-1}}{16\pi J k \nu^2_{J,J-1} \Delta v T_{\rm ex}} N \left(\mathrm{e}^{h\nu_{J,J-1}/kT_{\rm ex}} - 1\right) \mathrm{e}^{-(J+1)h\nu_{J,J-1}/2kT_{\rm ex}}, \tag{2.57}$$

where J is the number of the rotational level and Δv is the width of the line at half maximum. Using this last expression for the optical depths in equation 2.53, we obtain the excitation, and kinetic temperatures (assuming thermalization of the transitions) are given by:

$$T_{\rm ex,k} = -\frac{11.06}{\ln(R/4)}, \tag{2.58}$$

where R is the ratio between the velocity integrated intensities:

$$R = \frac{T^0_{L,21}\Delta v_{21}}{T^0_{L,10}\Delta v_{10}}.$$

Equation 2.57 can also be used to solve for the total column density, which results as:

$$N = \frac{16\pi J k \nu^2_{J,J-1}}{(2J+1)hc^3 A_{J,J-1}} (T_{\rm ex}\tau_0 \Delta v) \left(\mathrm{e}^{h\nu_{J,J-1}/kT_{\rm ex}} - 1\right)^{-1} \mathrm{e}^{(J+1)h\nu_{J,J-1}/2kT_{\rm ex}}. \tag{2.59}$$

The second factor in the right side of the equation can be obtained observationally; for $T_{\rm ex} \gg T_{\rm bg}$, in the Rayleigh-Jeans regime, equation 2.55 can be written as:

$$T^0_L \Delta v = T_{\rm ex}\tau_0 \Delta v,$$

which is the velocity integrated line intensity.

2.2.2 Maser line emission

The word *maser* stands for "Microwave Amplification by Stimulated Emission of Radiation", which is a phenomenon equivalent to the laser, but at radio wavelengths. Maser emission is produced when there is an inversion of the populations of the energy levels such that

$$\frac{n_j}{n_i} = \frac{g_j}{g_i} \mathrm{e}^{-h\nu_{ji}/kT_{\mathrm{ex}}} > 1, \tag{2.60}$$

implying that $T_{\mathrm{ex}} < 0$. This negative value of the temperature only indicates that the population of the upper energy level is larger; it has nothing to do with the thermodynamic temperature of the gas. We see from equation 2.26 that this condition also implies that the absorption coefficient $\kappa < 0 \Rightarrow \tau_0 < 0$. Then, from equation 2.52, we have that:

$$T_L = |T_{\mathrm{ex}}| \mathrm{e}^{|\tau_\nu|}, \tag{2.61}$$

which means that the intensity is amplified exponentially as radiation passes through the region.

If we consider only two levels, as we have done so far, we realized that the inversion of population of the energy levels cannot be possible, since in that case: $T_{\mathrm{bg}} < T_{\mathrm{ex}} < T_{\mathrm{k}}$ (see §2.2.1). Therefore, it is not possible to obtain a negative excitation temperature. It is necessary to consider transitions from and to other energy levels. The transitions from these other levels, which populate a given level i or j, are called *pumping* transitions, and they are responsible for the inversion of the population. We can consider all the other transitions as if they were a *third* level k (see Figure 2.7). Then, we call P_j the effective rate of transitions from level k to j, and similarly, P_i is the effective rate of transitions from level k to i passing through the level k. If we have that $P_j > P_i$, then there will be a net increase in the population of the level j and the inversion of population will be achieved.

As the radiation passes through a region in which the populations are inverted, the particles in the energy level E_j are stimulated to undergo a transition to the level E_i; the upper level tends to be depopulated. On the other hand, the pumping mechanism tends to maintain the inversion of population. If the radiation field is strong enough to change considerable the population of the energy levels, the maser is referred as to be *saturated*, otherwise it is called *unsaturated* maser. Under unsaturated conditions, the

intensity of the masers increases exponentially, while for the saturated maser, the intensity increases linearly.

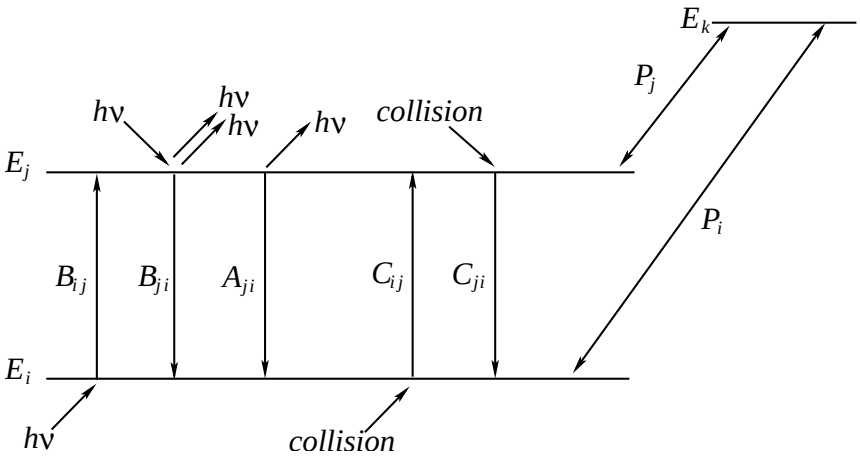

Figure 2.7: Energy levels involved in maser emission. E_i and E_j are the masing levels, while E_k represents all other energy levels from which the masing levels can be populates. P_i and P_j represent the effective pumping rates of the masing levels.

Pumping mechanisms

The excitation of the particles to higher energy levels can be achieved either by collisions with other particles or by absorption of radiation (see §2.2). The pumping mechanism is called collisional or radiative according to the nature of the process that dominates the excitations. Due to their complexity, the pumping models are almost always evaluated with the aid of detailed numerical calculations; they include a series of transition cycles in which the particles are excited from the ground state to higher energy levels, then they decay in cascade until finally they reach the masing level j, which should be overpopulated in order to produce the maser emission. The conditions in most strong astronomical masers are such that many transitions which connect the maser levels with other states are optically thick. These include, many times, the loss of transitions of the pumping cycle. This has a significant effect on the basic pumping considerations, since it establishes a coupling between the distribution of any given pair of levels and the intensity of the radiation in the line which connects them, slowing down their effective

transition rates. Because of this coupling, which occurs through the effects of absorption and stimulated emission, a complete treatment of the problem requires a simultaneous solution of the equations of populations for all the relevant levels and the transfer of radiation in all the lines which couples them. A practical treatment of the problem therefore requires some approximation method to decouple the equations of level populations and radiative transfer. The most popular of such method is the formalism of escape probability, first introduced by Sobolev (1958). A detailed presentation of the assumptions and derivation of the equations of this analysis can be found in works such as Elitzur (1982). Following we will discuss some of the conclusions derived from the pumping models that make use of the Sobolev approximation.

Radiative pumps

For the pump dominated by radiative processes, the excitations through collisions are neglected. In order to achieve the inversion of populations, it is required that the pumping radiation is produced by an external source (a diluted blackbody), or by dust particles, at a temperature T_d, which are mixed with the source molecules.

In general, we can write the number of photons emitted from a radiatively pumped maser source as

$$N_m = \eta P_t, \tag{2.62}$$

where $\eta = (P_j - P_i)/(P_j + P_i)$, is the pumping efficiency of the maser, and P_t is the total pump rate in the source. It can be shown that regardless of the optical depth of the maser source, the pump rate at a radiatively pumped maser is equal to the number of pump photons absorbed by it per unit of time, N_p, i.e.:

$$P_t = N_p, \tag{2.63}$$

which, when combined with equation 2.62 yields:

$$N_m = \eta N_p, \tag{2.64}$$

therefore, the number of maser photons emitted cannot exceed the number of pump photons absorbed. This provides a very powerful constraint on any potential radiative pump model. If a certain pump is advocated for a given maser source, the number of photons emitted by the pump source in the proposed pump lines must exceed the number of maser photons, which is directly determined from observations. This constraint indicates that one can

probably rule out ultraviolet or optical pumps since the required luminosities of the pumping sources are often not available.

Collisional pumps

When the excitations from the ground state are dominated by collisions, the pump is referred to as collisional. The pump rate due to collisions can be written as:

$$P = C_p n_k, \tag{2.65}$$

where C_p is the average rate for collisional excitation from the reservoir to the maser levels. The total maser photon emission rate is then

$$N_m = \eta C_p n_k \Delta V, \tag{2.66}$$

where ΔV is the volume of the maser source. This relation does not constrain the pump in any obvious manner similar to equation 2.64 for a radiative pump. However, collisional pumps are constrained because collision rates which are too high would thermalize the level population and quench the maser altogether. The modeling of collisional pumps is often hampered by poor knowledge of detailed state-to-state cross section, which is one of the more serious problems of molecular astrophysics in general.

Detection of magnetic fields through maser observations

The detection and measurement of magnetic fields in cosmic sources represents a great challenge for the observational astronomers. In most of the cases, they are inferred through polarization observations of dust or line emission. It is worth to note that the measured polarization can be due to different mechanisms but it is mainly attributed to the presence of a magnetic field. In the case of the dust emission, assuming that the dust grains are aligned due to the magnetic field, the degree and direction of the linear polarization i indicates the strength and direction of the field. This method has been used mainly for determining the presence of magnetic fields in star forming regions. On the other hand, in the envelopes of evolved stars, maser emission has been used to study the magnetic fields. Due to their intrinsic high brightness and narrow linewidth, masers are a very useful tool to determine the presence, strength and direction of magnetic fields in cosmic sources

The OH molecule is a radical with a net electronic angular momentum

L and electron spin **S**, which give rise to the magnetic moments $\boldsymbol{\mu}_L = \mu_{\rm B}\mathbf{L}$ and $\boldsymbol{\mu}_S = 2.00229\mu_{\rm B}\mathbf{L}$, respectively. $\mu_{\rm B}$ is know as the Bohr magneton, and its value is expressed by the following expression:

$$\mu_{\rm B} = \frac{e\hbar}{2m_e c}. \tag{2.67}$$

Consequently, the molecule can interact with an external magnetic field **B** changing its energy by

$$\Delta E = \boldsymbol{\mu}_L \cdot \mathbf{B} + \boldsymbol{\mu}_S \cdot \mathbf{B}. \tag{2.68}$$

This causes the energy levels to split into different components; this phenomenon is known as the *Zeeman effect*. Observationally, if the magnetic field is not too strong, this effect leads to the unfolding of an emission line, with central frequency ν_0, into 3 components: two circularly polarized, split at frequencies $\nu_0 \pm \delta\nu$, and one linearly polarized centered at frequency ν_0. From equation 2.70, it can be shown that the circularly polarized components are shifted in frequency from the central component by:

$$\delta\nu = \frac{g_J \alpha_J \mu_{\rm B}}{h} B, \tag{2.69}$$

where g_J is known as the Lande factor, and its value its of the order of unity; α_J is a factor that arises due to the hyperfine structure (see Townes & Schawlow 1975). Therefore, by measuring the separation of the split components, it is possible to determine the strength of the magnetic field.

In order to measure the magnetic fields in astronomical sources, astronomers can use telescopes equipped with two feeds circularly polarized: right circular polarization and left circular polarization (RCP, and LCP, respectively). The response of the feeds to the polarized radiation would be given by

$$\begin{aligned} I_{\rm RCP,LCP}(\nu) =& \frac{1}{4}\left[(\cos\theta \pm 1)^2 I_0(\nu + \delta\nu)\right. \\ & \left. +(\cos\theta \mp 1)^2 I_0(\nu - \delta\nu) + 2\sin^2\theta\ I_0(\nu)\right], \end{aligned} \tag{2.70}$$

where θ is the angle between the direction of the magnetic field and the line of sight; $I_0(\nu)$ is the total intensity (in the absence of magnetic field); and the upper and lower sings should be used for the RCP and LCP, respectively.

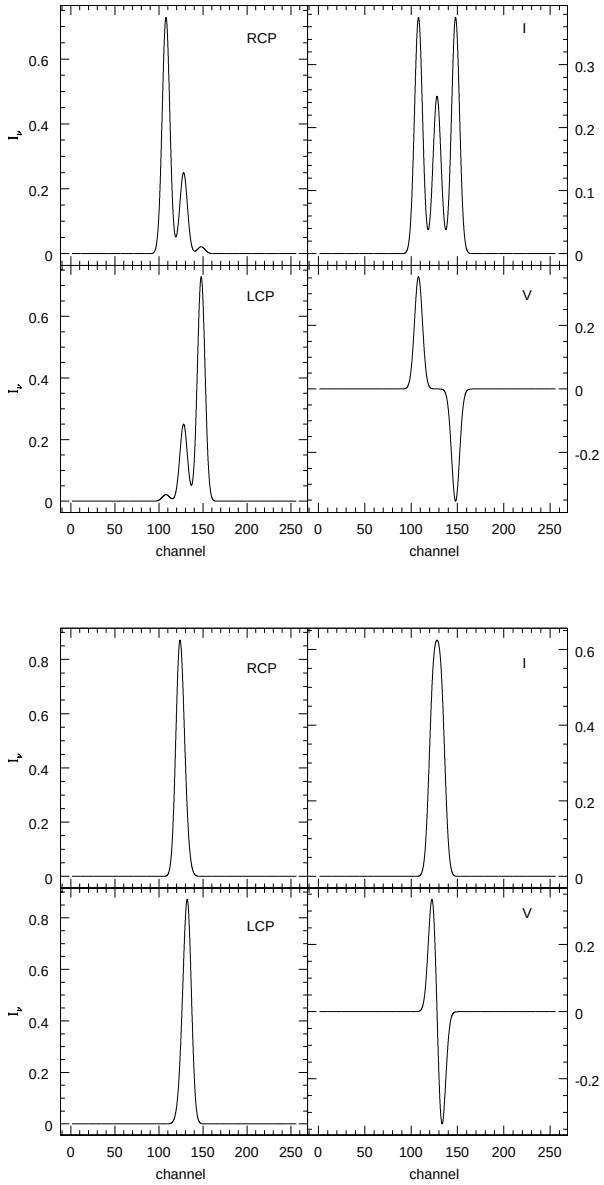

Figure 2.8: Top: Large splitting case of the Zeeman effect of a Gaussian line; the three polarized components are clearly separated. Bottom: Small splitting case of the Zeeman effect. In this case the polarized components are blend together.

We note that the emission from the three polarized components are detected in each feed, although it might not always be the case that they are clearly separated.

For the situation in which they are clearly separated (large splitting; see upper panel of Figure 2.8), both the strength of the magnetic field and its angle with respect to the line of sight, θ, can be obtained from the observations (Sault et al. 1990). This can be done by firstly inverting equation 2.69, from where we can obtain B; for example, in the particular case of the transition of the OH at 1665 MHz, the Lande factor $g_J = 2.34$, and $\alpha_J = 1.4$, which gives us $B \simeq 0.3\,\delta\nu\ \mu\mathrm{G\ Hz^{-1}}$.

To find θ, we consider the ratio of the components of the two feeds for which $\delta\nu$ is positive (first term in the right hand side of equation 2.70):

$$\gamma = \frac{I_{\mathrm{RCP}}(\nu)}{I_{\mathrm{LCP}}(\nu)} \simeq \frac{(\cos\theta + 1)^2}{(\cos\theta - 1)^2}, \tag{2.71}$$

from where we can solve for θ:

$$\cos\theta = \frac{-1(1+\gamma) \pm 2(\gamma)^{1/2}}{1-\gamma}. \tag{2.72}$$

However, in most astronomical observations, it is not possible to separate clearly the three Zeeman components; they appear blend together in just one line in each of the feeds (small splitting; see lower panel of Figure 2.8). In this case it is not possible to measure directly neither B nor $\cos\theta$, and an indirect method has to be used. A detailed treatment on the derivation of parameters from the small splitting case can be found in works such those from Schwarz et al. (1986) or Sault et al. (1990); here, we will just present a basic derivation.

From the definition of the parameter stokes V:

$$\mathrm{V} = \frac{I_{\mathrm{RCP}} - I_{\mathrm{LCP}}}{2}, \tag{2.73}$$

using equations 2.70 and 2.69, we see that

$$\begin{aligned} \mathrm{V}(\nu) = &\quad \tfrac{1}{2}\cos\theta\,[I_0(\nu+\delta\nu) - I_0(\nu-\delta\nu)] \\ = &\quad \frac{I_0(\nu+\delta\nu) - I_0(\nu-\delta\nu)}{2\delta\nu}\cos\theta\ \delta\nu \simeq \quad \frac{dI(\nu)}{d\nu}\,\frac{g_{\mathrm{J}}\alpha_J\mu_{\mathrm{B}}}{h} B\cos\theta \end{aligned}$$

$$\Rightarrow \mathrm{V} = bB\cos\theta\frac{dI(\nu)}{d\nu}, \tag{2.74}$$

where $b = \frac{g_{\mathrm{J}}\alpha_J\mu_{\mathrm{B}}}{h}$ is the Zeeman factor. A good approach to find $bB\cos\theta$ is done by dividing the spectrum of the stokes parameter V, by the derivative of stokes parameter I, then the magnetic field can be derived (see e.g. Schwarz et al. 1986, Sault et al. 1990).

We will never know how to study by any means the chemical composition (of stars), or their mineralogical structure.

Augusto Comte

3

Detection of HCO^+ Emission toward the Planetary Nebula K 3-35*

D. Tafoya, Y. Gómez, G. Anglada, L. Loinard, J. M.Torrelles, L. F. Miranda, M. Osorio, R. Franco-Hernández, L-Å, Nyman, J. Nakashima and S. Deguchi

3.1 Abstract

We report the detection, for the first time, of HCO^+ ($J = 1 \rightarrow 0$) emission as well as marginal CO ($J = 1 \rightarrow 0$) emission toward the planetary nebula (PN) K 3-35 as a result of a molecular survey carried out toward this source. We also report new observations of the previously detected CO ($J = 2 \rightarrow 1$) and water maser emission, as well as upper limits for the emission of the SiO, $H^{13}CO^+$, HNC, HCN, HC_3OH, HC_5N, CS, HC_3N, ^{13}CO, CN, and NH_3 molecules. From the ratio of CO ($J = 2 \rightarrow 1$) to CO ($J = 1 \rightarrow 0$) emission we have estimated the kinetic temperature of the molecular gas, obtaining a value of $\simeq 20$ K. Using this result, we have estimated a molecular mass for the envelope of $\simeq 0.017\ M_\odot$, and an HCO^+ abundance relative to H_2 of 6×10^{-7}, similar to the abundances found in other PNe. K 3-35 is remarkable because it is one of the two PNe reported to exhibit water maser emission, which is present in the central region as well as at a distance of $\simeq 5000$ AU away from the center. The presence of molecular emission provides some clues that could help to understand the persistence of water molecules in the envelope of K 3-35. The HCO^+ emission could be arising in dense molecular clumps, that may provide the shielding mechanism which protects water molecules in this source.

*Published in the Astronomical Journal, 2007, Volume 133, Issue 2, pp. 364-369.

3.2 Introduction

The chemical composition of the molecular envelope that surrounds a young planetary nebula (PN) can reflect the recent history of the transition from the asymptotic giant branch (AGB) to the PN phase. When envelopes of AGB stars are oxygen-rich, they may produce strong maser emission of one or more molecules such as OH, H_2O, or SiO, which commonly appears stratified, with the SiO masers located close to the stellar surface, water masers in the range of about 10-100 AU, and OH masers farther away, up to 10^4 AU from the central star (Reid & Moran, 1981; Chapman & Cohen, 1986).

Molecules that were present in the red giant envelope are destroyed by the radiation of the core as the star evolves to the PN phase, while other molecular species could develop in these peculiar physical conditions. In particular, water-vapor masers that are detected in the giant envelopes (Reid & Moran, 1981; Elitzur, 1992a; Habing, 1996), and also in some pPNe (Likkel & Morris, 1988; Marvel & Boboltz, 1999; Gómez & Rodríguez, 2001; Imai et al., 2002), are not expected to persist in the PN phase, where the envelope not only begins to be ionized but also becomes rarefied (Lewis 1989; Gómez, Moran & Rodríguez 1990). As the slow and massive mass loss of the late AGB-phase stops and the star enters in its PN phase, the water molecules are expected to disappear in a time scale of decades (Gómez et al., 1990), and only OH masers seem to persist for a considerable time ($\simeq$ 1000 yr; Kwok 1993). However, recently two PNe (K 3-35 and IRAS 17347-3139; Miranda et al. 2001, de Gregorio-Monsalvo et al. 2004) have been found to harbor water maser emission, suggesting that these objects are in an early stage of their evolution as PNe, where the physical and chemical conditions could still permit the existence of water molecules.

K 3-35 is a very young PN (which evolved from an oxygen rich AGB star) characterized by an S-shaped radio continuum emission morphology with a well defined point-symmetric structure (Aaquist & Kwok 1989; Aaquist 1993; Miranda et al. 2000, 2001). The detected water-vapor masers are located at the center of the nebula, apparently tracing a torus-like structure with a radius of $\simeq$ 85 AU (adopting a distance of $\simeq$ 5 kpc, Zhang 1995), and in addition they are also found at the surprisingly large distance of 5000 AU from the star, in the tips of the bipolar lobes (Miranda et al., 2001; Gómez et al., 2003). Water masers were not expected to be found at such an enormous distance in an evolved star since the physical conditions required to pump the

maser emission ($n_{\rm H_2} \simeq 10^8$ cm^{-3}, $T_{\rm k} \simeq 500$ K) are difficult to explain, given our current understanding of these objects. Miranda et al. (2001) proposed that shocks driven by the bipolar jet could create the physical conditions necessary to pump the distant water-vapor masers. However, the presence and persistence of water molecules in these PNe are still puzzling, probably being related to some shielding mechanism due to the presence of high density molecular gas that protects water molecules against the ionizing radiation of the central star.

To investigate the possible existence of such a shielding mechanism, one must characterize the physical conditions of the molecular gas in the envelope surrounding K 3-35. Interestingly, weak broad CO ($J = 2 \rightarrow 1$) emission has been detected toward K 3-35 by Dayal & Bieging (1996), and more recently by Huggins et al. (2005), indicating the presence of a neutral molecular envelope and suggesting the possible presence of dense molecular clumps. In this paper, we present a search for additional molecular emission toward K 3-35, reporting the first detection of HCO^+ in this PN, confirmation of CO ($J = 2 \rightarrow 1$) and water maser emission, as well as a tentative detection of CO ($J = 1 \rightarrow 0$).

3.3 Observations

The survey for molecular lines toward the young planetary nebula K 3-35 was carried out using the Onsala 20 m telescope in Sweden, the 45 m Nobeyama telescope in Japan and the IRAM 30 m telescope in Spain (see Table 3.1). The coordinates RA(J2000)=$19^h27^m44^s$, Dec(J2000)=$21°30'03''$ were adopted for the position of K 3-35 (Miranda et al., 2001). In what follows, we describe each of these observations.

3.3.1 20 m Onsala

Observations of several molecular transitions from 86 to 113 GHz were carried out using the 20 m telescope of the Onsala Space Observatory (OSO)[8] in the dual beam switching mode. We used a 100 GHz receiver which includes a cryogenically cooled SIS-mixer covering the frequency range from 84 to 116 GHz. The backend used was the LCOR autocorrelator which, for all

[8]Onsala Space Observatory at Chalmers University of Technology is the Swedish National Facility for Radio Astronomy

molecular transitions except for ^{13}CO, had a bandwidth of 80 MHz, providing a resolution of 50 kHz. This corresponds to a velocity resolution of $\simeq 0.17$ km s^{-1} at 86 GHz and $\simeq 0.13$ km s^{-1} at 115 GHz. The ^{13}CO observations were carried out with a bandwidth of 40 MHz, providing a spectral resolution of 25 kHz, which corresponds to a velocity resolution of $\simeq 0.068$ km s^{-1}. In all cases the bandwith was centered at $v_{\rm LSR} = 20$ km s^{-1}. The half power beam width (HPBW) of the telescope ranges from $\simeq 44''$ at 86 GHz to $33''$ at 115 GHz. System temperatures were typically in the range from 300 to 500 K. The parameters of the molecular transitions observed as well as additional telescope parameters are given in Table 3.1.

3.3.2 45 m Nobeyama

Observations with the 45 m radio telescope at Nobeyama[9] were carried out using the position switching mode. The BEam Array Receiver System (BEARS), consisting of a grid of 5×5 beams separated by $\sim 41''$, was used for the observations of the CO ($J = 1 \rightarrow 0$) transition at 115 GHz. The backend bandwidth was 32 MHz, and was centered at $v_{\rm LSR} = 20$ km s^{-1}, providing a spectral resolution of 30 kHz ($\simeq 0.08$ km s^{-1}). The HPBW of the telescope at this frequency is $\simeq 16''$. Typical system temperatures for the 115 GHz observations were in the 420-450 K range.

Observations of the H_2O maser and NH_3(1,1) lines at $\nu \simeq$ 22-24 GHz were carried out using the H22 receiver. We used a bandwidth of 40 MHz centered at $v_{\rm LSR} = 20$ km s^{-1} with a frequency resolution of 20 kHz ($\simeq 0.25$ km s^{-1}). The HPBW of the telescope at these frequencies is $\sim 70''$. Typical system temperatures for these observations were 200-300 K. The parameters of the molecular transitions observed as well as additional telescope parameters are given in Table 3.1.

3.3.3 30 m IRAM

Observations of the CO ($J = 2 \rightarrow 1$) line at 230 GHz were carried out with the IRAM 30 m telescope at Pico Veleta using the position switching mode. We used the multibeam HEterodyne Receiver Array (HERA), which consists of nine receivers arranged in a regular 3×3 grid with spacing on the

[9]The Nobeyama Radio Observatory is a branch of National Astronomical Observatory, an interuniversity research institute, operated by Ministry of Education, Science, and Culture, Japan

Table 3.1. Single Dish Observations toward K 3-35

Telescope	Date	Molecule	Transition	Frequency (GHz)	$\eta_{\rm MB}$[a]	Γ[b] (K Jy^{-1})	Δch[c] (km s^{-1})	rms ($T_{\rm MB}$)[d] (K)	$\int T_{\rm MB} {\rm d}v$[e] (K km s^{-1})	$v_{\rm LSR}$[f] (km s^{-1})	Δv[g] (km s^{-1})
20m OSO	Feb-Mar 2003	SiO	$v = 1,\ J = 2 \rightarrow 1$	86.2434420	0.65	0.045	0.174	0.024	...	...	...
"	"	$H^{13}CO^+$	$J = 1 \rightarrow 0$	86.7542940	0.64	0.045	0.173	0.024	...	...	...
"	"	HCN	$J = 1 \rightarrow 0,\ F = 2 \rightarrow 1$	88.6318473	0.63	0.043	0.169	0.017	...	...	...
"	"	HCO^+	$J = 1 \rightarrow 0$	89.1885180	0.63	0.043	0.168	0.012	0.33±0.03	28	20
"	"	HNC	$J = 1 \rightarrow 0,\ F = 2 \rightarrow 1$	90.6635430	0.61	0.043	0.165	0.024	...	...	...
"	"	CH_3OH	$J = 8_0 \rightarrow 7_1\, A^+$	95.1694400	0.58	0.040	0.158	0.028	...	...	...
"	"	HC_5N	$J = 36 \rightarrow 35$	95.8503370	0.58	0.040	0.156	0.030	...	...	...
"	"	CS	$J = 2 \rightarrow 1$	97.9809680	0.56	0.038	0.153	0.027	...	...	...
"	"	HC_3N	$J = 12 \rightarrow 11$	109.173634	0.47	0.034	0.137	0.039	...	...	...
"	"	^{13}CO	$J = 1 \rightarrow 0$	110.201353	0.47	0.033	0.068	0.045	...	...	...
"	"	CN	$J = 1 \rightarrow 0$	113.490982	0.44	0.032	0.132	0.044	...	...	...
45m Nobeyama	Mar 09, 2003	H_2O	$J = 6_{16} \rightarrow 5_{23}$	22.235080	0.81	0.357	0.250	0.010	1.5 ±0.1	21.4	0.72
							0.250	0.010	1.6±0.1	22.5	0.88
"	Mar 2003	NH_3	$(J, K) = (1, 1)$	23.695110	0.81	0.357	0.250	0.010	...	...	...
"	"	CO	$J = 1 \rightarrow 0$	115.271204	0.46	0.196	0.083	0.200	2.7±0.4	27	10
30m IRAM	Apr 01, 2003	CO	$J = 2 \rightarrow 1$	230.537990	0.58	0.105	0.406	0.088	10.2±0.4	23	20

[a]Main beam efficiency. The main beam brightness temperature is obtained as $T_{\rm MB} = T'_A/\eta_{\rm MB}$, where T'_A is the antenna temperature corrected for the atmospheric attenuation.

[b]Sensitivity of the telescope. The flux density can be obtained as $S_\nu = \eta_{\rm MB} T_{\rm MB}/\Gamma$.

[c]Channel width.

[d]1-σ rms noise per channel (in $T_{\rm MB}$ scale).

[e]Zero-order moment (velocity integrated intensity) of the line emission.

[f]First-order moment (intensity weighted mean $v_{\rm LSR}$) of the line emission.

[g]Equivalent line width, obtained from the second-order moment. For a Gaussian line profile, this value corresponds to the FWHM.

sky of 24″, and a beam size of $\sim 12''$. The backend used was the VErsatile Spectral and Polarimetric Array (VESPA) autocorrelator splitted into two parts, providing 438 channels of 0.41 km s^{-1} width, and 224 channels of 1.63 km s^{-1} width for each of the nine receivers. The system temperature was $\sim$ 300 K, and the pointing uncertainty was $\sim 2''$. The parameters of the molecular transition observed as well as additional telescope parameters are given in Table 3.1.

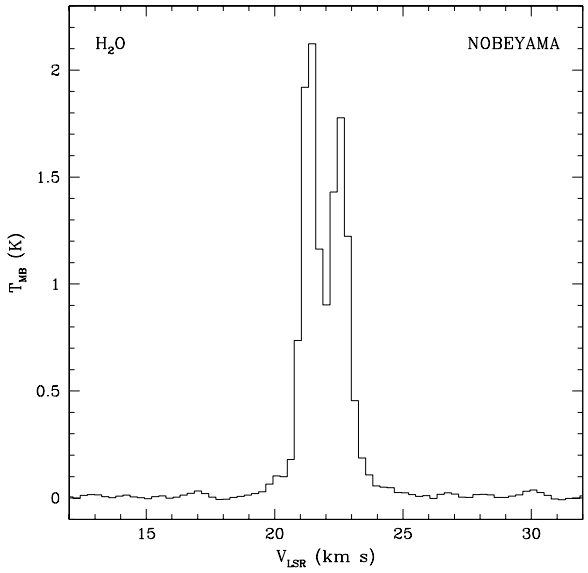

Figure 3.1: Water maser spectrum toward K 3-35 observed on March 9, 2003 with the Nobeyama 45 m telescope. The spectrum has been smoothed to a resolution of 0.25 km s^{-1} and a 1st order polynomial baseline has been subtracted. The rms noise in the off-line channels is 0.01 K. Two components at LSR velocities of 21.4 and 22.5 km s^{-1} can be identified.

3.4 Results

In Table 3.1 we summarize the results of our molecular survey toward K 3-35. We succeeded in detecting weak emission of HCO^+ ($J = 1 \rightarrow 1$) and CO ($J = 1 \rightarrow 0$), both reported for the first time in this work. We also detected CO ($J = 2 \rightarrow 1$) emission, which was reported previously by

Dayal & Bieging (1996) and Huggins et al. (2005), and water maser emission, reported previously by Engels et al. (1985), Miranda et al. (2001), and de Gregorio-Monsalvo et al. (2004). The remaining molecular transitions listed in Table 3.1 have not been detected. The integrated intensity, central velocity, and line width of the detected lines are presented in Table 3.1, where we also give the rms achieved in all the transitions observed in our survey.

3.4.1 H_2O

Using the 45 m Nobeyama telescope we detected the H_2O ($J = 6_{16} \rightarrow 5_{23}$) maser line toward K 3-35 (see Fig.3.1 and Table 3.1). The maser emission appears in the velocity range from 20 to 24 km s^{-1}, with two clear components centered at $v_{\rm LSR}$ = 21.4 and 22.5 km s^{-1}, similar to the velocities of the strongest peaks observed by Engels et al. (1985) and Miranda et al. (2001). The Very Large Array (VLA) observations of Miranda et al. (2001) reveal that this velocity range corresponds essentially to the features observed toward the center of K 3-35 and the tip of its northern lobe.

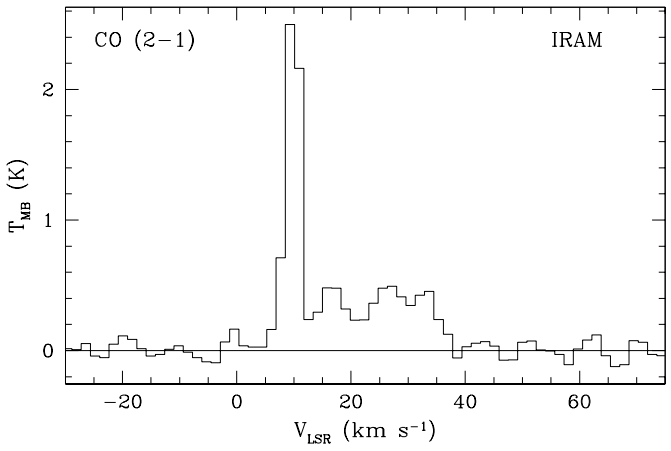

Figure 3.2: CO ($J = 2 \rightarrow 1$) spectrum toward K 3-35 observed with the IRAM 30 m telescope. The spectrum has been smoothed to a resolution of 1.6 km s^{-1} and a 2nd order polynomial baseline has been subtracted. The emission has two velocity components, a narrow component ($\Delta v \simeq 5$ km s^{-1}), centered at $v_{\rm LSR} \simeq 10$ km s^{-1}, and a broad component ($\Delta v \simeq 20$ km s^{-1}), centered at $v_{\rm LSR} \simeq 23$ km s^{-1}.

3.4.2 CO

Using the IRAM 30 m telescope we have detected CO ($J = 2 \rightarrow 1$) emission toward K 3-35. The observed emission has two velocity components, a narrow component ($\Delta v \simeq 5$ km s^{-1}), centered at $v_{\rm LSR} \simeq 10$ km s^{-1}, and a broad component ($\Delta v \simeq 20$ km s^{-1}), centered at $v_{\rm LSR} \simeq 23$ km s^{-1} (see Fig. 3.2). Our observations with the multibeam HERA array reveal that, while the emission of the narrow component is present over a large region ($\gg 1'$), the broad component is only detected toward the position of K 3-35. Given its line width and angular extension, we conclude that the narrow component is most probably of interstellar origin, while the broad component is most likely associated with the PN K 3-35. In order to better isolate the CO emission associated with K 3-35, a Gaussian fit to the narrow component was subtracted from the overall spectrum.

In Figure 3.2 we show the resulting CO ($J = 2 \rightarrow 1$) spectrum toward K 3-35, after subtraction of the narrow component. In Table 3.1 we give the line parameters of the broad component associated with K 3-35. The values of the central velocity and line width are similar to those reported previously by Dayal & Bieging (1996) using the Kitt Peak 12 m telescope and more recently by Huggins et al. (2005) using the Pico Veleta 30 m telescope. Our line intensity is higher than the value reported by Huggins et al. (2005), and this can be due to slight differences in the pointing, given the small size of the 30 m beam at 1.3 mm. Figure 3.4 shows a CO ($J = 2 \rightarrow 1$) spectra mosaic (after subtraction of the narrow component at 10 km s^{-1}) of a region of $1' \times 1'$, centered on K 3-35. This mosaic shows that broad emission is coming from within a region smaller than $\sim 20''$, providing a constraint on the angular size of the K 3-35 molecular envelope.

We also have detected weak broad CO ($J = 1 \rightarrow 0$) emission toward K 3-35 using the Nobeyama 45 m telescope (see lower panel of Fig. 3.3 and Table 3.1). An interstellar narrow CO ($J = 1 \rightarrow 0$) component was also present and subtracted as in the CO ($J = 2 \rightarrow 1$) data. The central velocity of the broad emission is $v_{\rm LSR} \simeq 27$ km s^{-1} and the line width is $\Delta v \simeq 10$ km s^{-1}. This is the first time that the CO ($J = 1 \rightarrow 0$) transition has been reported in association with this PN. Although the line is only marginally detected (3-σ) and more sensitive observations are necessary to confirm the detection, it is located at the right velocity, suggesting a true association with K 3-35. We attribute the apparent difference in line widths between the CO ($J = 2 \rightarrow 1$) and CO ($J = 1 \rightarrow 0$) lines to the modest signal-to-noise

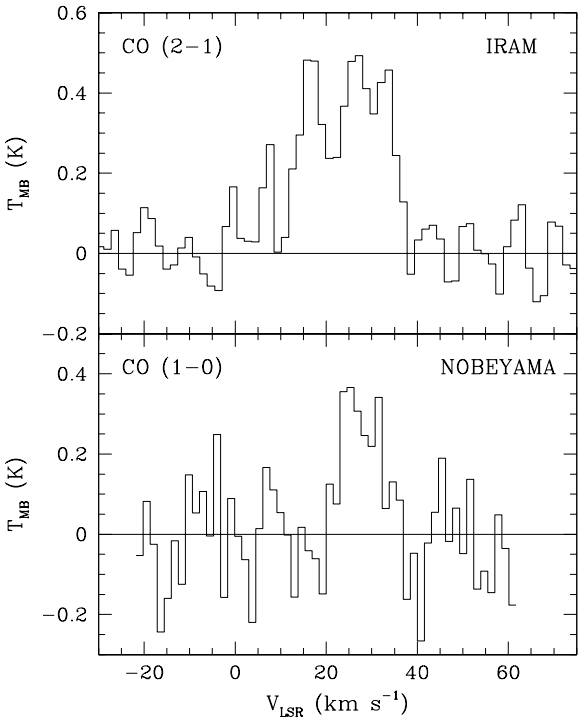

Figure 3.3: Upper panel: CO ($J = 2 \rightarrow 1$) spectrum toward K 3-35 observed with the IRAM 30 m telescope. The spectrum has been smoothed to a resolution of 1.6 km s^{-1} and a 2nd order polynomial baseline has been subtracted. The narrow, interstellar component at $v_{\rm LSR} \simeq$ 10 km s^{-1} (Fig. 2) has also been subtracted (see §3.2). The rms noise in the off-line channels is $\sim$ 0.063 K. The line emission is centered at $v_{\rm LSR} \simeq$ 23 km s^{-1}, with a line-width $\Delta v \simeq$ 20 km s^{-1}. Lower panel: CO ($J = 1 \rightarrow 0$) spectrum toward K 3-35 observed with the Nobeyama 45 m telescope. The spectrum has been smoothed to a resolution of 1.5 km s^{-1} and a 3rd order polynomial baseline has been subtracted. The narrow, interstellar component at $v_{\rm LSR} \simeq$ 10 km s^{-1} has also been subtracted. The rms noise in the off-line channels is $\sim$ 0.1 K. The line emission is centered at $v_{\rm LSR} \simeq$ 27 km s^{-1}, with a line-width Δv $\simeq$ 10 km s^{-1}.

ratio of the CO ($J = 1 \rightarrow 0$) detection.

The CO emission is very useful for investigating the physical parameters of the molecular gas associated with the PN K 3-35. An estimate of the kinetic temperature of the gas can be obtained from the ratio of the CO ($J = 2 \rightarrow 1$) to CO ($J = 1 \rightarrow 0$) transitions. Assuming that the level populations are well thermalized, that the emission is optically thin, and

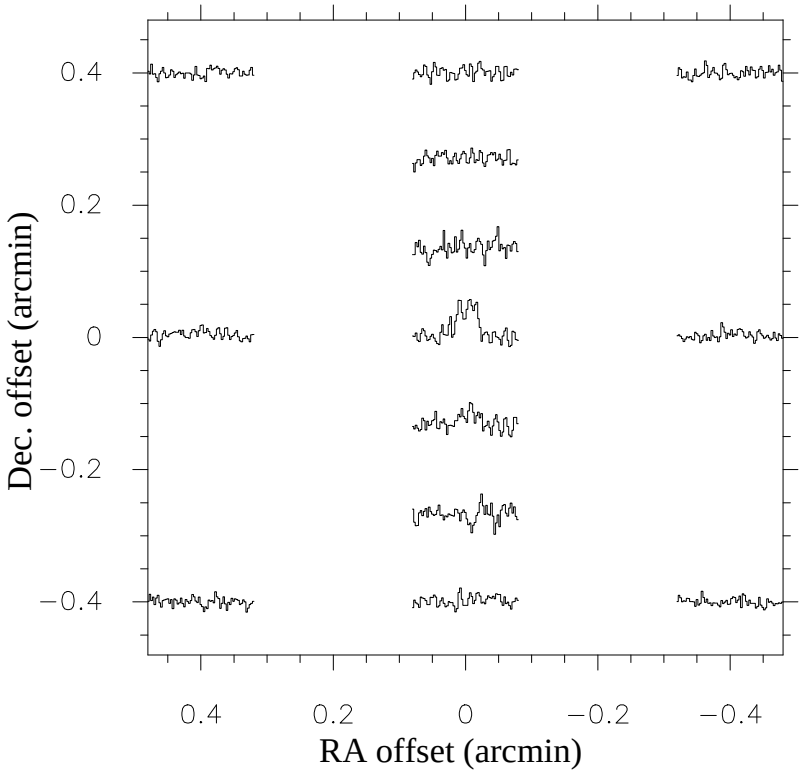

Figure 3.4: Mosaic of CO ($J = 2 \rightarrow 1$) spectra in the region around K 3-35 obtained with the IRAM 30 m telescope. A narrow, interstellar component at $v_{\rm LSR} \simeq 10$ km s^{-1}, present in all the positions, has been subtracted from the spectra. The (0,0) offset position corresponds to the position of K 3-35, RA(J2000)=$19^h27^m44^s$, Dec(J2000)=$21°30'03''$. Note that the emission arises from a compact region toward K 3-35.

neglecting the correction for departures from the Rayleigh-Jeans regime, the kinetic temperature can be approximated by the following equation,

$$T_k = -\frac{11.06}{\ln(R/4)}, \tag{3.1}$$

where R is the ratio of the CO ($J = 2 \rightarrow 1$) to CO ($J = 1 \rightarrow 0$) velocity integrated line intensities corrected by the difference in beam sizes. If the

emission is unresolved in both transitions,

$$R = (\theta_{2\rightarrow1}/\theta_{1\rightarrow0})^2 \int T_{\rm MB}({\rm CO}; 2\rightarrow1)\, dv / \int T_{\rm MB}({\rm CO}; 1\rightarrow0)\, dv,$$

being θ the FWHM of the telescope main beam. Using the integrated intensities of our 30 m and 45 m CO observations, we derived a value of 20 ± 6 K for the kinetic temperature of the molecular gas in K 3-35. Analysis of previous observations led to a higher kinetic temperature estimate ($T_k \geq 120$ K; Dayal & Bieging 1996). However, from our observations, and taking properly into account the difference in the telescope beam sizes, we derive for K 3-35 a lower value for the kinetic temperature, which is more similar to other kinetic temperature determinations in young PNe, ranging typically from 25 to 60 K (Bachiller et al. 1997).

The CO column density and molecular mass can be also derived from the CO observations assuming LTE conditions and that the emission is optically thin. For this, we use the CO ($J = 2 \rightarrow 1$) line since its spectrum is of better quality (see Fig. 3.3). The beam averaged CO column density can be obtained using the following relation,

$$\left[\frac{N({\rm CO})}{\rm cm^{-2}}\right] = \frac{1.1\times10^{13}\ T_k}{(e^{-5.54\,{\rm K}/T_k} - e^{-16.60\,{\rm K}/T_k})[(e^{11.06\,{\rm K}/T_k}-1)^{-1} - 0.02]} \times \left[\frac{\int T_{\rm MB}({\rm CO}; 2\rightarrow1)\ {\rm d}v}{\rm K\ km\ s^{-1}}\right]. \quad (3.2)$$

For a kinetic temperature $T_k = 20$ K, we obtain a beam averaged CO column density $N({\rm CO}) = 5.1 \times 10^{15}$ cm^{-2} for the K 3-35 envelope. The result is weakly dependent on the precise value of T_k adopted (for $T_k \simeq 100$ K, $N({\rm CO})$ would be only a factor of 2.6 higher).

The molecular mass of the envelope can be estimated using the following expression,

$$\left[\frac{M_m}{M_\odot}\right] = 2.9\times10^{-25} \left[\frac{\theta}{\rm arcsec}\right]^2 \left[\frac{D}{\rm kpc}\right]^2 \left[\frac{N({\rm CO})}{\rm cm^{-2}}\right] X_{\rm CO}^{-1}, \quad (3.3)$$

where θ is the FWHM of the telescope beam, D is the distance to the source, and $X_{\rm CO}$ is the abundance of CO relative to H_2. Using a representative value for PNe, $X_{\rm CO} \simeq 3\times10^{-4}$ (Huggins et al. 1996), and adopting a distance of $D = 5$ kpc to K 3-35, we estimate a molecular mass for the envelope of M_m

$\simeq 0.017\ M_\odot$. This result can be easily scaled for different values of T_k, D, and $X_{\rm CO}$ using the expressions given above.

3.4.3 HCO^+

HCO^+ ($J = 1 \rightarrow 0$) emission was detected toward K 3-35 with the 20 m Onsala telescope. This is the first time that HCO^+ emission has been reported in association with this PN. The observed spectrum is shown in Figure 3.5 and the line parameters are given in Table 3.1. The mean velocity of the HCO^+ emission is $v_{\rm LSR} \simeq 28$ km s^{-1} and the line width is $\Delta v \simeq 20$ km s^{-1}. These values are similar to those obtained from the CO ($J = 2 \rightarrow 1$) observations reported by Dayal & Bieging (1996), Huggins et al. (2005), and in the present work, supporting that the detected HCO^+ emission is associated with the planetary nebula K 3-35.

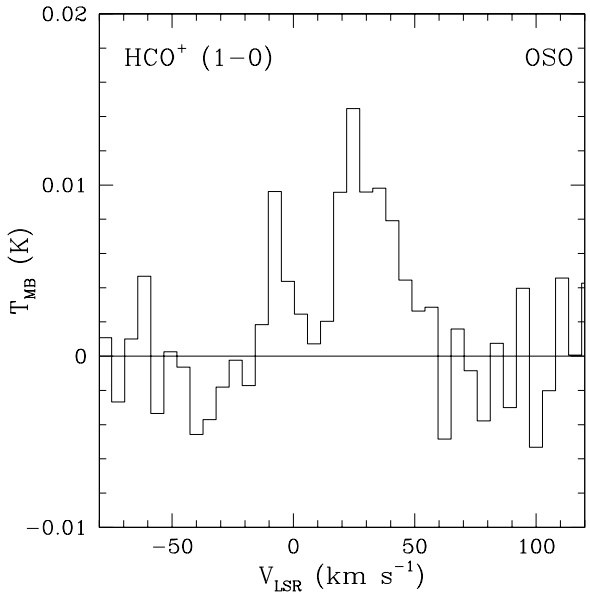

Figure 3.5: HCO^+ ($J = 1 \rightarrow 0$) spectrum toward K 3-35 observed with the Onsala 20 m telescope. The spectrum has been smoothed to a resolution of 5.4 km s^{-1} and a 2nd order polynomial baseline has been subtracted. The rms noise in the off-line channels is ~ 0.003 K. The line emission is centered at $v_{\rm LSR} \simeq 28$ km s^{-1}, with a line-width $\Delta v \simeq 20$ km s^{-1}.

Assuming LTE conditions and that the emission is optically thin, we can

estimate the beam averaged HCO^+ column density from our observations using the following equation,

$$\left[\frac{N(\mathrm{HCO^+})}{\mathrm{cm^{-2}}}\right] = \frac{7.9\times10^{10}\ \ T_k}{(1-e^{-4.29\,\mathrm{K}/T_k})[(e^{4.29.\,\mathrm{K}/T_k}-1)^{-1}-0.26]} \times\left[\frac{\int T_{\mathrm{MB}}(\mathrm{HCO^+};1\rightarrow0)\ \mathrm{d}v}{\mathrm{K\ km\ s^{-1}}}\right]. \quad (3.4)$$

For a kinetic temperature $T_k = 20$ K, the resulting beam averaged HCO^+ column density is $N(HCO^+) \simeq 6.9\times10^{11}$ cm^{-2}. This value implies for K 3-35 an HCO^+ abundance relative to CO, $[HCO^+/CO] = 1.9\times10^{-3}$, where we have corrected for the difference in the beam sizes, and an HCO^+ abundance relative to H_2, $X_{HCO^+} = 5.7\times10^{-7}$, assuming that $X_{CO} = 3\times10^{-4}$.

3.5 Discussion

The presence of water maser emission led to the suggestion that K 3-35 is an extremely young PN (Miranda et al. 2001), given that water molecules are expected to survive only for a short time ($\sim$ 100 yr) during the PN phase. However, the existence of these molecules in the envelope may not be an unambiguous indicator of youth, since dense molecular clumps could be protecting the water molecules from photo-dissociation and let them survive for a longer time. An alternative way to probe the evolutionary status of PNe is to analyze their molecular content. It is known that the molecular abundances in protoplanetary nebulae (PPNe) envelopes change as the core begins to produce UV radiation and the star enters in the PN phase. In particular, it has been observed that the HCO^+ abundance increases rapidly when the star goes from the PPN to PN phase (Bachiller et al. 1997; Josselin & Bachiller 2003), providing some indications on the evolutionary state. Furthermore, Huggins et al. (1996) found that the ratio of molecular to ionized mass, M_m/M_i, is inversely correlated with the radius of the nebula, and therefore it can be taken as an indicator of the evolutionary stage of the PN, almost independent of the distance.

In order to probe the evolutionary status of K 3-35 and compare it with other objects, we estimated the ratio M_m/M_i for K 3-35. The molecular mass for K 3-35 was obtained from our results in §3.2. To estimate the mass of ionized gas in K 3-35, we have followed the formulation of Mezger &

Henderson (1967) and used the 3.6 cm radio continuum data of Miranda et al. (2001). The value for the ionized mass is $M_i \simeq 9 \times 10^{-3}\ M_\odot$, resulting in a ratio of molecular to ionized mass, $M_m/M_i \simeq 1.9$ for K 3-35. This value for the ratio of molecular to ionized mass in K 3-35 is comparable to the values found for other young PNe (e.g. IC 5117) with kinematical ages of a few hundred years (Miranda et al. 1995). In order to further test the evolutionary status of K 3-35, we plot in Figure 3.6 the HCO^+ abundance as a function of the ratio of molecular to ionized mass for K 3-35, as well as for a sample of PPNe and PNe taken from Bachiller et al. (1997) and Josselin & Bachiller (2003). Figure 3.6 shows that the HCO^+ abundance in K 3-35 is ~ 500 times higher than the abundance in the PPN CRL 2688, and that it has reached a value comparable (in fact, somewhat higher) to those found in more evolved PNe.

The HCO^+ traces molecular gas with densities of order of $\sim 10^5$ cm^{-3}, such as that forming dense molecular clumps embedded in the ionized material (Huggins et al. 1992). It is feasible that these clumps could be protecting other molecules, such as H_2O, from the ionizing radiation. Therefore, the detection of HCO^+ in K 3-35 suggests that dense molecular clumps could be responsible for the shielding of the water molecules present in this nebula. Higher angular resolution observations at millimeter and submillimeter wavelengths would be very valuable to confirm the clumpiness in K 3-35.

In summary, our study of K 3-35 indicates that the molecular data on this PN are consistent with this source being a relatively young (a few hundred years) PN, where the survival of water molecules may be favored by the presence of dense molecular clumps that could be protecting the water molecules from photo-dissociation.

3.6 Conclusions

We have carried out a survey for molecular emission toward the young planetary nebula K 3-35. As a result of this survey, we detected for the first time HCO^+ ($J = 1 \rightarrow 0$) and CO ($J = 1 \rightarrow 0$) emission toward this PN. The emission appears in a velocity range that is in agreement with that of the broad CO ($J = 2 \rightarrow 1$) emission reported in previous studies, as well as in the present work. We have also mapped the CO ($J = 2 \rightarrow 1$) line, showing that the emission is compact and centered on K 3-35, confirming the association with the PN, and setting an upper limit for the angular size

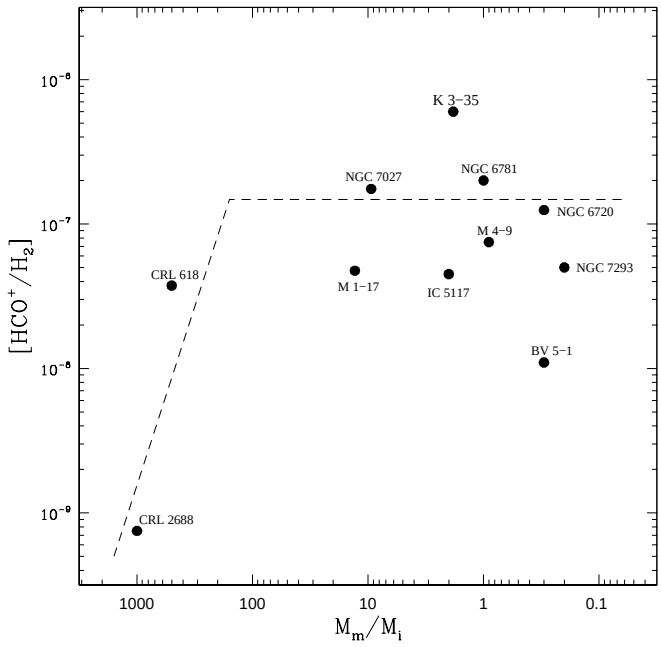

Figure 3.6: HCO^+ abundance as a function of the ratio between molecular and ionized mass, for several PPNe and PNe. The M_m/M_i ratio has been found to decrease with the age of the PN (Huggins et al. 1996). Therefore, the plot illustrates the time evolution of the HCO^+ abundance. The dashed line represents the average HCO^+ abundance for PPNe and PNe. Note the significant increase in the HCO^+ abundance from the PPN to the PN phase. Data points are taken from Bachiller et al. (1997) and Bachiller & Josselin (2003), except for K 3-35 (this work).

of the molecular envelope around K 3-35 of $\sim 20''$. We have used the ratio of the CO ($J = 2 \rightarrow 1$) and CO ($J = 1 \rightarrow 0$) lines to obtain a better constrained estimate of the kinetic temperature in the K 3-35 molecular envelope, which turns out to be $\sim 20\pm6$ K. From our observations we have found that the HCO^+ abundance in K 3-35 is $\sim 6 \times 10^{-7}$, which is similar to values found in other young PNe. This result, along with the value for the ratio of molecular to ionized mass, $M_m/M_i \simeq 1.9$, suggest that K 3-35 might not be an extremely young (< 100 yr) PN but a somewhat more evolved one (a few hundred years) where the presence of water maser emission could be favored by a shielding mechanism that prevents the water molecules from being dissociated. Since it is believed that the HCO^+ emission could be aris-

ing in dense clumps of molecular material embedded in the ionized gas, its detection in K 3-35, a source of water maser emission, provides an important clue to understand the shielding mechanism that could be protecting the water molecules from the radiation of the central star. Interferometric molecular observations at millimeter and submillimeter wavelenghts would be very valuable to determine the morphology of the molecular envelope and to investigate the clumpiness of the HCO^+ emission in this remarkable young planetary nebula.

When you make the finding yourself - even if you're the last person on Earth to see the light - you never forget it.

Carl Sagan

4

The magnetic field toward the young planetary nebula K 3-35*

Y. Gómez, D. Tafoya, G. Anglada, L. F. Miranda, J. M.Torrelles, N. A. Patel, R. Franco Hernández

4.1 Abstract

K 3-35 is a planetary nebula (PN) where H_2O maser emission has been detected, suggesting that it departed from the proto-PNe phase only some decades ago. Interferometric VLA observations of the OH 18 cm transitions in K 3-35 are presented. OH maser emission is detected in all four ground state lines (1612, 1665, 1667, and 1720 MHz). All the masers appear blueshifted with respect to the systemic velocity of the nebula and they have different spatial and kinematic distributions. The OH 1665 and 1720 MHz masers appear spatially coincident with the core of the nebula, while the OH 1612 and 1667 ones exhibit a more extended distribution. We suggest that the 1665 and 1720 masers arise from a region close to the central star, possibly in a torus, while the 1612 and 1667 lines originate mainly from the extended northern lobe of the outflow. A high degree of circular polarization (>50%) was found to be present in some features of the 1612, 1665, and 1720 MHz emission. For the 1665 MHz transition at $\sim$+18 km s^{-1} the emission with left and right circular polarizations (LCP and RCP) coincide spatially within a region of $\sim$0.″03 in diameter. Assuming that these RCP and LCP 1665 features come from a Zeeman pair, we estimate a magnetic field of

*Accepted for publication in the Astrophysical Journal.

$\sim$0.9 mG within 150 AU from the 1.3 cm continuum peak. This value is in agreement with a solar-type magnetic field associated with evolved stars.

4.2 Introduction

K 3-35 (PN G056.0+0.20; IRAS 19255+2123) is an extremely young PN where we are observing the first stages of formation of collimated bipolar outflows (Miranda et al., 1998). Its radio continuum emission at 3.6 cm exhibits an elongated, filamentary S-shape with a remarkable point-symmetric structure with respect to the center (Aaquist, 1993; Miranda et al., 2001; Gómez et al., 2003). Recently, its morphology has been successfully modeled with a precessing jet evolving in a dense asymptotic giant branch (AGB) circumstellar medium (Velázquez et al., 2007). The extension of the radio continuum jets at 3.6 cm is $\sim 2''$, which is equivalent to 10,000 AU (assuming a distance of 5 kpc; Zhang, 1995). A short dynamical age (<50 years) for the jets was estimated from Velázquez et al. (2007), which is comparable with that of the core. In addition, the high ratio of molecular to ionized mass (Tafoya et al., 2007) indicates that K 3-35 departed from the proto-PN phase only some decades ago.

K 3-35 was the first PN known to exhibit H_2O maser emission (Miranda et al., 2001). Since then, two other PNe have been reported with H_2O maser emission: IRAS 17347−3139 (de Gregorio-Monsalvo et al., 2004) and IRAS 18061−2505 (Gómez et al., 2008). The water masers toward K 3-35 are located at the center of the nebula, along the minor axis, at a radius of $\sim$85 AU and also at the tips of the jet lobes (Miranda et al., 2001). Uscanga et al. (2008) have analyzed the kinematics of the H_2O masers in K 3-35, identifying the presence of a rotating and expanding ring with a radius of $\sim$100 AU, which may be related with the collimation of the outflow.

The mechanism that generates collimated outflows in PNe and their role in the shaping of these objects is still a matter of debate. Magnetic fields have been suggested to play a major role in these aspects; their existence in circumstellar envelopes has been invoked to explain jets and bipolar morphologies in PNe (e.g. Rózyczka & Franco, 1996; **?**; García-Segura, 2006; Matt et al., 2000, 2004; Blackman et al., 2001; García-Segura et al., 2005; Frank et al., 2007). García-Segura & López (2000) have modeled morphologies of PNe with and without magnetic fields, showing the importance of magnetic fields to produce collimated ejections. Soker (2006) has argued that the magnetic

fields in PNe cannot shape the morphology of the nebula alone without the presence of a stellar companion that produces a spin-up mechanism in the envelope. The detection of magnetized disks toward evolved stars is therefore crucial to understand the generation of collimated jets and bipolar structures in PNe.

Magnetic fields have been detected in several proto-PNe (Zijlstra et al., 1989; Kemball & Diamond, 1997; Vlemmings, et al., 2005, 2006; Bains et al., 2003; Etoka & Diamond, 2004; Szymczak & Gérard, 2005; Herpin et al., 2006; Vlemmings & van Langevelde, 2008) but only toward a few PNe (Miranda et al., 2001; Greaves, 2002; Jordan et al., 2005). The strength of the magnetic fields detected in envelopes of evolved objects ranges from 1 G, at a radius of r$\sim$1 AU, to 10^{-4} G, at r$\sim$1000 AU, and is of the order of kG in the central stars of PNe (Jordan et al., 2005). Recently, the geometry of the magnetic field has been inferred for the proto-PN W43A (Vlemmings, et al., 2005) and the PNe NGC 7027, NGC 6537, and NGC 6302 (Greaves, 2002; Sabin et al., 2007) suggesting the presence of toroidal magnetic fields. In the particular case of K 3-35, it shows polarized OH maser emission in the 1665 MHz line around the central region, with a high level of circular polarization above $\simeq$50%, suggesting the presence of a magnetic field (Miranda et al., 2001; Gómez et al., 2005).

In this work we present VLA[1] observations toward K 3-35 of the OH maser emission in its four transitions (1612, 1665, 1667 and 1720 MHz) in order to study the spatial distribution and polarization of the masers as well as the magnetic field in this PN.

4.3 Observations

The OH maser observations towards K 3-35 at 1612.231, 1665.401, 1667.359 and 1720.530 MHz were carried out on 2002 March 31 with the VLA. The array was in the A configuration giving an angular resolution of $\sim$1″ at 18 cm. The 1665 and 1667 OH main lines were observed with a total bandwidth of 195.31 kHz, divided into 256 channels of 0.763 kHz each. The velocity resolution for these transitions was $\sim$0.14 km s^{-1} covering a total velocity range of 35 km s^{-1}. The 1612 and 1720 OH satellite lines were observed with

[1]The Very Large Array (VLA) is operated by the National Radio Astronomy Observatory (NRAO), facility of the National Science Foundation operated under cooperative agreement by Associated Universities, Inc.

Table 4.1. Calibrator Flux Densities

Frecuency	Flux Density (Jy)		
	Flux	Phase	Bandpass
(MHz)	1331+305[a]	1925+211[b]	0319+415[b]
1665	13.631	1.094±0.005	23.1±0.1
1667	13.623	1.087±0.005	23.4±0.1
1612	13.852	1.216±0.027	··· [c]
1720	13.412	1.069±0.007	23.4±0.3

[a]Adopted flux density.

[b]Boostrapped flux density for the phase and bandpass calibrators, respectively.

[c]The bandpass calibrator was not observed at 1612 MHz.

a total bandwidth of 781.25 kHz, divided into 256 channels of 3.05 kHz each, achieving a velocity resolution of ∼0.56 km s^{-1} yielding a total velocity range of ∼140 km s^{-1}.

The calibration, deconvolution, and imaging of the data were carried out using the Astronomical Image Processing System (AIPS) of the NRAO. Both the right circular polarization (RCP) and the left circular polarization (LCP) were observed simultaneously using the normal spectral line mode centered at a v_{LSR} = +15 km s^{-1} for all transitions, except the 1667 MHz line which was centered at +4 km s^{-1}. We applied Hanning smoothing to all four OH transitions in order to improve the signal-to-noise ratio of the data, and to minimize the Gibbs phenomenon. The resulting *rms* per channel is ∼ 6 mJy beam^{-1} for the 1665, 1667, and 1720 MHz transitions and ∼ 30 mJy beam^{-1} for the 1612 MHz transition. The absolute amplitude calibrator was 1331+305, the phase calibrator 1925+211, and the bandpass calibrator 0319+415. The flux densities of these calibrators for each frequency are summarized in Table **??**. The RCP and LCP data were calibrated separately and later combined during the imaging process to make Stokes I = (I_{RCP} + I_{LCP})/2 and Stokes V = (I_{RCP} − I_{LCP})/2 data sets, where I_{RCP} and I_{LCP} are the intensities in the right and left circular polarizations, respectively. Cleaned images for the RCP and LCP data were made using the task IMAGR of AIPS with the ROBUST parameter (Briggs, 1995) set to 0, allowing to determine the peak position of the OH masers, at each velocity channel, with a relative accuracy of ∼ 0.″05.

4.4 Results and Discussion

4.4.1 Continuum and OH Maser Emissions

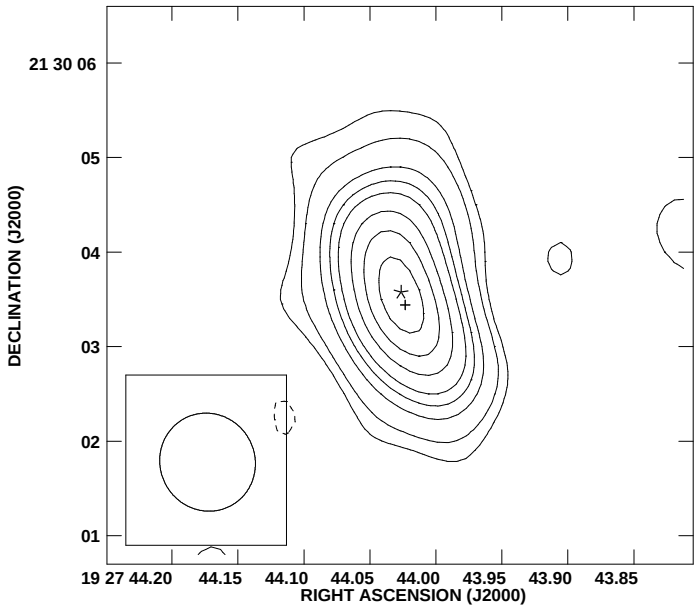

Figure 4.1: VLA 18 cm continuum contour image of K 3-35 (beam size is $\sim 1''$, shown in the bottom left corner of the image). The contours are -3, 3, 5, 7, 9, 12, 15, 20, and 30 times 0.3 mJy beam^{-1}, the rms noise of the image. The cross marks the continuum peak position at 1.3 cm at α(2000)= 19^h 27^m $44\overset{s}{.}0233$, δ(2000)= 21° $30'$ $03\overset{''}{.}441$, (Miranda et al., 2001; Uscanga et al., 2008). The star marks the peak position of the 18 cm continuum at α(2000)= 19^h 27^m $44\overset{s}{.}026$, δ(2000)= 21° $30'$ $03\overset{''}{.}57$ (this work). Note the NE-SW elongation of the emission that follows the same orientation as the bipolar outflow reported at higher frequencies (Miranda et al., 2001).

Figure 1 shows the 18 cm continuum emission toward K 3-35, taken from the line-free channels of the OH spectral data. The continuum emission has a deconvolved angular size of $1\overset{''}{.}8 \times 0\overset{''}{.}5$, P.A.= 16°. This 18-cm continuum image shows a northeast-southwest elongation which resemble the orientation of the bipolar outflow (Aaquist, 1993; Miranda et al., 2001). The total continuum flux density at 18 cm is 18 ± 1 mJy with a peak position at α(2000)= 19^h 27^m $44\overset{s}{.}026 \pm 0\overset{s}{.}001$, δ(2000)= 21° $30'$ $03\overset{''}{.}57 \pm 0\overset{''}{.}04$.

The 18 cm nominal peak position is located toward the north, about $\sim$0.″13, of the 1.3 cm peak position reported by Miranda et al. (2001). We attribute this shift in position to the fact that the 18 cm emission might be optically thick, while the 1.3 cm is optically thin, then the 1.3 cm peak may appear closer to the central star than the 18 cm peak. However, since the uncertainty in the absolute position for the 18 cm data is about 0.″1, observations with higher absolute positional accuracy are needed to confirm this spatial shift.

The OH 1665 and 1667 MHz main lines, as well as the OH 1612 and 1720 MHz satellite lines were all detected and imaged toward K 3-35. Figure 2 shows the RCP, LCP, I and V spectra made with the task ISPEC of AIPS, for the four ground state lines. The detected OH maser emission lines appear with LSR velocities $<$23 km s^{-1}, which are all blueshifted with respect to the systemic velocity of the source derived from the CO (2-1) molecular gas ($\sim$23 km s^{-1}; Tafoya et al., 2007). In general, the OH maser spectrum in an evolved star is characterized by two peaks which are blueshifted and redshifted, coming mainly from the front and back parts of the expanding envelope, respectively (Reid et al., 1977). In the presence of an ionized region, which is the case for K 3-35, and since the ionized gas can become optically thick at low frequencies, it is possible that the redshifted maser components, coming from the back side of the nebula, are not detected because the emission could be absorbed by the free-free opacity of the ionized gas (Rodríguez et al., 1985). This effect may explain why in K 3-35 all the OH maser features are blueshifted with respect to the systemic velocity.

In Table 4.2 we list the velocity and position of the peak flux density features for the OH RCP and LCP 1665, 1667, 1612 and 1720 MHz spectra (see Figure 2). The velocity and spatial distribution of the OH masers are shown in Figure 3. The positions were obtained by 2D Gaussian fitting in each velocity channel where the OH maser emission was above 5-σ level, with a typical uncertainty of 0.″05 (see Table 4.2). Only one single maser component was fitted per channel and in all cases it is spatially unresolved ($\leq$1″).

It can be noticed from Figure 3, that the masers for the different transitions are located toward different regions of the nebula. In particular, the OH 1665 and 1720 masers have a compact distribution, around the 1.3 cm continuum emission peak, compared with the 1612 and 1667 masers that appear in a more extended area (see Figure 3). On the other hand, the OH 1665 and 1667 MHz masers are tracing different kinematic components, with the

Table 4.2. Peak flux density of the OH maser spectral features toward K 3-35

	RCP					LCP					
Transition MHz	V^a_{LSR} (km s^{-1})	S_ν (mJy)	α(J2000)^b (s)	δ(J2000)^b (")	Δ^c (")	V^a_{LSR} (km s^{-1})	S_ν (mJy)	α(J2000)^b (s)	δ(J2000)^b (")	Δ^c (")	m^d_c (%)
1665	21.0	61.6	44.020	03.40	0.04	21.0	42.4	44.020	03.40	0.05	+18
	20.1	66.1	44.020	03.40	0.06	20.1	14.6	43.991	03.60	0.10	+64
	18.6	37.0	44.020	03.30	0.10	18.6	482.0	44.0200	03.400	0.005	-86
	17.1	422.6	44.0200	03.400	0.007	17.1	36.5	44.027	03.60	0.15	+84
	15.0	82.1	44.020	03.400	0.04	15.0	474.8	44.0271	03.400	0.006	-71
	14.6	99.8	44.027	03.40	0.04	14.6	304.7	44.020	03.40	0.01	-51
1667	8.0	87.8	44.020	03.40	0.04	8.0	114.3	44.020	03.40	0.03	-13
	−3.5	43.0	44.027	03.60	0.07	−3.5	33.8	44.020	03.60	0.09	+12
1612	21.2	<30^e	...	...	...	21.2	774.3	44.018	03.46	0.02	-90
	18.4	383.2	44.021	03.33	0.06	18.4	578.6	44.020	03.34	0.04	-20
	8.8	1496.6	44.022	03.31	0.01	8.8	1815.8	44.024	03.37	0.01	-10
	−2.0	155.8	44.039	03.76	0.16	−2.0	261.6	44.032	03.62	0.08	-25
1720	21.4	838.7	44.0242	03.437	0.003	21.4	306.5	44.0251	03.425	0.007	+47

Note. — The dotted line means that no emission up to 5σ was detected in this velocity channel.

[a] is the velocity of each individual channel.

[b] Position obtained by a Gaussian fitting for the emission in each channel.

[c] Position error

[d] m_c is the percentage of circular polarization (V/I).

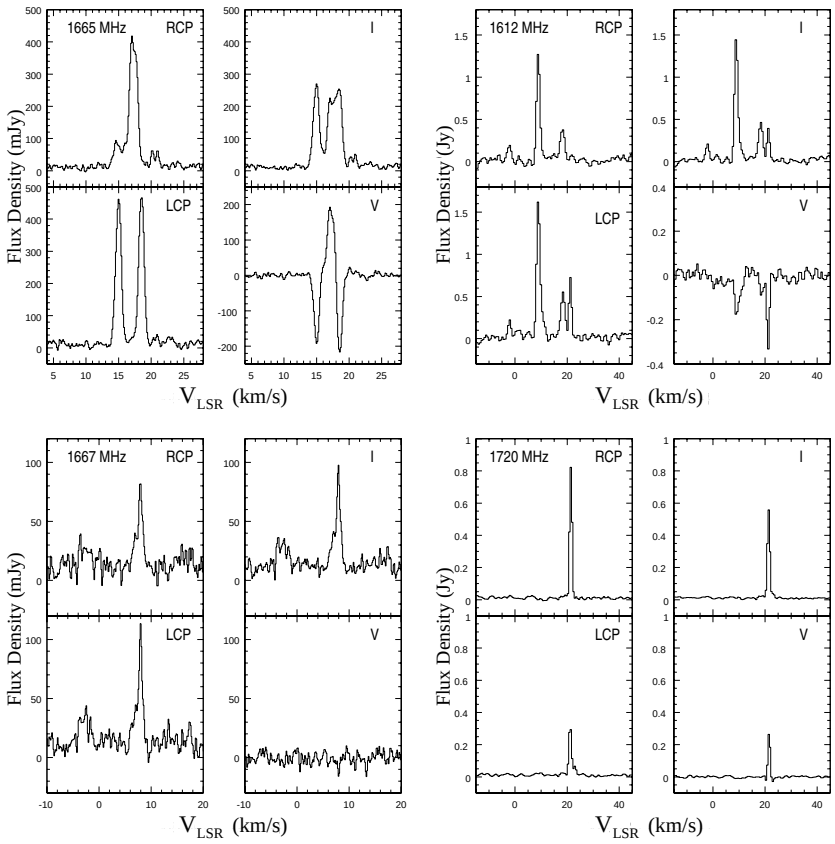

Figure 4.2: RCP, LCP, I and V spectra toward K 3-35, for the 1665, 1667, 1612, and 1720 MHz OH transitions. The spectra were obtained by integrating the emission in a box of 5″× 5″ centered on the continuum emission peak at 18 cm. The systemic V_{LSR} velocity of the source is ∼23 km s^{-1}. Note the "S" profile in the Stokes parameter V in the 1665 MHz transition at ∼18 km s^{-1}, indicating a Zeeman pattern.

1667 maser spots having velocities lower than 10 km s^{-1}. In what follows, we present an analysis of the spatial distribution, kinematics and polarization for each individual OH maser transition.

1665 MHz

Engels et al. (1985) did not detect the OH 1665 MHz transition toward

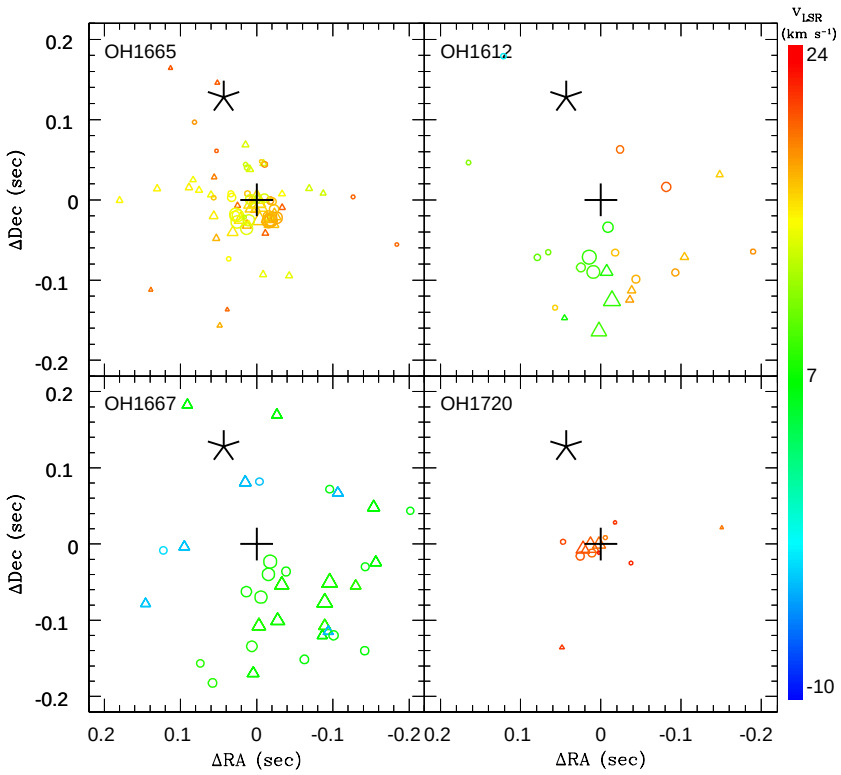

Figure 4.3: OH maser spots for the 1665, 1667, 1612 and 1720 MHz transitions toward the young PN K 3-35. The circles mark the left circular polarization (LCP) and the triangles the right circular polarization (RCP). Only maser spots in each individual velocity channel with signal-to-noise ratios >5 were plotted. The OH maser spots have been plotted with the same color-coded velocity that is shown at the right side. The symbol sizes are proportional to the square root of the integrated flux density. The black cross (0,0) marks the continuum peak position at 1.3 cm and the black star marks the peak position of the 18 cm continuum (see §3.1).

K 3-35 with a 3-σ sensitivity limit of 0.6 Jy. Miranda et al. (2001) detected and imaged for the first time the 1665 MHz transition toward K 3-35 using the VLA, reporting the presence of emission in a velocity range from +14 to +20 km s^{-1}. In this work (Figure 2 and Table 4.2) we confirm the presence of OH 1665 MHz maser emission, which covers the same LSR velocity range as reported by Miranda et al. (2001). The velocity and position of the OH 1665

MHz RCP and LCP peak flux density spectral features are listed on Table 4.2. The location of the OH 1665 maser spots (with signal-to-noise ratios > 5), appear slightly shifted to the south of the 18 cm radio continuum peak (see Figure 3). These features are constrained within $0\farcs1$ and are more coincident in position with the 1.3 cm radio continuum peak, which we think is closer to the central star. Almost all the OH 1665 MHz features exhibit a high degree of circular polarization above 50% and, in the particular case of the spectral feature in the velocity range from +17.5 to +18 km s^{-1}, the RCP and LCP emission is spatially coincident, suggesting the presence of a Zeeman pair.

1667 MHz

Two weak 1667 MHz spectral components toward K 3-35 were first reported by Engels et al. (1985) at LSR velocities of -4 and +7.8 km s^{-1}, and intensities of 0.3 and 0.4 Jy, respectively. Te Lintel Hekkert (1991) did not detect the OH 1667 MHz masers with an upper limit of 0.2 Jy. Miranda et al. (2001) reported the detection of 1667 MHz maser emission in two velocity ranges, from -2 to -3 km s^{-1} and from +7 to +9 km s^{-1}, with peak flux densities lower than 0.1 Jy. In this work we report the detection of two 1667 MHz spectral features at -3.5 and +8.0 km s^{-1} (see Figures 2, 3, and Table 4.2), that are spatially separated in two groups by about $0\farcs1$, toward the northeast and the southwest, respectively (see blue and green features in Figure 3). There is no significant circular polarization in the OH 1667 MHz masers ($\leq$16%; see Table 4.2) in agreement with the results of Miranda et al. (2001). The two features are blueshifted with respect to the systemic velocity of the PN ($\sim$ +23 km s^{-1}), suggesting that they are arising from the blueshifted lobe of the outflow. In any case, it is clear from Figure 3, that the 1667 maser emission is tracing a different region that the 1665 one.

1612 MHz

The OH 1612 MHz line was first detected toward K 3-35 by Engels et al. (1985) using the Effelsberg 100 m telescope. Three velocity features (at -4, +9 and +20 km s^{-1}) were reported, with the strongest feature ($\sim$ 4 Jy) at +9 km s^{-1}. Te Lintel Hekkert (1991), using the Nançay radio telescope, observed two 1612 MHz velocity features at $\sim$ +9 and +20 km s^{-1}. High spectral resolution 1612 MHz observations, carried out also with the Nançay radio telescope by Szymczak & Gérard (2004), showed the presence of four velocity

features (at −2, +9, +18 and +21 km s^{-1}). Interferometric VLA observations revealed the coincidence in position (within ∼0.″5) of the 1612 MHz maser emission and the continuum emission peak, supporting the association of the OH masers with K 3-35 (Aaquist, 1993). In this work we confirm that the OH 1612 maser emission is associated with K 3-35 (Figure 3). Four OH 1612 maser spectral features were detected at −2.0, +8.8, +18.4 and +21.2 km s^{-1} (Figure 2 and Table 4.2), in agreement with those reported by Szymczak & Gérard (2004). We note that the OH 1612 masers are displaced in position by about 0.″1 to the south of the 1.3 cm continuum peak and that they show an extended distribution in space (see Figure 3).

In Figure 2 we identify four main groups of 1612 MHz maser features. Two of them coincide in velocity with those of the 1667 MHz transition at ∼ −3.5 and +8 km s^{-1}, although only the group at +8 km s^{-1} coincides spatially with that of the 1667 MHz transition (see green color maser spots in Figure 3), suggesting that both the OH 1612 and 1667 velocity transitions are arising in the same region, (i.e. in the northern blueshifted lobe of the outflow) (Miranda et al., 2000). The third and fourth groups of OH 1612 MHz masers at ∼ +18 and +21 km s^{-1} appear in the same velocity range as the 1665 transition, and it is more likely that they are arising from an inner region of the nebula, close to the central star. All the features show circular polarization, with the highest polarized feature at +21 km s^{-1} (orange red color spots in Figure 3).

1720 MHz

The OH 1720 MHz maser emission has been detected previously toward K 3-35 by Te Lintel Hekkert (1991) when the classification of this object was still unclear. Now it is known that K 3-35 is a young PN (Miranda et al., 2001) and so far it is the only one that exhibits the OH 1720 MHz maser transition. Te Lintel Hekkert (1991) detected a single peak spectral component toward K 3-35 centered at +22.1 km s^{-1} with a total flux density of 3 Jy. Our 1720 MHz detection (see Figure 2) shows a narrow velocity feature centered at an LSR velocity of +21.4 km s^{-1} (0.6 Jy), coincident in position with the radio continuum peak at 1.3 cm (red color maser spots in Figure 3), suggesting that these masers originate very close to the central star.

The OH 1720 MHz maser emission is commonly associated with shocked molecular regions in star forming regions and supernovae remnants (Frail

et al., 1994). Recently, the 1720 MHz transition has been detected toward a few post-AGB stars (Sevenster & Chapman, 2001; Deacon et al., 2004). Elitzur (1976) has proposed that the only way to produce strong OH 1720 MHz maser emission is by means of collisional pumping under particular physical conditions ($T_{\rm k} \leq 200$ K; $n_{H_2} \simeq 10^5$ cm^{-3}). Sevenster & Chapman (2001) detected OH 1720 MHz maser emission toward the post-AGB star IRAS 18043−2116, and explained this emission as due to the passage of a C-type shock through the remnant AGB envelope caused by the fastwind. According to the scenario proposed by these authors, H_2O molecules would be formed behind the shock. Subsequently, the H_2O is photodissociated enhancing the OH abundance. The post-shock physical conditions are favorable for pumping the OH 1720 MHz maser transition. Even though these authors predicted that H_2O masers would not be present, Deacon et al. (2004) detected H_2O maser emission toward IRAS 18043−2116. These results suggest that the physical conditions in this source can be adequate to excite both the OH 1720 MHz and the H_2O maser emissions.

For K 3-35 we note that the velocity and location of the OH 1720 MHz masers are very similar to those of the H_2O masers (Miranda et al., 2001). This suggest that the pumping mechanism of the H_2O masers could be produced by the same shock that is exciting the OH 1720 MHz transition. The OH 1720 MHz maser emission has a high degree of circular polarization, ∼50% (Table 4.2), however, although the RCP and LCP maser features coincide in position (within 0.″04), they do not show the typical "S" profile, indicative of a Zeeman pattern in the Stokes parameter V.

4.4.2 Magnetic field in K 3-35

Polarization studies have been carried out toward proto-PNe using OH maser transitions (e.g. Bains et al., 2003; Szymczak & Gérard, 2004), H_2O masers (Vlemmings, et al., 2005; Vlemmings & van Langevelde, 2008) and SiO masers (Herpin et al., 2006), showing for some objects magnetic field components which are orthogonal to the major axis of the nebulae. Several PNe have been reported to harbor OH maser emission (Payne et al., 1988; Zijlstra et al., 1989; Bowers & Knapp, 1989; Te Lintel Hekkert & Chapman, 1996). However, the relatively weakness of the OH maser features difficults the detection of polarization using OH maser techniques. In the case of K 3-35, the OH maser emission is strong enough to allow us a detailed study of the polarization of these emission.

The existence of strong circular polarization in some features of the OH 1612, 1665 and 1720 MHz maser transitions suggests the presence of a magnetic field in K 3-35. In general, the field leads to a splitting of the magnetic substates of the OH molecule, which can be detected as a Zeeman pair (Davies, 1974; Crutcher & Kazes, 1983). Assuming that the source is permeated with the same strength of field then, if a Zeeman effect is present, the LCP and RCP components have to be emitted from the same region of the OH source.

Figure 4 shows a close up of the 1665 maser spots plotted in Figure 3 (upper left panel) but with masers that have flux densities above 15σ. The velocity and position of these RCP and LCP 1665 maser features are mainly distributed in three spatial regions: one apparently coincident with the 1.3 cm continuum emission peak (marked with the upper square in Figure 4) and the other two located toward the southeast (left square) and southwest (right circle) of the 1.3 cm radio continuum peak. The regions to the southeast and southwest correspond to the two LCP high intensity spectral features at $\sim$+15 and +18.6 km s^{-1}, respectively (see upper left panel in Figure 2), which are separated in position by about 0.″04. The relative position accuracy between the LCP 1665 masers is less than 0.″006, and the resulting velocity resolution (after Hanning smoothing) is $\sim$0.3 km s^{-1}, then we consider that this positional and spectral shift is real. The shift between these two groups of OH 1665 features may be simply due to inhomogenities of the gas at different velocities or they can reveal a true kinematic effect of a single structure. If we try to extrapolate the kinematics of the ring traced by the H_2O masers (Uscanga et al., 2008), we note that the sense of rotation for the H_2O ring is not in agreement with the velocity gradient of the two OH 1665 MHz groups (see bottom left panel of Figure 4). We suggest that only the group of masers around +18.6 km s^{-1} could be associated with dense gas close to the central star, likely in an equatorial torus, but the OH 1665 masers at $\sim$+15 km s^{-1}, would be associated with the blueshifted lobe of the outflow as in the case of the 1667 and 1612 MHz masers.

We also note that the 1665 RCP and LCP maser spots with velocity $\sim$ +17.5 to +18 km s^{-1}, overlap each other (see black circle in upper-left panel of Figure 4). In this sense, the OH 1665 transition has a velocity component that seems to follow the physical requirements for a Zeeman pattern (they exhibit the typical "S" shape in the Stokes V spectrum shown in Figure 2). Assuming that these masers are arising from the same spatial region (within 0.″03) and that we have at least one Zeeman pair in the velocity range between

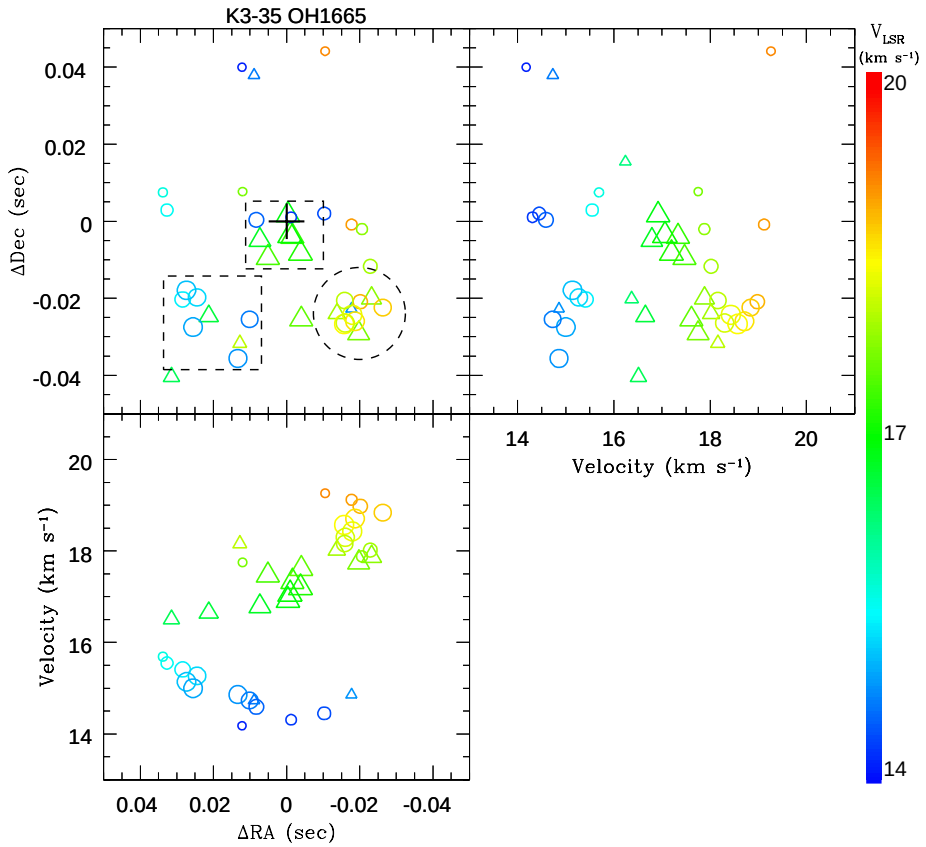

Figure 4.4: Close-up of the position-velocity diagrams for the 1665 MHz transition along the declination (top-right panel) and right ascension (bottom-left panel) of K 3-35. Only maser spots above 15σ were plotted, in order to note the three different groups that have been mark with two black dashed squares and one black dashed circle. The OH maser spots have been plot with the same color-coded velocity. The color circles mark the left circular polarization (LCP) and the triangles the right circular polarization (RCP) features. The black dashed circle marks the region where we suggest there is a Zeeman pair (see §3.2). The cross indicates the 1.3 cm peak continuum position.

+17.5 to +18 km s^{-1}, we can estimate the magnitude of the magnetic field along the line-of-sight (B_{LOS}).

It is known that when the Zeeman splitting is small compared to the

line width, the Stokes V spectrum is given by V = $\mathrm{d}I/\mathrm{d}\nu$ b B_{LOS} Hz $\mu\mathrm{G}^{-1}$ (Heiles et al., 1993; Robishaw et al., 2008), where $\mathrm{d}I/\mathrm{d}\nu$ is the frequency derivative of the Stokes I spectrum and b is the splitting coefficient (b=3.270 for the OH 1665 MHz transition; Davies, 1974). In terms of the velocity, the previous expression will be V = 3.27 c/ν_0 $\mathrm{d}I/\mathrm{d}v$ B_{LOS} Hz $\mu\mathrm{G}^{-1}$, where c=3×10^5 km s^{-1} and ν_0=1665×10^6 Hz. After doing the following scaling, V=0.55 km s^{-1} $\mathrm{d}I/\mathrm{d}v$, we estimate $\mathrm{B}_{LOS} \simeq 0.9 \pm 0.1$ mG, at a distance, from the 1.3 cm continuum peak, of ∼0.″03 (∼ 150 AU).

A comparison between the magnetic field estimates toward evolved stars as function of distance from the star has been made by Vlemmings, et al. (2005), plotting two models: solar-type (α=−2, B∝r$^{\alpha}$) and for a dipole medium (α=−3). Plotting the strength of the magnetic field of K 3-35 in figure 6 of Vlemmings, et al. (2005), shows that it is in agreement with a solar-type.

4.5 Conclusions

Using the VLA we detected and imaged the 1612, 1665, 1667 and 1720 MHz OH masers toward K 3-35. The velocity and position distribution of the masers suggest that they are arising from different regions in the nebula. The 1665 and 1720 MHz maser features have a compact distribution, near the 1.3 cm continuum emission peak, and it is possible that some features of the 1665 MHz transition are originating in an equatorial disk. The 1612 and 1667 MHz maser features are spread in a more extended region in two main velocity groups. We suggest that the velocity component at ∼ +8.0 km s^{-1} in the 1612 and 1667 MHz spectra could be tracing the same region near the central core in the blueshifted lobe of the outflow. As far as we know, K 3-35 is the only PN that exhibits simultaneously OH 1720 MHz and H_2O maser emission. We note that the velocity and location of the OH 1720 MHz masers are very similar to those of the H_2O masers. This suggests that the pumping mechanism of the H_2O masers could be produced by the same shock that is exciting the OH 1720 MHz transition. The 1612, 1665, and 1720 MHz spectra show some velocity features with a high degree of circular polarization (>50%). In the particular case of the velocity feature at ∼ +18 km s^{-1} in the OH 1665 MHz transition, it shows the typical "S" profile for the Stokes V, and the LCP and RCP features are arising from the same spatial position (within ∼0.″03 in diameter). This result suggests

that a Zeeman pair could be present in K 3-35 and a magnetic field in the line-of-sight of $\sim$0.9 mG, at a radius of 150 AU, is estimated. This magnetic field value is in agreement with a solar-type (α=$-$2, B$\propto$r$^{\alpha}$) magnetic field associated with evolved stars.

Perhaps they are not stars, but rather openings in heaven where the love of our lost ones pours through and shines down upon us to let us know they are happy.

Eskimo Proverb

5

A collimated, ionized bipolar structure and a high density torus in the young planetary nebula IRAS 17347−3139*

D. Tafoya, Y. Gómez, N. A. Patel, J. M.Torrelles, J. F. Gómez, G. Anglada, L. F. Miranda, and I. de Gregorio-Monsalvo

5.1 Abstract

We present observations of continuum (λ = 0.7, 1.3, 3.6 and 18 cm) and OH maser (λ = 18 cm) emission toward the young planetary nebula IRAS 17347−3139, which is one of the three planetary nebulae that are known to harbor water maser emission. From the continuum observations we show that the ionized shell of IRAS 17347−3139 consists of two main structures: one extended (size $\sim 1\farcs5$) with bipolar morphology along PA=−30°, elongated in the same direction as the lobes observed in the near-infrared images, and a central compact structure (size $\sim 0\farcs25$) elongated in the direction perpendicular to the bipolar axis, coinciding with the equatorial dark lane observed in the near-infrared images. Our image at 1.3 cm suggests the presence of dense walls in the ionized bipolar lobes. We estimate for the central compact structure a value of the electron density at least $\sim$ 5 times higher than in the lobes. A high resolution image of this structure at 0.7 cm shows two peaks separated by about $0\farcs13$ (corresponding to 100-780 AU, using a distance range of 0.8−6 kpc). This emission is interpreted as originating in

*Published in the Astrophysical Journal ,2009, Volume 691, Issue 1, pp. 611-620.

an ionized equatorial torus-like structure, from whose edges the water maser emission might be arising. We have detected weak OH 1612 MHz maser emission at $V_{\rm LSR} \sim -70$ km s^{-1} associated with IRAS 17347−3139. We derive a 3σ upper limit of $< 35\%$ for the percentage of circularly polarized emission. Within our primary beam, we detected additional OH 1612 MHz maser emission in the LSR velocity ranges -5 to -24 and -90 to -123 km s^{-1}, associated with the sources 2MASS J17380406−3138387 and OH 356.65−0.15, respectively.

5.2 Introduction

The study of transition objects from the asymptotic giant branch (AGB) to the planetary nebula (PN) phase is very important to understand the processes by which low and intermediate mass stars evolve. It has been observed that planetary nebulae (PNe) display a large variety of morphologies, including bipolar or multipolar structures (Balick 1987; Schwarz, Corradi, & Melnick 1992; Manchado et al. 1996). However, it is not well understood how they develop such morphologies. Given that the transition phase occurs in a very short time scale of ~ 1000 years (Kwok 1993), only a few objects are expected to be in this evolutionary stage, making the observational study of the physical conditions under which they evolve a difficult task. A simple model which in general explains the development of bipolar morphologies in PNe is the generalized interacting stellar winds (GISW) model (Kahn & West 1985; Balick 1987; Icke 1988, Mellema et al. 1991). This model assumes that the "superwind", expelled during the AGB phase, produces a circumstellar envelope (CSE) which has a latitude-dependent density profile, with an enhancement in the equatorial region and decreasing monotonically toward the poles. Subsequently, the slow massive wind is replaced by a fast tenuous wind; the latter interacts hydrodynamically with the former, resulting in the creation of the bipolar lobes (Mellema et al. 1991, Frank et al. 1993, García-Segura et al. 1999, Balick & Frank 2002).

High sensitivity and angular resolution images of PNe obtained with the Hubble Space Telescope (HST) have revealed collimated structures whose formation cannot be explained by the GISW model (Miranda & Solf 1992; Sahai & Trauger 1998). The presence of a companion, collimated outflows (e.g. Sahai & Trauger 1998; Soker & Rappaport 2000; Velázquez et al. 2007) or magnetic fields (e.g. García-Segura et al. 1999), are required in most

cases to explain the formation of such collimated structures. Nonetheless, the existence and study of a disk or an equatorial density enhancement in the CSE is considered a key ingredient to understand the processes that form bipolar lobes. A detailed study of particular PNe can provide crucial information about the physical conditions under which they develop their morphologies, and help to determine the relevance of the different shaping mechanisms proposed.

IRAS 17347−3139 is a young PN with a clear bipolar morphology, as revealed by the near-infrared images (de Gregorio-Monsalvo et al. 2004 [hereafter dGM04], Sánchez-Contreras et al. 2006; Sahai et al. 2007). The lobes show an extent of $\sim 4''$, separated by a dark lane, which probably is tracing a dense dusty equatorial region. Sánchez-Contreras et al. (2006) suggest that the limb brightened appearance of the lobes could be indicating the presence of bubble-like structures with dense walls and tenuous interiors, presumably excavated by jet-like winds.

dGM04 detected water masers arising from this young planetary nebula. Up to now, only other two PNe are known to exhibit water maser emission (Miranda et al. 2001; Gómez et al. 2008). Since the water maser emission is expected to last for a very short period after the intense mass-loss rate stops, at the end of the AGB phase ($\sim$ 100 yr, Gómez, Moran & Rodríguez 1990), the detection of this emission suggests that these stars have entered the PN phase only some decades ago, making this objects good candidates to study the early stages of PN formation. On the other hand, the nature of the radio continuum emission in IRAS 17347−3139 has been discussed by dGM04 and Gómez et al. 2005 (hereafter G05). These authors showed that the flux density of IRAS 17347−3139 rises with frequency, deriving a spectral index $\alpha \simeq 0.7$ ($S_\nu \propto \nu^\alpha$), between 4.9 and 22 GHz, which was interpreted in terms of free-free emission from an ionized nebula. Moreover, G05 found that the radio continuum flux density is increasing rapidly with time. They estimated a dynamic time scale for the ionized envelope of $\sim$ 100 yr, supporting the idea that this star entered the PN phase only some decades ago.

OH maser emission at 1612 MHz toward IRAS 17347−3139 was first reported by Zijlstra et al. (1989). Recently, Szymczak and Gérard (2004) presented single-dish polarimetric observations of OH masers toward this source. However, the association of this emission with the PN is uncertain due to the low angular resolution of their observations.

In order to clarify some questions originated in previous works, and to further investigate the PN IRAS 17347−3139, we have carried out high sen-

sitivity and angular resolution continuum and OH maser observations with the Very Large Array (VLA). This work is structured as follows: In § 2 we describe the new observations that allowed us to image with higher sensitivity and higher angular resolution the ionized envelope of this source. The results are presented in § 3, the analysis of the data is discussed in § 4, and the conclusions are given in § 5.

5.3 Observations and data reduction

On 2005 January 27, we used the VLA of the NRAO[2] in the hybrid configuration BnA, to carry out continuum observations of IRAS 17347−3139 at frequencies 8.46, 22.46 and 43.34 GHz (λ = 3.6, 1.3 and 0.7 cm, respectively). We used 2 IF's covering a total bandwidth of 100 MHz with two circular polarizations. At 0.7 and 1.3 cm we used the fast switching mode, changing from source to phase calibrator every 80 seconds in order to correct for the quick variations in the troposphere. As the phase tracking center, we used the position of the peak of the radio continuum reported by dGM04: α(J2000.0) = $17^{\rm h}38^{\rm m}00\overset{\rm s}{.}586$, δ(J2000.0) = $-31°40'55\overset{''}{.}67$. The source J1335+305 (3C 286) was used as the flux calibrator while J1744−312 was the phase calibrator. Table 5.1 lists the flux densities of the calibrators at the different frequencies. The total time on source was 0.6, 0.5 and 1.1 hrs at λ = 3.6, 1.3 and 0.7 cm, respectively.

We also carried out, with the VLA-BnA configuration, spectral line observations of four OH transitions with rest frequencies: 1612, 1665, 1667 and 1720 MHz. The 1665 and 1667 MHz observations were carried out on 2005 January 28, while the 1612 and 1720 MHz observations were carried out on 2005 January 29. For each transition we observed both right and left circular polarizations (RCP and LCP, respectively). We sampled 256 channels in a total bandwidth of 1.5625 MHz, centered at $V_{\rm LSR}$=−40 km s^{-1}, resulting in a spectral resolution of 6.1035 kHz ($\simeq$ 1.1 km s^{-1}). In addition, for the 1612 MHz transition, we used a narrow-band filter to avoid radio frequency interference due to the Iridium satellites. The sources 3C 286 and J1751−253 were the flux and phase calibrators, respectively (see flux densities in Table 5.1). From the spectral data of each transition we have obtained a continuum data set by averaging channels free of maser emission. The four continuum data

[2]The National Radio Astronomy Observatory is a facility of the National Science Foundation operated under cooperative agreement by Associated Universities, Inc.

Table 5.1. Set up of the observations

Frequency (GHz)	Phase Calibrator	Flux Density[a] (Jy)	Flux Calibrator	Flux Density[b] (Jy)
1.612	J1751-253	0.94 ± 0.01	3C 286	13.85
1.665	”	1.04 ± 0.01	”	13.63
1.667	”	1.05 ± 0.01	”	13.62
1.720	”	1.03 ± 0.01	”	13.41
8.460	J1744-312	0.78 ± 0.01	”	5.21
22.460	”	0.91 ± 0.02	”	2.52
43.340	”	1.08 ± 0.06	”	1.45

[a]Bootstrapped flux density for phase calibrator.

[b]Assumed flux density for flux calibrator.

sets were calibrated separately. Subsequently, during the imaging process, they were concatenated to produce a single continuum data set.

The calibration and data reduction were carried out using the Astronomical Image Processing System (AIPS) of the NRAO. We followed the standard procedures for reducing high-frequency data outlined in Appendix D of the AIPS Cookbook (2007). Since 3C 286 is resolved at some of the observation frequencies, we used an image model for this source in the calibration process. The data for the continuum observations were self-calibrated in phase (except at λ=18 cm), then Fourier transformed, weighted, and CLEANed to generate the final images.

5.4 Results

5.4.1 Radio continuum

Since the first detection by Zijlstra et al. (1989), it is known that IRAS 17347−3139 presents radio continuum emission. However, there were no radio images of this source reported in the literature. From our observations, we have obtained high sensitivity and high angular resolution interferometric images of IRAS 17347−3139 at wavelengths 18, 3.6, 1.3 and 0.7 cm (Figs. 5.1, 5.2, 5.3 and 5.4). This is the first time that the radio emission from this PN has been resolved spatially.

At 3.6 and 1.3 cm (Figures 5.2 and 5.3, respectively) the radio contin-

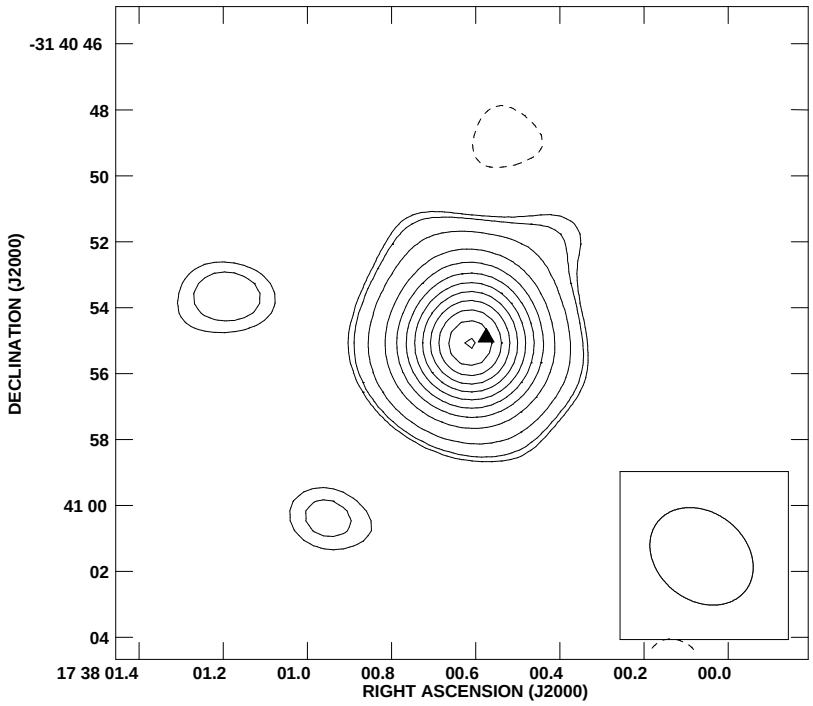

Figure 5.1: VLA image of IRAS 17347−3139 at wavelength 18 cm using a ROBUST weight parameter = 0. Contours are −3.7, 3.7, 5, 10, 20, 30, 40, 50, 60, 70, 80, 90, and 99 per cent of 2.4×10^{-2} Jy/beam, the peak value of the brightness. The first contours are -3 and 3 times the rms noise of the image, 2.9 $\times10^{-4}$ Jy/beam. The synthesized beam is shown in the bottom right corner, and its size is $3\farcs38 \times 2\farcs67$ (PA = $52°$). The position of the OH 1612 MHz maser associated to IRAS 17347−3139 is show as a filled triangle.

uum emission shows a bright central region and a fainter extended structure elongated in the northwest-southeast direction (P.A. = $-30°$). Particularly, in the image at 1.3 cm, the extended emission shows a double horn structure in the nortwest-southeast direction with an opening angle of about 30°. This structure also appears in the near-infrared emission (see also dGM04; Sánchez-Contreras et al. 2006, Sahai et al. 2007). The bright emission of the central region at 1.3 cm seems slightly elongated in the direction perpendicular to the extended structure. This elongation of the central region is more clearly seen in the image at 0.7 cm (Fig. 5.4).

We fitted two bi-dimensional Gaussian components to the emission ob-

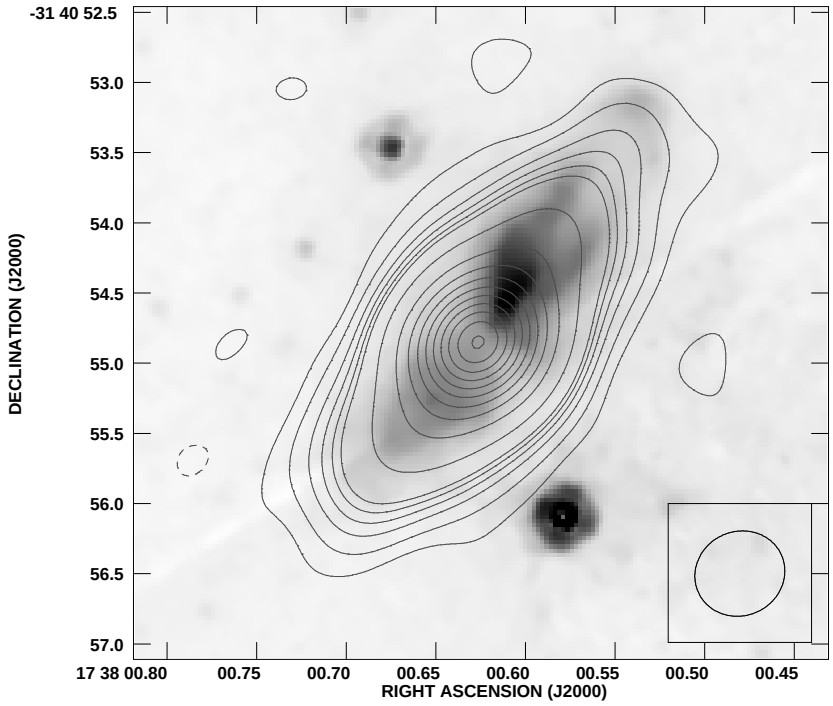

Figure 5.2: Contours: VLA image of IRAS 17347−3139 at wavelength 3.6 cm using a ROBUST weight parameter = 0. Contours are −0.31, 0.31, 1, 2, 3, 4, 5, 10, 20, 30, 40, 50, 60, 70, 80, 90 and 99 per cent of 7 $\times 10^{-2}$ Jy/beam. The value of the first contour is 3 times the rms noise of the image, 7.2 $\times 10^{-5}$ Jy/beam. The synthesized beam is shown in the bottom right corner, and its size is $0\farcs65 \times 0\farcs60$ (PA = $-65°$). Grey scale: HST IR image of IRAS 17347−3139 at 1.1 μm obtained with the NIC1 in the F110W filter. In order to make coincide the nominal position of the IR emission with the peak of the radio continuum, the IR image has been shifted $\sim 0\farcs5$ to the southeast.

served at 3.6 cm, and also to the emission at 1.3 cm, in order to estimate the size and orientation of both the compact (central region) and extended emission. At 18 and 0.7 cm only one Gaussian component was fitted[3]. For the fitting process, we used images reconstructed with the ROBUST parameter (Briggs 1995) set to +5 in order to recover as much faint extended emission as possible, then we used the task JMFIT of AIPS to fit the Gaussians. The

[3]We tried to fit two Gaussian components to the emission at 0.7 cm but, due to the low signal-to-noise ratio of the extended structure, the fitting was doubtful.

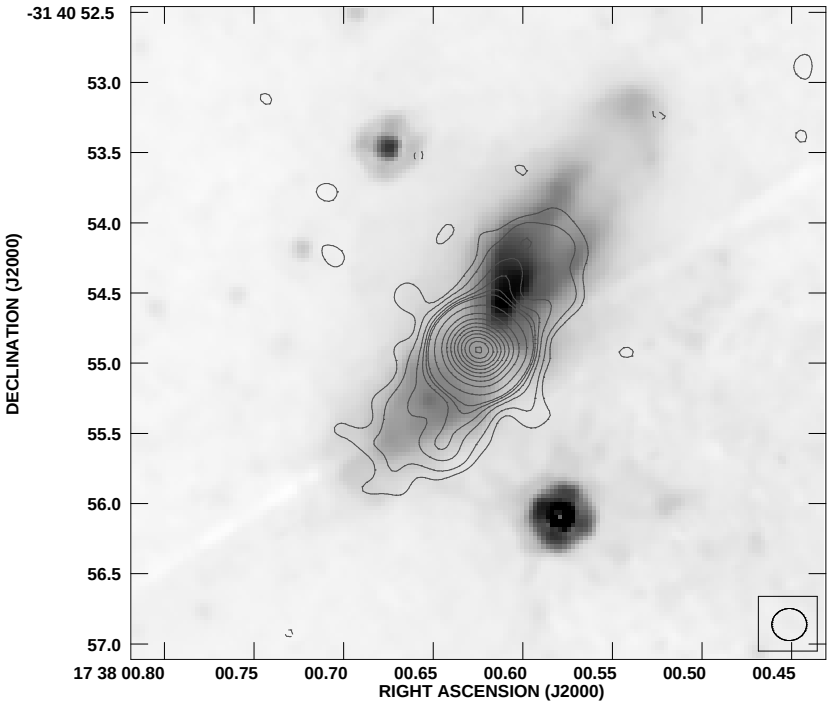

Figure 5.3: Contours: VLA image of IRAS 17347−3139 at wavelength 1.3 cm using a ROBUST weight parameter = 0. Contours are −0.53, 0.53, 1, 2, 3, 4, 5, 10, 20, 30, 40, 50, 60, 70, 80, 90 and 99 per cent of 1.1 $\times 10^{-1}$ Jy/beam, the peak value of the brightness. The value of the first contour is 3 times the rms noise of the image, 2.1×10^{-4} Jy/beam. The synthesized beam is shown in the bottom right corner, and its size is $0\farcs25 \times 0\farcs23$ (PA = $-88°$). Grey scale: HST IR image of IRAS 17347−3139 at 1.1 μm obtained with the NIC1 in the F110W filter.

results of the fitting are shown in Table 5.2. From these images (ROBUST = +5), we also measured the total flux density of the source within a box containing the whole emission (Table 5.3). We notice that the total flux density at 1.3, 3.6 and 18 cm is compatible with the sum of the flux densities of the fitted Gaussian components. At 0.7 cm, the flux of the fitted Gaussian is lower than the total flux of the source. This is probably due to the presence of extended faint emission not fitted by a single Gaussian component. Therefore, in Table 5.2, we attribute the residual flux density from the Gaussian fitting at 0.7 cm to the extended structure.

In Figure 5.5 we compare our measurements of the total flux density with

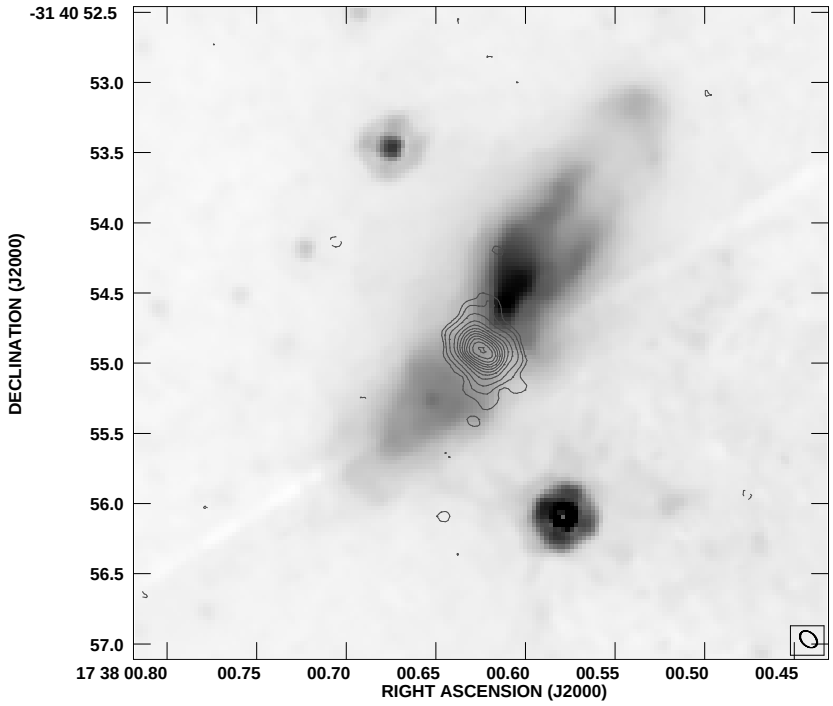

Figure 5.4: Contours: VLA image of IRAS 17347−3139 at wavelength 0.7 cm using a ROBUST weight parameter = 0. Contours are −2.5, 2.5, 3, 5, 10, 20, 30, 40, 50, 60, 70, 80, 90, 99 per cent of 7.35×10^{-2} Jy/beam, the peak value of the brightness. The value of the first contours are -3 and 3 times the rms noise of the image, 6.2 $\times10^{-4}$ Jy/beam. The synthesized beam is shown in the bottom right corner, and its size is $0\farcs14 \times 0\farcs10$ (PA $= 46°$). Grey scale: HST IR image of IRAS 17347−3139 at 1.1 μm obtained with the NIC1 in the F110W filter.

those of previous works and epochs. We noticed that the flux densities that we obtained follow an increasing trend with time, just as it was found previously by G05. A possible explanation of the increase in flux density could be the expansion of the ionized nebula (given that the spectral index does not vary significantly between the different epochs). From our observations we estimate a spectral index in the frequency range from 1.6 to 43 GHz of $\simeq 0.81$, which is similar to the values found by dGM04 and G05. Using the values of the flux density at 3.6 cm from our observations and from those of dGM04 and G05, assuming a constant expansion velocity, we estimate a kinematical age for the ionized nebula of about 100 years. This value is

Table 5.2. Parameters of the gaussian fitting to the continuum emission of IRAS 17347-3139[a]

	Compact region			Extended region		
Frequency (GHz)	Flux density (mJy)	Size[b] (arcsec × arcsecs)	P.A. (degrees)	Flux density (mJy)	Size[b] (arcsec × arcsecs)	P.A. (degrees)
1.666[c]	...	...	...	31±1	2.20×0.40	−29.8
8.460	56±1	0.33×0.19	16.1	70±1	1.57×0.40	−32.9
22.460	207±1	0.25×0.22	57.8	69±2	1.42×0.47	−32.7
43.340	375±2	0.25×0.19	50.4	65±10[d]	...	...

[a]Two gaussian components fitting, except for the data at 1.666 and 43.340 GHz.

[b]Deconvolved size.

[c]Average frequency of the four OH transitions (see §2).

[d]Residual flux density from the single Gaussian fit of the compact region (see §3.1).

Table 5.3. Continuum emission of IRAS 17347-3139

Frequency (GHz)	Flux density[a] (mJy)	RA(J2000)[b] (h m s)	Dec(J2000)[b] (° ′ ″)	Position Uncertainty[c] (arcsec)
1.666[d]	31 ± 1	17 38 00.61	−31 40 55.0	0.4
8.460	127 ± 1	17 38 00.63	−31 40 54.9	0.1
22.460	280 ± 2	17 38 00.624	−31 40 54.90	0.05
43.340	440 ± 10	17 38 00.624	−31 40 54.91	0.05

[a]Total flux density of the emission. The uncertainties were obtained using 1 σ the *rms* noise of the image.

[b]Position of the emission peak obtained from a Gaussian fitting.

[c]Absolute position error.

[d]Average frequency of the four OH transitions (see §2).

consistent with the result obtained by G05.

In Table 5.3 we list the continuum peak positions of the source at the different frequencies. At ν = 8.46, 22.46 and 43.34 GHz (for which the source is better resolved), they coincide within 0.″06 from each other. When this position is compared with the nominal infrared position of the nebula obtained from the HST image, the difference is of about 0.″5. We note, however, that the position we have measured for the peak emission differs by about 0.″9 from that given by dGM04, that was obtained from data with a lower angular resolution. Since the newer specific procedures to calibrate high frequency data were not used by dGM04, we attribute this difference to their absolute positional error, that appears to be $\sim 1''$.

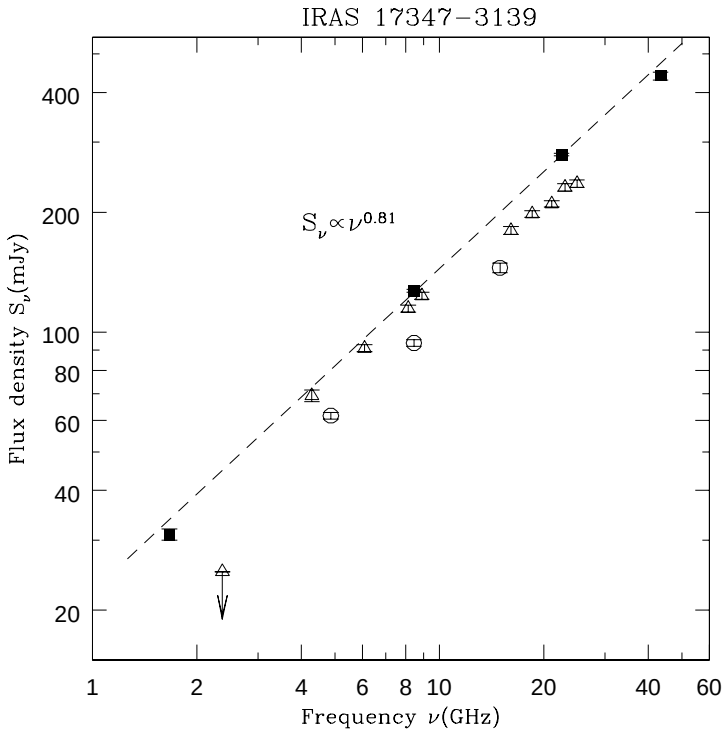

Figure 5.5: Spectral energy distribution of IRAS 17347−3139 in the range ∼ 1-43 GHz. The filled squares represent the flux densities obtained from our observations [epoch 2005.1]. The open triangles come from the observations carried out by G05 [epoch 2004.2]. The open circles come from the observations carried out by dGM04 [epoch 2002.5]. Note the increasing trend of the flux density of the source with time. The dashed line is a linear fit to the data from our observations.

5.4.2 OH Maser Emission

Among the four OH maser transitions observed at $\lambda \sim 18$ cm, we only detected the line at 1612 MHz toward IRAS 17347−3139. In Table 5.4 we give the parameters of the OH maser line detected. The OH 1612 MHz maser emission is slightly displaced to the north-west from the peak of the radio continum at 18 cm ($\sim 0\farcs5$, Figure 5.1). In Figure 5.6 (left panel) we present the spectra of the RCP and LCP ($S_{\rm RCP}$ and $S_{\rm LCP}$, respectively), as well as the total flux density (Stokes I=$[S_{\rm RCP}+S_{\rm LCP}]/2$) and the circular polarization (Stokes V=$[S_{\rm RCP}-S_{\rm LCP}]/2$) spectra. In both polarizations there

Table 5.4. OH 1612 MHz maser emission[a]

Source name	RA(J2000)[b] (h m s)	Dec(J2000)[b] (° ′ ″)	LSR Velocity range (km s^{-1})	Flux density[c] (mJy)	rms noise (mJy/beam)[d]
IRAS 17347−3139	17 38 00.57	−31 40 54.9	−70	38 ± 7	4
OH 356.65−0.15	17 38 00.66	−31 51 54.4	3	335 ± 7	4
	17 38 00.65	−31 51 54.4	−22	543 ± 7	4
J17380406−3138387	17 38 04.10	−31 38 38.3	−95	30 ± 7	4
	17 38 04.06	−31 38 38.6	−123	200 ± 7	4

[a]No emission has been detected from the 1665, 1667 and 1720 MHz OH maser transitions. The *rms* noise is 4 mJy/beam for all the transitions.

[b]Position of the emission peak of the observed spectral feature obtained from a Gaussian fitting. The absolute position error is 0.″4

[c]Peak flux density of the observed spectral feature (The integration region was 6.″5 × 5.″5 for IRAS 17347−3139, and 8″×8″ for OH 356.65−0.15 and J17380406−3138387). The uncertainties were obtained using 1 σ the *rms* noise of the image.

[d]1 σ the *rms* noise per channel. The size of the synthesized beam is 4.″4 × 2.″8 (Position angle = 65 degrees)

is only one feature at velocity $V_{\rm LSR} \simeq -70$ km s^{-1} with a flux density of $\simeq 40$ mJy. From the Stokes V spectrum we do not find evidence of the presence of circular polarized emission. We estimate a 3-σ upper limit of $< 35\%$ for the percentage of circularly polarized emission (m_c=|V|/I).

In addition to the OH 1612 MHz maser emission coming from IRAS 17347−3139, we also detected this line from two other positions that are located within the primary beam of our observations, which is 30′ at this frequency. One $\sim$ 2.′5 northeast from IRAS 17347−3139 and the other is $\sim$ 11′ south from this PN (see Table 5.4). The maser emission located toward the northeast appears in the velocity range from −125 to −95 km s^{-1} (right panel of Figure 5.6), which is very similar to the velocity range of the OH maser emission that Zijlstra et al. (1989) reported to be associated with IRAS 17347−3139. However, from our observations we found that the position of the OH maser emission in this velocity range coincides with the 2MASS source J17380406−3138387. On the other hand, the emission located toward the south of the position of IRAS 17347−3139 appears in the velocity range from −23 to 5 km s^{-1} (right panel of Figure 5.6). This emission is associated with the source OH 356.65−0.15 and was already reported by Bowers & Knapp (1989). Recently Szymczak & Gérard (2004) reported OH maser emission toward IRAS 17347−3139 in the same velocity range. However, due to the low angular resolution of their observations, probably they were contaminated by emission from the source OH 356.65−0.15.

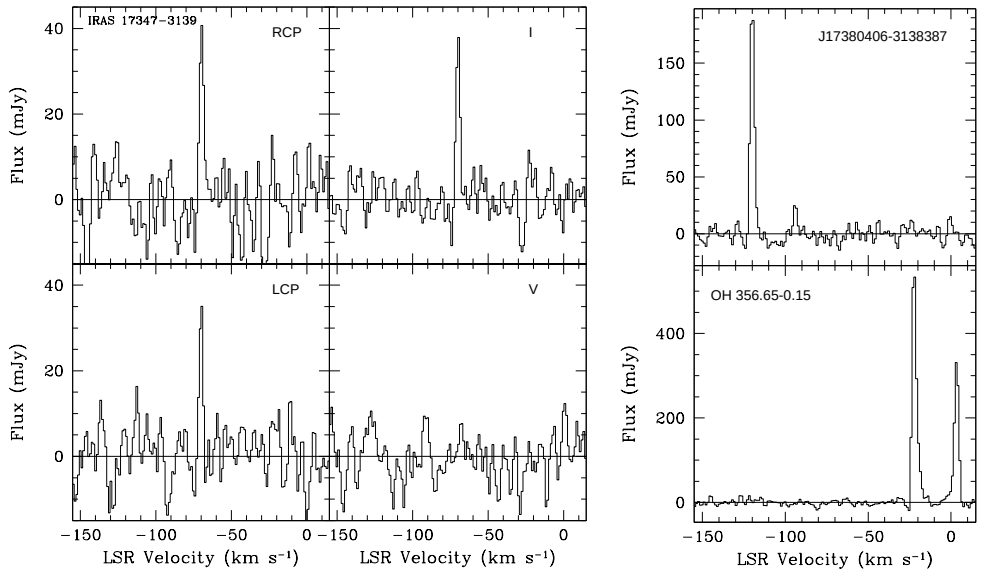

Figure 5.6: Left panel: Spectra of the right and left circular polarizations, as well as those of the total flux density (I) and polarization (V) of the OH 1612 MHz maser emission toward IRAS 17347−3139. Right panel: OH 1612 MHz maser emission from two other sources in the field (see §3.2).

5.5 Discussion

The spectrum of the free-free emission of an ionized region depends on the geometry, as well as on the electronic density and temperature distributions inside the region. For the simplest case of an isothermal, homogeneous ionized region the value of the spectral index, α (where $S_\nu \propto \nu^\alpha$), ranges from $+2$ (at low frequencies, where all the emission is optically thick) to -0.1 (at high frequencies, where all the emission is optically thin). The maximum flux density is reached at the "turnover frequency", ν_m, where the optical depth is of the order of unity and the spectrum becomes flat. In general, for a non-homogeneous ionized region, the spectral index of the free-free emission is the result of contributions from lines of sight with different optical depths. For the case of an isothermal, ionized region where the electron density goes as the inverse square of the radius ($n_e \propto r^{-2}$), the emission from the inner part of the region would be optically thick, while that from the outer parts

would be optically thin, resulting in a constant value of the spectral index $\alpha = +0.6$ over a wide range of frequencies (Panagia & Felli 1974; Olnon 1974; Reynolds 1986). If the ionized region is truncated at an inner radius r_0, there is a turnover frequency, where all the emission is optically thin and the spectrum becomes flat. These properties are true both for a spherically symmetric region and for a biconical (constant opening angle) region. This is also true for a constant velocity ionized spherical (or biconical) wind since in this case the electron density also decreases as the square of the radius (if the ionized fraction remains constant). If the density decreases steeply (e.g., in an accelerating wind), then the value of spectral index would be higher than +0.6, while a smaller value of the spectral index would indicate a flatter density distribution (e.g., in a decelerating wind).

The spectral index of the radio emission from IRAS 17347−3139 is $\alpha \simeq 0.81$ (Fig. 5.5) in the range of frequencies from 1.6 to 43 GHz. This can be interpreted in terms of an ionized region in which the electron density decreases as $n_e \propto r^{-2.3}$. This density distribution could correspond to a wind with an almost constant velocity ($v \propto r^{0.3}$). dGM04 and G05 discussed the possibility of the presence of an ionized wind in IRAS 17347−3139, but the mass-loss rate derived from that assumption, $\dot{M}_i \simeq 10^{-4}\ (D/\mathrm{kpc})^{3/2}\ M_\odot\ \mathrm{yr}^{-1}$, is far larger than the values observed in central stars of PNe and pre-PNe ($\leq 10^{-7}\ M_\odot\ \mathrm{yr}^{-1}$; Patriarchi & Perinotto 1991; Vassiliadis & Wood 1994). As a result, these authors interpreted the emission as arising from a recently ionized nebula.

Our new observations provide further insights on the nature of the radio emission of IRAS 17347−3139. As metioned in § 3.1, our high angular resolution images reveal the presence of two structures elongated in more or less perpendicular directions. In fact, the Gaussian fitting to the continuum emission of IRAS 17347−3139 (§ 3.1) shows that the central compact structure is elongated in the direction with P.A.$\simeq 50°$, while the extended structure is elongated in the direction with P.A.$\simeq -30°$. These directions correspond to those of the dark lane and the bipolar bright lobes observed in the IR images, respectively (see Figs. 5.2, 5.3, and 5.4). This alignment suggests that the radio continuum emission could be arising from two different components: an equatorial ionized torus-like structure, and two ionized bipolar lobes. To test this hypothesis, we analyzed the two components separately.

5.5.1 The Extended Ionized Emission

Since, as mentioned above, the spectrum of the free-free emission from an ionized region depends on the geometry and physical properties (T_e and n_e distributions), we can use this information to infer some of the properties of the extended structure. In Figure 5.7 (left panel) we have plotted the spectrum of the extended component, resulting from the values of the flux density obtained from the Gaussian fitting (§ 3.1). From 8.4 GHz to 43 GHz, the spectrum is flat, indicating that the turnover frequency is $\nu_m < 8.4$ GHz. There is only one measurement at frequencies lower than 8.4 GHz and, therefore, only a lower limit, $\alpha > +0.5$, can be obtained for the spectral index in the partially opaque regime. High angular resolution observations at 6 cm would be useful to constrain the value of this spectral index. Our observations show that the geometry of this component is not spherical, but has an aperture angle of $\theta_0 \simeq 30°$; therefore, it can be better described as a collimated ionized region. If we assume that the aperture angle is constant as a function of the distance to the central star (biconical structure), and that the inclination of this structure with respect to the plane of the sky is small, adopting an spectral index $\alpha \simeq +0.5$, a turnover frequency $\nu_m \simeq 8$ GHz, and an electronic temperature $T_e = 10^4$ K, we derive an inner radius $r_0 \simeq 0\farcs3$, and a density profile $n_e \propto r^{-1.9}$ (eqs. 15 and 18 from Reynolds 1986). A value of the spectral index higher than +0.5 would result in a density distribution decreasing steeply.

The electron density at radius r_0 is independent of α, and can be estimated from equation (13) of Reynolds (1986) as:

$$\left[\frac{n_0}{\mathrm{cm}^{-3}}\right] = 1.12 \times 10^3 \left[\frac{w_0}{\mathrm{arcsec}}\right]^{-0.5} \left[\frac{T_e}{\mathrm{K}}\right]^{0.675} \left[\frac{\nu_m}{\mathrm{GHz}}\right]^{1.05} \left[\frac{D}{\mathrm{pc}}\right]^{-0.5}, \qquad (5.1)$$

where $w_0 = \theta_0 r_0/2 \simeq 0\farcs08$) is the width of the ionized cone at radius r_0, and D is the distance to the source. For a distance range from 6 to 0.8 kpc (G05), we derive an electron density at the base of the lobes of $n_0 = 2\text{-}6 \times 10^5$ cm^{-3}. Although this is the maximum value of the density in the lobes, and the average value would be smaller (e.g., at $r = 1''$ the electron density would be ten times smaller than n_0), this high value of the electron density in the bipolar lobes supports the idea that this is a very young PN, and that the double horn structure seen at 1.3 cm (§3.1) could be tracing high density walls.

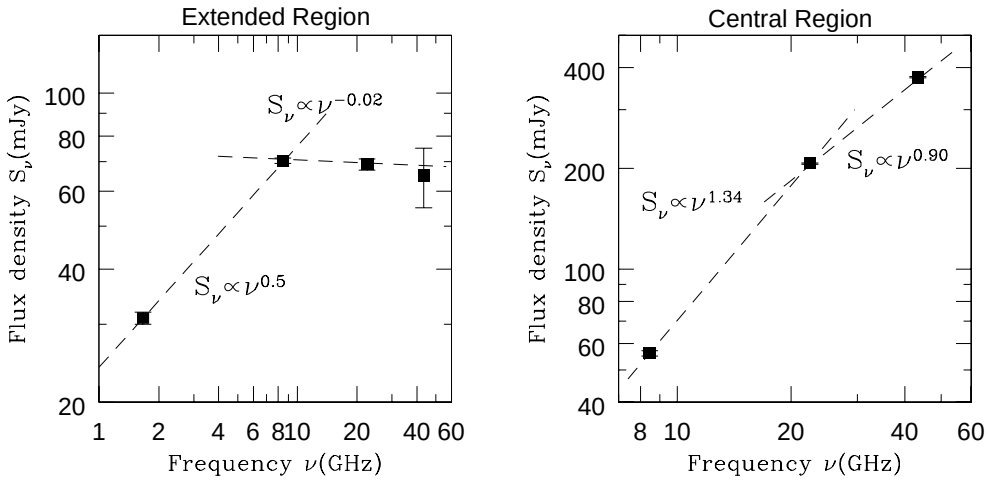

Figure 5.7: Left: Spectral energy distribution of the extended emission in IRAS 17347−3139. Right: Spectral energy distribution of the central component in IRAS 17347−3139.

If we further assume that the extended emission arises from a biconical ionized wind with an expansion velocity of 1000 km s^{-1}, using equation (19) from Reynolds (1986), we estimate a mass-loss rate of $\dot{M}_i \simeq 1.3 \times 10^{-5}$ $(D/\mathrm{kpc})^{3/2}$ $M_\odot$ yr^{-1}. This value is, once again, much larger than those observed in the stellar winds of other PN, favoring the idea that the emission arises from an ionized nebula. Nonetheless, it is worth noting the relatively high degree of collimation of this emission. Moreover, in the image at 3.6 cm the presence of a subtle point-symmetry is suggested. In the northern lobe this emission extends all the ways toward the tip where there is a bow-shaped structure. This morphology could be indicating that the extended ionized regions were excavated by a collimated wind (see §7.5.3).

5.5.2 The Central Region: a High Density Ionized Torus?

In Figure 5.7 (right panel) we show the spectral energy distribution (SED) of the central compact region from 8 to 43 GHz. For this range of frequencies the spectral index is $\alpha \simeq 1$, and seems to become shallower at higher frequencies. The value of the spectral index of this component indicates that the geometry or the density distribution of the ionized gas are different than

in the extended component. Also, the fact that the flux density apparently continues to increase for frequencies as high as 43 GHz indicates that part of this component is still optically thick at such frequencies. Considering that the optical depth is of the order of unity near the turnover frequency, $\nu_m \geq 43$ GHz, assuming a constant electronic temperature, T_e=10^4 K, and that the size of this component along the line of sight is similar to the width obtained from the Gaussian fit ($\sim 0\farcs25$; Table 5.2), we obtain a lower limit for the electron density of $n_e \geq$ 1-3 $\times$ 10^6 cm^{-3} for the distance range from 6 to 0.8 kpc. This value for the density is 5 times larger than the maximum value found for the extended emission. Considering this higher value of the density, and the elongation of this component in the direction perpendicular to the lobes of the extended emission, we suggest that the radio continuum emission is tracing the inner ionized regions of an equatorial torus-like structure, which is observed in the IR image as a dark lane, or waist (see Figs. 5.2, 5.3, and 5.4).

To further confirm this suggestion, we made images at 0.7 cm using only the baselines longer than 500 kλ (and ROBUST parameter = 0) to improve the angular resolution (Fig. 5.8). In this image a double-peaked structure is observed, with the peaks symmetrically separated with respect to the position of the radio continuum peak measured at other frequencies. The separation between the peaks ($\simeq 0\farcs13$) corresponds to 100$-$780 AU for a distance range of 0.8$-$6 kpc. A similar double peaked structure was observed in the PN NGC 2440 by Vázquez et al. (1999). From their observations of radio continuum and recombination lines, these authors inferred the presence of large extinction toward the central region, as well as a rotating, ionized toroid, roughly perpendicular to the bipolar lobes. In the case of IRAS 17347$-$3139 the two radio continuum peaks appear toward the dark lane observed in the IR images, and they are aligned in the direction perpendicular to the axis of the lobes, suggesting that the emission is also arising from an ionized torus-like region.

The water masers detected toward IRAS 17347$-$3139 by dGM04 appear distributed in an elliptical structure with its center shifted $\sim 0\farcs15$ from the peak of the radio continuum. These authors suggested that the peak of the radio continuum could be tracing one stellar component in a binary system while the masers would be associated with a companion star. The angular resolution of their observations ($0\farcs81 \times 0\farcs26$; PA = 26°) did not allow to confirm this suggestion. From our observations we were able to compare the distribution of water masers relative to the radio continuum emission with

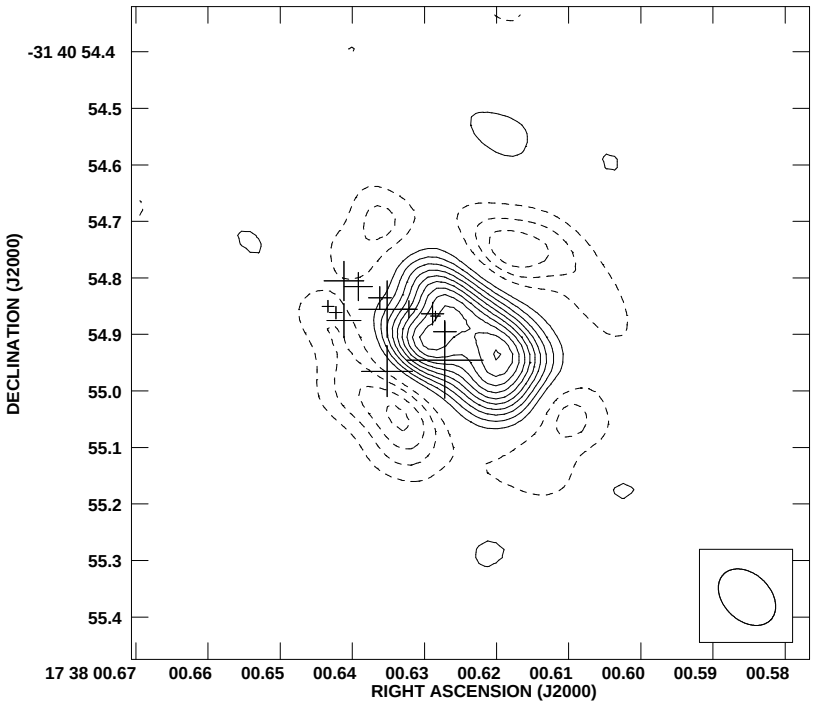

Figure 5.8: VLA image of IRAS 17347−3139 at wavelength 0.7 cm using a ROBUST weight parameter $= 0$, and restricting the visibilities to those with a uv baseline longer than 500 kλ. Contours are −40, −30,−20,−10, 10, 20, 30, 40, 50, 60, 70, 80, 90, 99 per cent of 2.6 $\times 10^{-2}$ Jy/beam, the peak value of the brightness. The value of the first contour is -3 and 3 times the rms noise of the image, 7.4 $\times 10^{-4}$ Jy/beam. The synthesized beam is shown in the bottom right corner, and its size is $0.12'' \times 0.08''$ (PA $= 46°$). Superimposed are shown the positions of the masers reported by dGM04.

higher angular resolution. In Figure 5.8, we have superimposed the water maser emission found by dGM04 on the radio continuum emission at 0.7 cm from our observations. In order to do this, we have shifted the positions of the observations of dGM04, so that the position of the continuum peak emission of their observations coincides with that of our observations at $\lambda \simeq$ 1.3 cm. From this Figure there is no clear evidence of the presence of a secondary companion associated with the maser emission as suggested by dGM04, although this possibility cannot be completely ruled out. If we consider that the emission at 0.7 cm is tracing an ionized torus around the

central star(s), the relative positions of the maser and the continuum emission suggest that the water masers arise from the outer parts of the ionized torus.

5.5.3 Collimated winds and tori in PNe

It is now well known that several proto-PNe and PNe show the presence of collimated structures which often have point-symmetric morphology (Schwarz, Corradi, & Melnick 1992; Sahai & Trauger 1998; Balick & Frank 2002). It has been suggested that these structures are created by collimated winds or jets. Lim & Kwok (2000, 2003) detected collimated radio emission in the core of the PN M2-9 which they interpreted as arising in an ionized jet. More recently, Lee et al. (2007) found optically thick radio cores in narrow-waist bipolar nebulae. They suggest that the radio continuum emission is arising in collimated ionized winds, which would be responsible for the shaping of the PNe.

As mentioned in §4.1, from our radio continuum observations, we found that the ionized extended component of the PN IRAS 17347−3139 shows a relatively high degree of collimation and that its spectral index is consistent with that of an ionized wind. We also note that the image of IRAS 17347−3139 at 3.6 cm (Fig. 5.2) suggests that the extended emission shows a subtle point-symmetry. Furthermore, a closely look of the emission at 1.3 and 0.7 cm (Figs. 5.3 and 5.4) reveals that it also shows point-symmetry which is consistent with the point-symmetry observed at 3.6 cm. In particular, the emission at 0.7 cm has two faint bumps, one toward the north and the other toward the south. These point-symmetric morphologies have been observed in several proto-PNe and PNe (Corradi et al. 1993; Guerrero et al. 1999; Miranda et al. 2001). They have been interpreted as the result of the presence of precessing jet-like winds excavating the slowly expanding envelope ejected during the AGB phase (Miranda et al 2001; Volk et al. 2007). Consequently, based on its morphological structure, we suggest that part of the emission of the extended component of IRAS 17347−3139 could be arising in a precessing ionized wind. Radio recombination line observations could be useful to probe the kinematics of the ionized nebula and confirm the presence of an ionized wind in this source.

The collimated winds have been succesful at explaining the formation of point-symmetric morphologies in proto-PNe and PNe (García-Segura 1997; Velázquez et al. 2007). However, the mechanims responsible for the launching and collimation of such winds remain poorly understood. It has been

observed that the pre-PNe and PNe that present collimated winds often also show the presence of an equatorial torus (Miranda et al. 2001; Sahai et al.2005; Uscanga et al. 2008). It has been proposed that the equatorial tori somehow could be related to the formation of the collimated winds (Mellema et al. 1991, Frank et al. 1993; Huggins 2007). In the GISW model, the torus channels the fast wind toward the polar regions, however it cannot collimate it (García-Segura et al. 1999). Our observations reveal that a torus could be present in the equatorial region of IRAS 17347−3139 (see §4.2), however, given its narrow waist and the possible presence of a precessing collimated ionized wind, the GISW model cannot explain the shape of this PN.

One of the mechanisms proposed to produce collimated outflows assumes that the fast wind is magnetized. Additionally, in the presence of a binary companion, the wind could undergo precession, producing a point-symmetric morphology (García-Segura 1997). However, in these models, while the presence of an equatorial torus is possible, it is not indispensable for the collimation of the jets. On the other hand, Nordhaus & Blackman (2006) proposed that a secondary companion could spiral-in the AGB circumstellar envelope enhancing the magnetic field by dynamo action. During the spiral-in process, an equatorial torus could be ejected, while the enhanced magnetic field could drive a collimated wind. The latter scenario could produce a configuration with an equatorial torus and collimated winds as observed in IRAS 17347−3139.

It has been estimated that the outflow driven by the dynamo action would be explosive and last $\lesssim 100$ years (Nordhaus & Blackman 2006). This value is similar to the kinematical age of the ionized component of IRAS 17347−3139. However, this age represents only a lower limit for the age of the bipolar lobes, suggesting that the collimated wind has been present for more than 100 years. Furthermore, given the low percentage of polarization derived from our OH 1612 MHz maser observations (see §3.2), it is probable that the magnetic field is not very strong. This results suggest that the magnetic fields could not be playing a mayor role in the formation of the collimated structure of this PN. More measurements of the strenght and geometery of the magnetic field are required to further test this model.

Another mechanism, proposed to explain the formation of collimated winds and the ejection of equatorial tori, also assumes that a binary companion spirals-in through the CSE of the AGB star, providing energy to detach the torus. When the spiral-in process of the secondary stops it could undergo Roche lobe overflow to form an accretion disk around the primary

star. Alternatively, the companion could reach a region where it is shredded by gravitational tidal forces to form an accretion disk. Therefore, in a similar way to the star-forming regions, these disks may blow collimated winds that shape the PNs. These modeles predict the presence of an equatorial torus and a colimated wind. They also predict that the ejection of the equatorial torus precedes the formation of the jets. For the case of the PN IRAS 17347−3139, as mentioned above, we estimate that the age of the collimated wind must be greater than 100 years. In addition, from our high resolution image at 0.7 cm (Fig 5.8), we can estimate an inner radius for the torus, which is of the order of half the separation between the two intensity peaks ($\sim 0\farcs06$); for a distance range of 0.8-6 kpc, and assuming a typical expansion velocity of 10 km s^{-1} (Huggins 2007), we find that the torus was completely ejected $\sim$ 25-185 years ago. To determine if the the torus was ejected previously than the collimated wind, and thus be able to test these models, we need a more accurate estimation of the distance to this source.

5.6 Conclusions

We have carried out sensitive high angular resolution VLA observations of the young planetary nebula IRAS 17374−3139. We present the first images of its ionized structure at cm wavelengths. The radio continuum images revealed the presence of a bright central structure, and an extended more tenuous bipolar component.

A double Gaussian fit shows that the extended component is elongated in the same direction as the bipolar lobes observed in the near-infrared images, while the central structure shows an elongation in the perpendicular direction, parallel to the dark lane observed in the IR images. We interpret that the radio continuum emission is arising in two extended ionized lobes, and in an equatorial ionized torus. The electron density at the base of the lobes is 2-6$\times10^5$ cm^{-3}, for a distance range from 6 to 0.8 kpc. This relatively high density in the lobes supports the idea that this source is a very young PN. Given the subtle point-symmetric morphology of the extended component, we suggest the possible presence of a collimated ionized wind in this source. On the other hand, we derive a lower limit for the electron density for the equatorial torus of $n_e \geq$ 1-3 $\times 10^6$ cm^{-3}, given the same distance range as above. A high resolution image at 0.7 cm reveals the presence of a double peak structure in the central component, supporting the interpretation of the

equatorial torus. We compared the distribution of the water maser emission with our high resolution radio continuum images; the relative positions of the maser and the continuum emission suggest that the water masers arise from the outer parts of the ionized torus.

We detected OH maser emission at 1612 MHz toward IRAS 17347−3139. The spectrum shows only one weak feature at $V_{\rm LSR} = -70$ km s^{-1} which coincides spatially with the continuum emission. We derived a 3-σ upper limit of $< 35\%$ for the percentage of circularly polarized emission (m_c=V/I). We also report the detection of OH 1612 MHz maser emission coming from two other sources, J17380406-3138387 and OH 356.65-015, located within our primary beam.

General Conclusions

Currently, there are only three planetary nebulae for which the presence of water maser emission has been confirmed: K 3-35, IRAS 17347−3139 and IRAS 18061−2505. All of these objects have bipolar morphologies with very narrow waists, whose formation challenges the standard models that try to explain the evolution of planetary nebulae. The detection of water maser emission gave origin to the question regarding the survival of the water molecules in an ionized environment. Moreover, the conditions for pumping the water maser emission, requiring densities of 10^9 cm^{-3} and temperatures of $\sim$ 500 K, were not expected to exist for more than $\sim$ 100 years after the massive wind of the AGB phase stopped. To further our understanding on the presence of water maser emission in this type of objects, and on the formation of narrow-waisted bipolar morphologies, in this thesis, we have studied two of these nebulae using observations at radio frequencies. The main results of these observations are the following:

- We could confirm the association of CO emission with the PN K 3-35; additionally, we detected emission from the molecule HCO^+ for the first time. These results confirm that this object is indeed a very young planetary nebula, although probably not as young as initially thought.
- The detection of HCO^+ also suggest the presence of dense molecular material that could be protecting the water molecules from being dissociated by the ionizing radiation. Furthermore, in these dense regions, the conditions for pumping the masers could be favorable; which could explain why the maser emission can last long after the massive wind from the AGB stopped.

K 3-35 also has OH maser emission. Existing polarimetric observations with low spectral and angular resolution shows that the OH 1665 MHz maser

emission was distributed along the direction perpendicular to the bipolar lobes, and is highly circularly polarized. We carried out observations with higher angular and spectral resolution and detected the four OH maser lines at 1612, 1665, 1667 and 1720 MHz. The main results of these observations are the following:

- Our observations confirm the high degree of circular polarization of the 1665 MHz, and show that the transitions at 1612 and 1720 MHz are also circularly polarized. The OH 1665 MHz masers are tightly grouped towards the central region, close to the peak of the radio continuum and seem to trace a structure perpendicular to the bipolar lobes (toroid). From this emission, we found a tentative candidate for a Zeeman pair, which would be due to the presence of a magnetic field of $\simeq 0.9$ mG. The determination of the value of the magnetic field in this kind of stars is very valuable, since it provides constrains to the different models proposed to explain the formation of collimated winds by means of magnetic fields.

- The OH 1667 MHz masers show an extended spatial distribution with a clear gradient of velocities along the direction of the bipolar ionized lobes. This gradient is consistent with the results obtained from optical observations. The centroid velocity of these masers do not coincide with the systemic velocity, but it is blueshifted about $\simeq 15$ km s^{-1}, suggesting that they are arising in the northern parts of the nebula (the approaching lobe).

- The OH 1720 MHz maser appears at a single velocity and is spatially localized coincident with the peak of the λ=1.3 cm radio continuum. The velocity of the maser emission is very similar to the systemic velocity, and we think this emission is arising very close to the central star.

In 2005, using the VLA, we carried out high angular resolution radio continuum observations toward the young planetary nebula IRAS 17347−3139. The main results of these observations are the following:

- We have resolved and imaged for the first time the structure of the ionized component in this nebula. At $\lambda = 3.6$ and 1.3 cm, the emission is extended in the same direction as the bipolar lobes seen in the infrared

images. It also shows a central, compact and bright region, which at $\lambda = 0.7$ cm, appears elongated in the direction perpendicular to the bipolar lobes and coinciding with a dark lane seen in the infrared images. The spectral index of the extended emission is similar to that of an ionized wind, however, the mass-loss rate derive from this assumption is too large as compared with the values of other similar sources. Nonetheless, we note that the morphology of this emission presents a subtle point symmetry, persuading us to think that probably part of the extended emission is indeed arising in an ionized wind, which would be just in the process of shaping the bipolar lobes.

- We compared the distribution of the water masers in IRAS 17347−3139 with the high angular resolution radio continuum images of our observations. From an inspection of the images, there is no evidence supporting the previous proposition that the radio continuum and the masers are associated with two different components, respectively; it can rather be argued that it is more likely that the masers are arising in one side of a dense circumstellar torus, the blueshifted one.

- We detected a weak maser feature ($\simeq$ 40 mJy) from the OH 1612 MHz transition at a velocity $v_{LSR} \simeq -70$ km s^{-1}, which coincides spatially with the radio continuum. No emission was detected from the other three transitions. Within our primary beam, we also detected maser emission in the velocity ranges that were reported previously, however, the emission was found to be associated to other two sources: J17380406-3138387 and OH 356.65-015.

In general, we conclude that our study confirms that K 3-35 and IRAS 17347−3139 are indeed two objects for which the ionization began in a relatively recent time: $\sim$ 100 years. Both objects present dense molecular material, which could explain the presence of water maser emission even though the ionization of the circumstellar envelope had begun. On the other hand, both objects have a bipolar morphology with narrow waists that could be explained in terms of a collimated, precessing wind shaping the bipolar lobes. Therefore, the presence of a binary system in the center of the planetary nebulae is required, and the standard generalized interacting winds model cannot be used. The scheme proposed for the disappearance of the maser emission cannot be followed either in these type of objects; the persistence

of water maser emission has to be interpreted in terms of a different evolutionary scenario. Our measurement of the magnetic field present in the equatorial region of K 3-35 is important to constrain the models, however, it is not clear what is the role that it is playing in the overall collimation of the bipolar lobes in this nebula.

Bibliography

Aaquist, O., 1993, A&A, 267, 260

Aaquist, O. B. & Kwok, S. 1989, A&A, 222, 227

Bachiller, R., Forveille, T., Huggins, P. J., & Cox, P. 1997, A&A, 324, 1123

Bains, I., Gledhill, T., Yates, J. & Richards, A. 2003, MNRAS, 338, 287

Balick, B. 1987, AJ, 96, 671

Balick, B., Preston, H.L., & Icke, V. 1987, ApJ, 94 1641

Balick, B. & Frank, A. 2002, ARA&A, 40, 439

Barvainis, R., McIntosh, G. & Predmore, C. R. 1987, Nature, 329, 613

Baud, B. & Habing, H.J. 1983, A&A, 127, 73

Blackman, E. G., Frank, A., Markiel, J. M., Thomas, J. H., Van Horn, H. M. 2001, Nature, 409, 485

Böhm-Vitense, E. Introduction to Stellar Astrophysics: Vol 3 (Introduction to Stellar Astrophysics) 1992

Booth, R. S., Kus, A. J., Norris, R. P. & Porter, N. D. 1981, Nature, 290, 382

Bowers, P. F. & Hagen, W. 1984, ApJ, 285, 637

Bowers, P. F. & Knapp, G. R. 1989, ApJ, 347, 325

Briggs, D. S. 1995, PhD thesis, New Mexico Institute of Mining and Technology

Calvet, N. & Peimbert, M. 1983, RMxAA, 5, 319

Capriotii, E.R. 1973, ApJ, 179, 495

Chapman, J. M. & Cohen, R. J. 1986, MNRAS, 220, 513

Chapman, J., Cohen, R. J., Saikia, D. J., MNRAS, 249, 227

Chevalier, R.A., Luo, D. 1994, ApJ, 435,815

Clark, F. O., Troland, T. H., Pepper, G. H. & Johnson, D. R. 1984, ApJ, 283, 174

Claussen, M. J., Sahai, R. & Morris, M. R. 2009, ApJ, 691 219

Cook, B. & Elitzur, M. 1985, ApJ, 295, 175

Corradi, R. L. M., Schwarz, H. E., & Stanghellini, L. 1993, in IAU Symp. 155, Planetary Nebulae, ed. R. Weinberger & A. Acker (Dordrecht: Kluwer), 216

Crutcher, R. M.; Kazes, I. 1983, A&A, 125, 23

Crutcher, R. M., Troland, T. H., Goodman, A. A., Heiles, C., Kazes, I. & Myers, P. C. 1993, ApJ, 407, 175

Davies, R. D. 1974, in IAU Symp. 60, Galactic Radio Astronomy, ed. F. J. Kerr & S. C. Simonson, III (Dordrecht: Reidel), 275

Dayal, A. & Bieging, J. H. 1996, ApJ, 472, 703

Deacon, R. M., Chapman, J. M.& Green, A. J. 2004, ApJS, 155, 595

de Gregorio-Monsalvo, I., Gómez, Y., Anglada, G., Cesaroni, R., Miranda, L. F., Gómez, J. F. & Torrelles, J. M. 2004, ApJ, 601, 921 [dGM04]

de Jong, T. 1983, ApJ, 274, 252

Diamond, P.J., Norris, R.P., Rowland, P.R., Booth, R.S., & Nyman, L-Å. 1985, MNRA, 212, 1

Diamond, P. J. & Kemball, A. J. 1999, in Asymptotic Giant Branch Stars, IAU Symposium 191, Edited by T. Le Bertre, A. Lebre, & C. Waelkens. p. 195

Elitzur, M. 1976, A&A, 52, 213

Elitzur, M. 1982, Reviews of Modern Physics, 54, 1225

Elitzur, M. 1992, ARA&A, 30, 75 (Elitzur 1992a)

Elitzur M. 1992, Astronomical masers, Kluwer Academic Publishers (Astrophysics and Space Science Library. Vol. 170; Elitzur 1992b)

Engels, D., Schmid-Burgk, J., Walmsley, C.M. & Winnberg, A. 1985, A&A, 148, 344

Engels, D., Schmid-Burgk, J. & Walmsley, C.M. 1986, A&A, 167, 129

Estallela R., & Anglada G., Introducción a la Física del Medio Interestelar, Textos Docentes, 50. Ediciones UB, Barcelona, 1999

Etoka, S., & Diamond, P. 2004, MNRAS, 348, 34

Faulkner, D.J. 1970, ApJ, 162, 513

Ferrari, A. 1998, ARA&A, 36, 539

Ferch, R. L. & Salpeter, E. E. 1975, ApJ, 202, 195

Finzi, A. & Wolf, R.A. 1971, A&A, 11, 418

Fleischer, A. J., Gauger, A., & Sedlmayr, E. 1992, A&A, 266, 321

Frail, D. A., Goss, W. M., Slysh, V. I. 1994, ApJ...424L.111

Frank, A., Balick, B., Icke, V., & Mellema, G. 1993, ApJ, 404, 25

Frank, A. 1994, AJ, 107,261

Frank, A., De Marco, O., Blackman, E., & Balick, B. 2007

García-Segura, G. 1997, ApJ, 489, 189

García-Segura, G., Langer, N., Rózyczka, M. & Franco, J. 1999, ApJ, 517, 767

García-Segura, G. & López, J. A. 2000, ApJ, 544, 336

García-Segura, G., López, J. A., & Franco, J., 2005, ApJ, 618, 919

García-Segura, G. 2006, IAU 243, Planetary Nebulae in our Galaxy and Beyond. Edited by Michael J. Barlow and Roberto H. Méndez. Cambridge: Cambridge University Press, p.297

Gómez, Y., Moran, J.M., & Rodríguez, L.F. 1990, RevMexAA, 20, 55

Gómez, Y. & Rodríguez, L. F. 2001, ApJ, 557, 109

Gómez, Y., Miranda, L. F., Anglada, G., & Torrelles, J. M. 2003, in IAU 209, Planetary Nebulae, (Sn Francisco:ASP), p.263

Gómez, J. F., de Gregorio-Monsalvo, I., Lovell, J. E. J., Anglada, G., Miranda, L. F., Suárez, O., Torrelles, J. M., & Gómez, Y. 2005, MNRAS, 364, 738 [G05]

Gómez, Y., Tafoya, D., Anglada, G., Franco-Hernández, R., Torrelles, J. M., Miranda, L. F., 2005, MmSAI..76..472

Gómez, J. F., Suárez, O., Gómez, Y., Miranda, L. F., Torrelles, J. M., Anglada, G. & Morata, O. 2008, AJ, 135, 2074

Gómez, Y., Tafoya, D., Anglada, G., Miranda, L. F., Torrelles, J. M., Patel, N. A. & Franco-Hernandez, R. Accepted in ApJ, in press.

Greaves, J. S. 2002, A&A, 392, 1

Guerrero, M. A., Vázquez, R. & López, J. A. 1999, AJ, 117, 967

Habing, H. J. 1996, A&A Rev, 7, 97

Härm, R. & SchwarZschild, M. 1975, ApJ, 200, 324

Heiles, C., Goodman, A. A., McKee, C. F. & Zweibel, E. G., 1993,in Protostars and Planets III, ed. E. H. Levy & J. I. Lunine (Tucson: Univ. Arizona Press), 279

Herman, J. & Habing, H. 1981, Physical Processes in Red Giants, edited by I. Iben and A. Renzini (Reidel, Dordrecht), p. 383

Herpin, F., Baudry, A., Thum, C., Morris, D. & Wiesemeyer, H., 2006, A&A, 450, 667

Herschel, W. 1785, Philosophical Transactions of the Royal Society of London, 75, 213

Herschel, W. 1786, Philosophical Transactions of the Royal Society of London, 76, 457

Herschel, W. 1789, Philosophical Transactions of the Royal Society of London, 79, 212

Hirano, N., Shinnaga, H., Dinh-V-Trung, Fong, D., Keto, E., Patel, N., Qi, C., Young, K., Zhang, Q. & Zhao, J. 2004, ApJ, 616, 43

Huggins, P. J., Bachiller, R., Cox, P.& Forveille, T. 1992, ApJ, 401, 43

Huggins, P. J., Bachiller R., Cox, P. & Forveille, T. 1996, A&A, 315, 284

Huggins, P. J., Bachiller, R., Planesas, P., Forveille, T. & Cox, P. 2005, ApJS 160 272

Huggins, P. J. 2007, ApJ, 663, 342

Icke, V. 1988, A&A, 202, 177

Icke, V., Preston, H.L. & Balick, B. 1989 AJ, 97, 462

Icke, V., Mellema, G., Balick, B. & Eulderink, F. 1992, Nature, 355, 524

Imai, H., Obara, K., Diamond, P. J., Omodaka, T. & Sasao, T. 2002, Nature, 417, 829

Imai, H., Sahai, R. & Morris, M. 2007, ApJ, 669, 424

Jewell, P.R., Webber, J.C., Snyder, L.E. 1980, ApJ, 242, L29

Jordan, S., Werner, K. & O'Toole, S. J. 2005, A&A, 432, 273

Josselin, E. & Bachiller, R. 2003, A&A, 397, 659

Kahn, F. D. & West, K. A. 1985, MNRAS, 212, 837

Kemball, A. J. & Diamond, P. J. 1997, ApJ, 481, L111

Knapp, G. R., & Morris, M. 1985, ApJ, 292, 640

Kutter, G.S. & Sparks, W.M. 1974, ApJ, 192, 447

Kwok, S., Purton, C.R. & FitzGerald, M. P. 1978, ApJ, 219, L125

Kwok, S. 1993, ARA&A, 31, 63

Kwok, S. 2009, AS&S, 319, 5

Lee, T.-H., Lim, J. & Kwok, S. 2007, ApJ, 665, 341

Lewis, B. M. 1989, ApJ, 338, 234

Likkel, L. & Morris, M. 1988, ApJ, 329, 914

Likkel, L., Morris, M. & Maddalena, R. J. 1992, A&A, 256, 581

Lim, J., & Kwok, S. 2000, in ASP Conf. Ser. 199, Asymmetric Planetary Nebulae II: From Origins to Microstructures, ed. J. Kastner, S. Rappaport, & N. Soker (San Francisco: ASP), 259

Lim, J., & Kwok, S. 2003, in ASP Conf. Ser. 303, Symbiotic Stars Probing Stellar Evolution, ed. R. L. M. Corradi, J. Mikolajewska, & T. J. Mahoney (San Francisco: ASP), 437

Lockett, P. & Elitzur, M. 1992, ApJ, 399, 704

Lucas, R., Guélin, M., 1999, IAU Symposium 191, edited by T. Le Bertre, A. Lebre and C. Waelkens, p. 305

Manchado, A., Guerrero, M. A., Stanghellini, L. & Sierra-Ricat, 1996, The IAC Morphological Catalog of Northern Galactic Planetary Nebulae, ed. Instituto de Astrofísica de Canarias.

Marvel, K. B. & Boboltz, D. A. 1999, AJ, 118, 1791

Matt, S., Balick, B., Winglee, R. & Goodson, A., 2000, ApJ, 545, 965

Matt, S., Winglee, R. M., & Böhm, K.-H. 2003, Ap&SS, 287, 65

Matt, S., Frank, A., & Blackman, E. G. 2004, in ASP Conf. Ser. 313, Asymmetric Planetary Nebulae III, ed. M. Meixner et al. (San Francisco: ASP), 449.

Mellema, G., Eulderink, F., & Icke, V. 1991, A&A, 252, 718

Mellema, G. 1994, A&A, 290, 915

Mellema, G. & Frank, A. 1995, MNRAS, 273,401

Mellema, G. 1994, MNRAS, 277, 173

Mezger, P. G. & Henderson, A. P. 1967, ApJ, 147, 471

Miranda, L. F. & Solf J. 1992, A&A, 260, 397

Miranda, L. F., Torelles, J. M. & Eiroa, C. 1995, ApJ, 446, 39

Miranda, L. F., Torrelles, J. M., Guerrero, M. A., Aaquist, O. B., & Eiroa, C. 1998, MNRAS, 298, 243.

Miranda, L. F., Fernández, M., Alcalá, J. M., Guerrero, M. A., Anglada, G., Gómez, Y., Torrelles, J. M. & Aaquist, O. B. 2000, MNRAS, 311, 748

Miranda, L. F., Gómez, Y., Anglada, G. & Torrelles, J. M. 2001, Nature, 414, 284.

Moran, J. M., Burke, B. F., Barret, A. H., Rogers, A. E. E., Carter, J. C., Ball, J. A. & Cudaback, D. D. ApJ, 152, L98

Nakagawa, A., Omodaka, T., Shibata K. M., Kurayama, T., Imai, H., Kameno, S., Tsushima, M., Matsumoto, N., Matsui, M. and the VERA project team 2008, Proceedings of the International Astronomical Union (2007), 3:206-207 Cambridge University Press

Nomoto, K., Thielemann, F.-K. & Yokoi, K. 1984, ApJ, 286, 644

Nordhaus, J. & Blackman, E. G. 2006, MNRAS, 370, 2004

Nyman, L-Å& Olofsson, H. 1986, A&A, 158, 67

Olnon, F. M. 1975, A&A, 39, 217

Panagia, N. & Felli, M. 1975, A&A, 39, 1

Pardo, J. R., Cernicharo, J. & Goicoechea, J. R. 2007 ApJ, 661, 250

Pascoli G. 1997, ApJ, 489, 946

Patriarchi, P. & Perinotto, M. 1991, A&AS, 91, 325

Payne, H. E., Phillips, J. A. & Terzian, Y. 1988, ApJ, 326, 368

Reid, M. J., Muhleman, D. O., Moran, J. M., Johnston, K. J., & Schwartz, P. R. 1977, ApJ, 214, 60

Reid, M. J. & Moran, J. M. 1981, ARA&A, 19, 231

Reynolds, S. P. 1986, ApJ, 304, 713

Robishaw, T., Quataert, E. & Heiles, C. 2008, ApJ, 680, 981

Rodríguez, L. F., Gómez, Y. & García-Barreto, J. A. 1985, RMxAA, 11, 109

Rózyczka, M. & Franco, J. 1996, ApJ, 469, L127

Rybicki, G. B., & Lightman, A. P. Radiative Processes in Astrophysics, Wiley-Interscience, 1979

Sabin, L., Zijlstra, A. A. & Greaves, J. S., 2007, MNRAS, 376, 378

Sahai, R. & Trauger, J. T. 1998, AJ, 116, 1357

Sahai, R., Le Mignant., D., Sánchez-Contreras, C., Campbell, R. D. & Chaffee, F. H., 2005, ApJ, 622, 53

Sahai, R., Morris, M., Sánchez-Contreras, C. & Claussen, M. 2007, AJ, 134, 2200

Salpeter, E.E. 1952, ApJ,115,326

Sánchez-Contreras, C., Le Mignant, D., Sahai, R., Chaffee, F. H. & Morris, M. 2006, in IAU Symp. 234, Planetary Nebulae in Our Galaxy and Beyond, ed. M. J. Barlow & R. H. Méndez (Cambridge: Cambridge Univ. Press)

Sault, R.J., Killeen, N.E.B., Zmuidzinas, J. & Loushin, R. 1990, ApJ, 74, 437

Schultz, G.V., Sherwood, W.A. & Winnberg, A. 1978, A&A, 63, L5

Schwarz, U.J. Troland, T.H. Albinson, J.S., Bregman, J.D., Goss, W.M. & Heiles, C. 1986, ApJ, 301, 320

Schwarz, H. E., Corradi, R. L. M. & Melnick, J. 1992, A&AS, 96, 23

Schwarzschild, M. Structure and evolution of the stars, Princeton, Princeton University Press, 1958.

Sevenster, M. N. & Chapman, J. M. 2001, ApJ, 546, L119

Sedlmayr, E. 1994, in Molecules in the Stellar Environment, Proc. IAU Colloq. 146, ed. U. G. J¿rgensen (Springer, Berlin), 163

Shklovsky , 1956

Smith, R.L., Rose, W.K. 1972, ApJ, 176, 395

Sobolev, V. V. 1958, Theoretical Astrophysics, edited by V. A. Ambartsumyan, translated by J. B. Sykes (Pergamon London), Chap. 29.

Soker, N. & Livio, M. 1989, ApJ, 339, 268

Soker, N. & Rappaport, S. 2000, ApJ, 538, 241

Soker, N. 2006, PASP, 118, 260

Stanghellini, L., Corradi, R. L. M., & Schwarz, H. E. 2000, ApJ, 534, 167

Starrfield, S., Sparks, W. M. & Truran, J. W. 1985, ApJ, 291, 136

Sun, J. & Kwok, S. 1987, A&A, 185, 258

Szymczak, M., Baszkiewicz, L., Etoka, S. & Le Squeren, A. M., 2001,A&A, 379, 884

Szymczak, M. & Gérard, E. 2004, A&A, 423, 209

Szymczak, M. & Gérard, E. 2005, A&A, 433, L29

Tafoya, D., Gómez, Y., Anglada, G., Loinard, L., Torrelles, J. M., Miranda, L. F., Osorio, M., Franco-Hernández, R., Nyman, L.-A., Nakashima, J. & Deguchi, S. 2007, AJ, 133, 364

Te Lintel Hekkert, P., 1991, A&A, 248, 209

Te Lintel Hekkert, P. T. L., Chapman, J. M., & Zijlstra, A& A, 1992ApJ...390L..23

Te Lintel Hekkert, P. T. L.,& Chapman, J. M., A&AS, 1996, 119, 459

Townes, H. C. & Schawlow, A. L. Microwave Spectroscopy, Courier Dover Publications, 1975

Trimble,V. & Sackman,I.-J. 1978, MNRAS, 182, 97

uchman, Y., Sack, N. & Barket, Z. 1979, ApJ, 234, 217

Uscanga, L., Gómez, Y., Raga, A. C., Cantó, J., Anglada, G., Gómez, J. F., Torrelles, J. M. & Miranda, L. F., 2008, MNRAS, submitted.

Vassiliadis, E. & Wood, P. R. 1994, ApJS, 92, 125

Vázquez, R., Torrelles, J. M., Rodríguez, L. F., Gómez, Y., López, J. A. & Miranda, L. F. 1999, ApJ, 515, 633

Velázquez, P. F., Gómez, Y., Esquivel, A. & Raga, A. C. 2007, MNRAS, 382, 1965

Verschuur, G. L. & Kellermann, K. I., (Editors) Galactic and Extra-galactic Ratio Astronomy (Springer, Berlin, 1988, second edition).

Vlemmings, W. H. T., van Lagevelde, H. J. & Diamond, P. J. 2005, A&A, 434, 1029

Vlemmings, W. H. T., Diamond, P. J. & Imai, H. Nature, 440, 58

Vlemmings, W. H. T. & van Langevelde, H. J., 2008, A&A 488, 619

Volk, K., Kwok, S. & Hrivnak, B. J. 2007, ApJ, 670, 1137

Wentzel, D.G 1976. ApJ, 204, 452

Winters, J. M., Le Bertre, T., Jeong, K. S., Helling, C., & Sedlmayr, E. 2000, A&A, 361, 641

Wood, P.R. 1974, ApJ, 190, 609

Zhang, C. Y. 1995, ApJS, 98, 659

Zhang, Q., Hunter, T. R., Sridharan, T. K., & Ho, P. T. P. 2002, ApJ, 566, 982

Zijlstra, A. A., Te Lintel Hekkert, P., Pottasch, S. R., Caswell, J. L., Ratag, M. & Habing, H. J. 1989, A&A, 217, 157

TeX document compiled on MacOS X, Version 10.4.11,
using pdfTeX, Version 3.141592-1.40.3 (Web2C 7.5.6)

Printed in Mexico